ABSTRACT

CORROSION STUDIES ON α TANTALUM AND β TANTALUM COATED STEEL

by
Sung Min Maeng

Tantalum coating by sputtering, one form of physical vapor deposition (PVD), has been investigated as a replacement for chromium coatings on gun bores to protect them from erosion and corrosion due to its high ductility and high corrosion resistance in aggressive environments. When deposited as a film on steel substrates by sputtering, either α-Ta, β-Ta, or a mixture of both phases have been observed under varying deposition conditions. To evaluate corrosion behavior of Ta coatings, electrochemical impedance spectroscopy and potentiodynamic polarization were conducted as a function of coating thickness. The coating porosity was observed to decrease with increasing coating thickness and hence, coatings greater than 50 μm exhibited corrosion resistance consistent with the bulk phase. Substrate roughness appeared to have little to no effect on the coating quality with respect to corrosion performance for 50 μm α-Ta coatings.

Coatings produced in full scale processes revealed that for Ta coating (< 50 μm), the corrosion process was dominated by dissolution of the steel substrate through open pores, however, at the end of 5 days, coating degradation was not observed. In contrast, while open pores were not observed with the Cr coatings, the corrosion resistance decreased as a function of time under acidic conditions, resulting in dissolution and oxidation of Cr. Initially, however, the sputtered Cr coating exhibited improved corrosion resistance over the electrodeposited one, potentially due to its oxide film.

The unique properties of tantalum oxide films produced from anodic oxidation and thermal oxidation demonstrates that the nanoscale oxide films formed exhibit an ordered local structure reflecting the very compact nature that enhances its corrosion resistance.

CORRODION STUDIES ON α TANTALUM AND β TANTALUM COATED STEEL

by
Sung Min Maeng

A Dissertation
Submitted to the Faculty of
New Jersey Institute of Technology
in Partial Fulfillment of the Requirements for the Degree of
Doctor of Philosophy in Environmental Engineering

Department of Civil and Environmental Engineering

January 2005

APPROVAL PAGE

CORROSION STUDIES ON α TANTALUM AND β TANTALUM COATED STEEL

Sung Min Maeng

Dr. Lisa Axe, Dissertation Advisor — Date
Associate Professor of Civil and Environmental Engineering, NJIT

Dr. Trevor A. Tyson, Dissertation Co-Advisor — Date
Associate Professor of Physics, NJIT

Dr. Daniel J. Watts, Committee Member — Date
Executive Director of York Center for Environmental Engineering and Science, NJIT

Dr. Hsin-Neng Hsieh, Committee Member — Date
Professor of Civil and Environmental Engineering, NJIT

Dr. Jay N. Meegoda, Committee Member — Date
Professor of Civil and Environmental Engineering, NJIT

Dr. Zafar Iqbal, Committee Member — Date
Research Professor of Chemistry and Environmental Science, NJIT

BIOGRAPHICAL SKETCH

Author: Sung Min Maeng

Degree: Doctor of Philosophy

Date: January 2005

Undergraduate and Graduate Education:

- Doctor of Philosophy in Environmental Engineering, New Jersey Institute of Technology, Newark, NJ 07102, 2005
- Master of Science in Environmental Engineering, New Jersey Institute of Technology, Newark, NJ 07102, 1999
- Master of Science in Environmental Engineering, Inha University, Inchon, Korea, 1996
- Bachelor of Science in Environmental Engineering, Inha University, Inchon, Korea, 1994

Major: Environmental Engineering

Publications and Presentations:

S. Maeng, L. Axe, T. A. Tyson, P. Cote, "Corrosion behavior of electrodeposited and sputtered Cr coatings and sputtered Ta coatings with α- and β-phase," submitted to *Surf. Coat. Technol.* (2004).

S. Maeng, L. Axe, T. A. Tyson, L. Gladczuk, M. Sosnowski, "Corrosion behavior of magnetron sputtered α-Ta coatings on AISI 4340 steel with different surface roughness," submitted to *Surf. Coat. Technol.* (2004).

S. Maeng, L. Axe, T. A. Tyson, L. Gladczuk, M. Sosnowski, "Corrosion behavior of magnetron sputtered α- and β-Ta coatings as a function of thickness," submitted to *J. of Corr. Sci.* (2004).

S. Maeng, L. Axe, T. A. Tyson, A. Jiang, "An investigation on structure of thermal and anodic tantalum oxide films," *J. of Electrochem. Soc.* in press (2004).

S. Maeng, L. Axe, T. A. Tyson,, "Characterization of Gun-Barrel Steel Corrosion as Function of Time in Concentrated Hydrochloric Acid Solution," *Corrosion*, Vol. 58, No. 4, pp. 370-380 (2002).

From my heart, I would like to dedicate this dissertation:

To my wife, Jee Young Park who showed me her love, patience, sacrifices, and encouragement until I reached this destination. I can never imagine my life without you.

To my son, Jonathan (Hyun Seo) who always makes my everyday life happier than ever. I will never forget the precious moment you were born. I love you so much.

To my parents, Philsoo Maeng and Bunja Park who have showed me their endless love and made all the sacrifices and support throughout my life. I love and respect both of you very much.

To my father-in-law who passed away. I know you want me to always take good care of your daughter. I promise that I will not disappoint you.

ACKNOWLEDGEMENT

I wish to express my sincere appreciation to my advisor, Dr. Lisa Axe, for her invaluable guidance, enthusiastic encouragement, and precious advice throughout my doctoral research. I also wish to thank Dr. Trevor Tyson for his invaluable comments and advice throughout my doctoral research. In addition to their advice, what I really learned from them is the passion as a researcher. I could never have arrived at this destination without their guidance.

I am greatly thankful to Dr. Daniel Watts, Dr. Hsin-Neng Hsieh, Dr. Jay N. Meegoda, and Dr. Zafar Iqbal for their efforts and valuable comments as members of the committee. It is my honor to have them as my committee members. I am very grateful to Dr. Marek Sosnowski for providing tantalum coating samples for this research and giving me valuable comments, and thank to Dr. Leszeck Gladczuk who showed me friendship in working together to make samples. My special thanks go to Ying Xu, Thipnakarin Boonfueng and Aiqin Jiang for their warm friendship as my colleagues and Mr. Chandrakant Patel for his friendship and encouragement throughout my life in NJIT. I am thankful to my good friends, Chul-Woo Lee and Hyun-Seok Kim, who have showed me what is real friendship and encouraged me from Korea.

At last, I am very thankful to the Sustainable Green Manufacturing Program, through the National Defense Center for Environmental Excellence for financial support throughout this research.

TABLE OF CONTENTS

Chapter **Page**

1 INTRODUCTION 1

2 CORROSION RESISTANCE OF TANTALUM 5

3 BACKGROUND 12

3.1 Electrochemical Theory on Corrosion 12

3.1.1 Electrochemical Reaction in Aqueous Corrosion 12

3.1.2 Electrochemical Thermodynamics 14

3.1.2.1 Free Energy and Electrode Potential 14

3.1.2.2 Concentration Effects on Electrode Potential 14

3.1.2.3 Graphical Representation of Electrochemical Equilibrium 16

3.1.3 Electrochemical Kinetics of Corrosion 17

3.1.3.1 Activation Polarization 21

3.1.3.2 Concentration Polarization 24

3.1.4 Mixed Electrode 25

3.2 Electrochemical Impedance Spectroscopy 26

3.3 Galvanic Corrosion 39

3.4 Hydrogen Embrittlement 46

3.5 Evaluation of Porosity of Metal Coatings by Electrochemical Techniques 47

3.6 Summary 51

4 OBJECTIVES AND OVERALL APPROACH 53

5 METHODS 56

5.1 Materials 56

TABLE OF CONTENTS
(Continued)

Chapter **Page**

5.2 X-ray Diffraction 59

5.3 Electrochemical Tests 59

5.3.1 Potentiodynamic Polarization 62

5.3.2 Electrochemical Impedance Spectroscopy 64

5.3.3 Galvanic Corrosion Test 65

5.3.4 Anodic Oxidation 65

5.4 Scanning Electron Microscopy (SEM) and Energy Dispersive X-ray Spectroscopy (EDX) 66

5.5 Extended X-ray Absorption Fine Structure Spectroscopy (EXAFS) 66

6 CORROSION BEHAVIOR OF MAGNETRON SPUTTERED α- AND β-Ta COATINGS ON AISI 4340 STEEL AS A FUNCTION OF COATING THICKNESS 69

6.1 Introduction 69

6.2 Experimental Methods 71

6.2.1 Preparation of Substrates and Ta Deposition 71

6.2.2 Coating Characterization 72

6.2.3 Electrochemical Tests 72

6.2.3.1 Galvanic Current Measurement 72

6.2.3.2 Potentiodynamic Polarization and EIS 73

6.3 Results and Discussions 73

6.3.1 Phase and Microstructure of Ta Coatings 73

6.3.2 Galvanic Corrosion 78

TABLE OF CONTENTS
(Continued)

Chapter **Page**

6.3.3 Potentiodynamic Polarization 79

6.3.4 Corrosion Behavior as a Function of Immersion Time Evaluated by EIS 86

6.4 Summary 98

7 CORROSION BEHAVIOR OF MAGNETRON SPUTTERED α-Ta COATINGS ON SMOOTH AND ROUGH STEEL SUBSTRATES 99

7.1 Introduction 99

7.2 Experimental Methods 100

7.3 Results and Discussions 102

7.3.1 Phase and Structure of the Ta Coatings 102

7.3.2 Porosity Assessment 108

7.3.3 Corrosion Behavior as a Function of Time 111

7.4 Summary 116

8 CORROSION BEHAVIOR OF ELECTRODEPOSITED AND SPUTTERED Cr COATINGS AND SPUTTERED Ta COATINGS WITH α- AND β-PHASE 118

8.1 Introduction 118

8.2 Experimental Methods 119

8.3 Results and Discussions 121

8.3.1 Phase Identification and Morphology 121

8.3.2 Corrosion Behavior of as Function of Immersion Time Evaluated by EIS 129

8.3.3 Anodic Polarization Behavior of Cr Coatings 138

TABLE OF CONTENTS
(Continued)

Chapter **Page**

8.4 Summary 141

9 AN INVESTIGATION ON STRUCTURES OF THERMAL AND ANODIC TANTALUM OXIDE FILMS 142

9.1 Introduction 142

9.2 Experimental Methods 143

9.3 Results and Discussion 145

9.4 Summary 159

10 CONCLUSIONS 160

11 FUTURE RESEARCH 163

APPENDIX A ELECTROCHEMICAL IMPEDANCE SPECTROSCOPY OF AISI 4340 STEEL 165

APPENDIX B DEKTAK SURFACE PROFILE OF ROUGH AND α-TA COATINGS WITH 50 μm ON ROUGH STEEL 167

REFERENCES 173

LIST OF TABLES

Table		Page
1.1	Properties of Tantalum	2
2.1	Structural information of tantalum suboxides* and tantalum pentoxide	6
2.2	Density and dielectric constant of Ta_2O_5 thin films	8
2.3	Etching rates of Ta_2O_5 thin films in various solutions	8
2.4	Corrosion resistance of refractory metals in various corrosive media	9
3.1	Corrosion potential (mV_{SCE}) of Metals after 24-h immersion if four different solutions, compared with the emf series[a]	44
5.1	Typical chemical composition of AISI 4340 steel and gun-barrel steel	57
5.2	Procedure of steel substrate preparation prior to Ta coating	58
5.3	Mechanical polishing for steel substrate	58
6.1	Electrochemical characteristics of Ta coatings, Ta foil and steel (AISI 4340) substrate.	82
6.2	The porosity of α- and β-Ta coated steel (AISI 4340) as a function of thickness evaluated from polarization resistance 1 h after immersion.	85
7.1	Results of EXAFS fits* on the first shell for α-Ta coatings on the smooth and rough steel substrate Fourier transformed over 2.85 to 15.8 $Å^{-1}$ k-range and fitted over 1.78 to 3.05 Å r-range.	105
7.2	Electrochemical characteristics of α-Ta coatings with different roughness, the smooth and rough steel substrates and Ta foil.	110
8.1	Results of EXAFS fits* on the first shell for PVD and ED Cr coatings and Cr foil Fourier transformed over 2.4 to 15.7 $Å^{-1}$ k-range and fitted over 1.56 to 3.15 Å r-range.	125
8.2	Results of EXAFS fit* on the first shell for α-Ta coating on the steel substrate Fourier transformed over 2.85 to 15.8 $Å^{-1}$ k-range and fitted over 1.70 to 3.05 Å r-range.	127
9.1	Results of EXAFS fitting for β-Ta_2O_5 powder and 800 °C thermal oxide film over 2.2 to 15.2 $Å^{-1}$ k-range and 0.92 to 2.04 Å r-range.	154

LIST OF FIGURES

Figure **Page**

3.1 Basic corrosion process occurring on the metal surface 13

3.2 Potential – pH diagram for for Iron (Fe) at 25 °C. Dark area indicates corrosion susceptibility. Labels 0, -2, -4, and –6 are the log of solution ion activity for the indicated lines 18

3.3 Potential – pH diagram for for Cr at 25 °C. Dark area indicates corrosion susceptibility. Labels 0, -2, -4, and –6 are the log of solution ion activity for the indicated lines 19

3.4 Potential – pH diagram for tantalum/water system at 25 °C 20

3.5 Activation overpotential showing Tafel behavior 22

3.6 Polarization of anodic and cathodic half-cell reactions for iron in acid solution to give a mixed potential, E_{corr}, and a corrosion rate (current density), i_{corr}. 26

3.7 Equivalent circuit for a simple corroding system with a solution resistance 28

3.8 Nyquist impedance plot obtained from the EIS measurement consisting of circuit as shown in Figure 3.7. 30

3.9 Bode plot of electrochemical impedance spectroscopy obtained from measurement on Dummy cell consisting of the circuit shown in Figure 3.7 31

3.10 Equivalent circuit for the presence of Warburg (diffusional) impedance 33

3.11 Equivalent circuit models for analyzing EIS spectra: (a) a simple faradaic electrode process with inductance and (b) a metal coated with a porous, nonconductive film. 38

3.12 Factors affecting galvanic corrosion 41

5.1 Flat electrochemical cell 60

5.2 Schematic XAFS experiment in transmission mode 67

6.1 X-ray diffraction patterns of α- and β-Ta coatings, Ta foil (polished and unpolished) and Ta powder 74

6.2 Surface plot of Ta coatings obtained by AFM 76

LIST OF FIGURES
(Continued)

Figure **Page**

6.3 SEM images showing defects observed on (a) 5 μm thick α-Ta coating; (b) 10 μm thick α-Ta coating; (c) 5 μm thick β-Ta coating; (d) 10 μm thick β-Ta coating; (e) 50 μm thick α-Ta coating; (f) 100 μm thick α-Ta coating. 77

6.4 Evolution of galvanic current density measured from different ratios of cathodic (Ta foil) to anodic (AISI 4340 steel) areas in deaerated 0.5 M H_2SO_4 with N_2 at room temperature during 24 h. 79

6.5 Anodic polarization curves of α- and β-Ta coatings with different thicknesses, Ta foil, and steel substrate (AISI 4340) in deaerated 0.5 M H_2SO_4 purged with N_2 at room temperature. 80

6.6 Typical SEM images of thin Ta coating (α-phase and 5 μm thickness) showing the corrosion of the steel substrate through defects and propagation of cracks initiated from defects after potentiodynamic polarization measurements in deaerated 0.5 M H_2SO_4 purged with N_2 at room temperature. Arrows indicate location of the elements detected with EDX. 83

6.7 Impedance spectra of Ta foil after different immersion time and AISI 4340 steel for 1 h exposure in deaerated 0.5 M H_2SO_4 purged with N_2 at room temperature. 87

6.8 Impedance spectra of the 100 and 50 μm α-Ta coatings after different immersion time in deaerated 0.5 M H_2SO_4 purged with N_2 at room temperature. 88

6.9 Typical impedance spectra of thin α- and β-Ta coatings (10 μm thickness) after different immersion time in deaerated 0.5 M H_2SO_4 purged with N_2 at room temperature. 90

6.10 FE-SEM images of the surface and cross sections of thin α- and β-Ta coatings after the EIS measurement. 91

6.11 Equivalent circuit models to fit experimental EIS data: (a) used for Ta foil and the 50 and 100 μm α-Ta coatings and (b) used for thin α- and β-Ta coatings. 92

6.12 R_p of Ta foil and R_{tot} of the 50 and 100 μm α-Ta coatings as a function of time. Error bars not visible are present within symbol. 94

LIST OF FIGURES
(Continued)

Figure **Page**

6.13 R_{ps} and R_{po} of thin Ta coatings as a function of time. Error bars are within the symbols. 96

6.14 Schematic of two models for depicting the relationship between pore resistance (R_{po}) and polarization resistance (R_{ps}) of the steel substrate at open pores: (a) both R_{po} and R_{ps} decrease with time and (b) mainly R_{ps} decreases with time. 97

7. 1 X-ray diffraction patterns of α-Ta coatings on the smooth and rough steel substrates and Ta powder. XRD patterns are normalized with respect to the peak with maximum intensity in each spectrum. 103

7.2 Fourier transforms of Ta L_{III}–edge $\chi(k)k^3$ spectra of α-Ta coatings on the smooth and rough steel substrates over the k range 2.85 – 16.3 Å. Ta L_{III}–edge $\chi(k)k^3$ spectra is shown in the insert. 104

7.3 AFM surface plots of the smooth and rough steel substrates (a, b) and α-Ta coatings on these substrates (c – f). Scans (a – d) were performed over 100 × 100 μm^2 area and scans (e – f) over for 2 × 2 μm^2. The vertical, z scale, unit is 5 μm for (a – d) and 200 nm for (e, f). 106

7.4 SEM images of α-Ta coatings (50 μm thick) on the smooth and rough steel substrates showing droplet like defects; (a) α-Ta coating on smooth steel substrate and (b) β-Ta coating on rough steel substrate. 107

7.5 Anodic polarization curves of smooth and rough steel substrates (AISI 4340), α-Ta coatings deposited on these substrates and of Ta foil, in 0.5 M H_2SO_4 deaerated with N_2 at room temperature. 109

7.6 Impedance spectra of α-Ta coatings for different immersion time in deaerated 0.5 M H_2SO_4 with N_2 at room temperature; (a) and (b) represent α-Ta coatings on smooth steel substrate; (c) and (d) α-Ta coatings on rough steel substrate. 112

7.7 Equivalent circuit models for fitting experimental EIS data of Ta foil and α-Ta coatings. 114

7.8 R_p and R_{tot} of Ta foil and α-Ta coatings on the smooth and rough steel substrates as a function of time. Error bars not visible are present within symbol. 115

LIST OF FIGURES
(Continued)

Figure **Page**

8.1 X-ray diffraction patterns of electrodeposited Cr and sputtered Cr coatings and sputtered α- and β-Ta coatings. 122

8.2 (a) Cr *K*-edge $\chi(k)k^3$ spectra of PVD and ED Cr coatings and Cr foil. (b) Fits to Fourier transforms of $\chi(k)k^3$ spectra over the k range 2.4 – 15.7 $Å^{-1}$. 123

8.3 Ta L_{III}-edge $\chi(k)k^3$ spectra of PVD α- and β-Ta coatings. (b) Fourier transforms over the k range 3.1 – 15.4 $Å^{-1}$ for α-Ta coating and 3.5 – 14.1 $Å^{-1}$ for β-Ta coating. 126

8.4 SEM images of electrodeposited Cr (a, b) and sputtered Cr (c, d) coatings. 127

8.5 SEM images of sputtered α-Ta (a, b) and β-Ta (c, d) coatings. 128

8.6 Impedance spectra of sputtered α-Ta and β-Ta coatings for different immersion time in deaerated 0.5 M H_2SO_4 with N_2 at room temperature. 130

8.7 Equivalent circuit model for fitting experimental EIS data of α-Ta and β-Ta coatings. (RE and WE are reference and working electrodes, respectively. R_{sol}: solution resistance, R_{po}: pore resistance, R_{ps}: polarization resistance of steel substrate, C_s: electrical double layer capacitance at steel/electrolyte interface, C_c: coating capacitance). 131

8.8 The evolution of fitted parameters of the equivalent circuit for α-Ta and β-Ta coatings. Error bars not visible are present within symbol. 132

8.9 Impedance spectra of electrodeposited Cr and sputtered Cr coatings for different immersion time in deaerated 0.5 M H_2SO_4 with N_2 at room temperature. 135

8.10 SEM images of electrodeposited Cr (a, b) and sputtered Cr (c) coatings after EIS measurement. 137

8.11 Anodic polarization curves of electrodeposited Cr and sputtered Cr coatings and the steel substrate (ASTM A723) after 1 h immersion in 0.5 M H_2SO_4 deaerated with N_2 at room temperature. 138

8.12 SEM images of electrodeposited Cr (a, b) and sputtered Cr (c, d) coatings after potentiodynamic polarization measurement. 139

LIST OF FIGURES
(Continued)

Figure **Page**

9.1 X-ray diffraction patterns of Ta_2O_5 powder; thermal Ta oxide at 800 °C for 1 hr, 400 °C for 3 hr and 0.5 hr; anodic Ta oxide; and α-Ta powder. 146

9.2 Optical image of thermally and anodically oxidized Ta foil. 147

9.3 SEM (left side) and AFM (right side) images of thermal Ta oxides at 800 °C for 1 hr and 400 °C for 3 and 0.5 hr and anodic Ta oxide. 148

9.4 Ta L_{III}–edge $\chi(k)k^3$ spectra of Ta_2O_5 powder, 800 °C-thermal Ta oxide, 400 °C-thermal Ta oxide films, anodic Ta oxide films, and Ta foil. 150

9.5 Fourier transforms of Ta L_{III}–edge $\chi(k)k^3$ spectra over the k range 2.2–15.2 Å. ... 152

9.6 Fits to Fourier transform ($\chi(k)k^3$) vs. radial coordinate over the R range 0.92 – 2.04 Å of Ta_2O_5 powder transmission spectra at 298 and 77 K and the thermal Ta oxide (800 °C for 1hr) fluorescence spectra at 298 K. 153

9.7 Ta L_{III}–edge $\chi(k)k^3$ spectra fitting with linear combination of the Ta_2O_5 and Ta spectra to the Ta oxide films (400 °C for 3 and 0.5 hr) over k range of 2.2 – 15.5 $Å^{-1}$. 156

9.8 Ta L_{III}–edge $\chi(k)k^3$ spectra fitting using linear combination of the Ta_2O_5 and Ta spectra to the anodic Ta oxide films over k range of 2.0 – 15.5 $Å^{-1}$ 157

9.9 Contribution of the two model spectra, β-Ta_2O_5 and Ta, in fitting the Ta L_{III}–edge $\chi(k)k^3$ spectra of anodic oxide films with various oxide thickness. The linear relationship is depicted by the solid line. 158

CHAPTER 1

INTRODUCTION

Chromium coatings have a long history of being used as protective coatings against erosion and corrosion of gun bore. Specifically electroplated chromium offers corrosion protection in various environments because of its oxide layer and it's useful in applications in wear resistance [1, 2]. However, because hexavalent chromium is now known to be toxic and associated wastes are hazardous and difficult to dispose of, its use is being discontinued [3]. Therefore, as an environmentally friendly coating and as dictated by the U. S. Army, tantalum deposited by sputtering, one form of plasma-assisted vapor deposition (PVD) is under development to replace chromium due to its high ductility and corrosion resistance [2, 4-6]. Currently, NJIT along with DOD facilities such as Benet Laboratory is investigating sputtered tantalum. When deposited as a film on steel substrates, more than one phase of tantalum is observed to form: one is α-phase, which is stable and ductile, and the other is β, which is meta-stable and brittle. As listed in Table 1.1, the α-phase tantalum has a body centered cubic (bcc) structure, while β-phase has been reported to be tetragonal, however, its structure and physical properties are under investigation [7-11]. Both α- and β-phases have been observed under varying deposition conditions by sputtering. Because of the brittle nature and metastability of the β-phase, α is preferred for the purpose of protecting the gun bore against erosion.

A metal coating deposited without impurities or discontinuities should exhibit a corrosion behavior comparable to that of the bulk metal. However, it is generally not

Table 1.1 Properties of Tantalum

Tantalum	Density (g/cm^3)	Resistivity ($\mu\Omega$-cm)	Structure	Ref.
Bulk tantalum (α-phase)	16.555	13	bcc a=3.303 Å	[12]
Sputtered α-phase tantalum	16.27-16.55	24-50	bcc a=3.31-3.33 Å	[12]
Sputtered β-phase tantalum	16.9	180-220	tetragonal a=5.313 Å c=10.194 Å	[13]

feasible to achieve such a perfect coating in practice. Consequently, the major problem of protective coatings in aggressive environments results from the potential presence of defects, such as open pores in the coatings. If the coating is anodic to the substrate, porosity is not a critical problem because cathodic protection of the substrate is achieved. However, when the coating is cathodic to the substrate, defects lead to a rapid localized galvanic attack at the coating/substrate interface and pitting corrosion of the substrate occurs [14, 15]. Therefore, evaluating porosity is critical in assessing the corrosion performance of the coating. Electrochemical techniques have been applied to assessing porosity and its effect on corrosion behavior [14-16]. An increase in coating thickness reduces the porosity regardless of the coating method [14]. When tantalum is in electrical contact with most other metals including steel, it tends to become cathodic. Because of this cathodic behavior, atomic hydrogen, which is liberated through the electrochemical reaction, can be absorbed causing hydrogen embrittlement in the coating [17]. Therefore,

if the tantalum coating on a steel substrate contains defects, especially open pores, the galvanic effect will be introduced, accelerating the corrosion process as well as inducing hydrogen embrittlement.

The overall objective of this study is to understand the corrosion behavior of tantalum coatings, which includes

- Assessing the effect of coating thickness on corrosion as a function of immersion time in order to obtain the critical thickness as a protective barrier;
- Evaluating the impact of substrate surface roughness on corrosion resistance of coating, as surface modification (i.e., polishing) is not feasible in a full-scale process;
- Comparing the performance of Ta versus Cr coatings produced in full-scale operation; and,
- Determining structural properties of the passive Ta oxide film to assist in better understanding its unique properties that provide an effective corrosion barrier.

Electrochemical techniques are critical in evaluating the porosity of tantalum coatings. In addition, the corrosion rate, polarization behavior, and impedance behavior have been investigated for tantalum coatings as a function of time in a corrosive medium. Complementary analyses to supplement these studies include x-ray absorption fine structure spectroscopy (XAFS), x-ray diffraction (XRD), scanning electron microscopy (SEM), and atomic force microscopy (AFM).

In the next chapter, background on Ta chemistry and properties are discussed with respect to corrosion. In subsequent chapter electrochemistry and electrochemical techniques are reviewed and followed by the research objectives, approach, and methods.

Results from the experiments are then presented in chapters 6 through 9. The dissertation concludes with overall concludes and future research.

CHAPTER 2

CORROSION RESISTANCE OF TANTALUM

Known as one of the most corrosion resistant metals, tantalum is an element of Group V B of the Periodic Table exhibiting a strong electronegative property due to its electronic configuration, as do elements in Groups IV B and VI B. This strong electronegativity makes metals in these groups reactive. Because of this high reactivity, an extremely stable oxide of tantalum is formed at ambient temperatures and provides what is considered a chemical inertness for tantalum [18]. In addition, tantalum itself is an active metal from an electrochemical point of view since its domain of thermodynamic stability is found to lie below that of water reduction at all temperatures from 25 to 300 °C [19]. The standard redox potential (E_H^0) of tantalum is less than zinc [20]. However, once passivated, its oxide film places tantalum below rhodium and above gold in the Pourbaix practical nobility table [20]. Therefore, the high corrosion resistance and inertness of tantalum is attributed to a very thin, impervious, protective oxide film [21]. Although tantalum pentoxide is the most thermodynamically stable oxide form, metastable suboxides exist in transition between the metal and the outer film [22, 23].

Bulk tantalum pentoxide powder has a very high melting point of 1784 °C with a density of 8.2 g/cm^3. The dielectric constant ranges from 24 to 65 depending on the structural phase [24]. Physical and chemical properties of other tantalum oxides such as TaO and TaO_2, which are metastable suboxides, are not well known; however, TaO_2 has a reported density of 10.0 g/cm^3 [24]. The structural information of tantalum suboxides and tantalum pentoxide is listed in Table 2.1.

Table 2.1 Structural information of tantalum suboxides* and tantalum pentoxide

Formula	Structure	Lattice Constant (Å)	Preparation	Ref.
Ta_3O_9	Monoclinic tantalum oxide, P_{2h}^5	a=6.30, b=12.03, c=3.75, γ=106°55'	Evaporating pure Ta in a vacuum of 5×0^{-5} mm Hg with subsequent annealing of the films for 3 h, first in a flow of helium and then in air at 600°C.	[26]
TaO_2	Tetragonal, rutile type	a_r=4.709, c_r=3.065	No details	[27]
TaO_{2-x} ($0\leq x<1$)	$I4_1/a$, Tetragonal	a=13.32, c=6.12, ($a=2\sqrt{2}\,a_r$, $c=2\,c_r$)	Oxidation of thin films of tantalum in vacuum (1×10^{-4} to 5×10^{-6} mmHg) at 600 °C to 700 °C	[27]
$Ta_4O_{\sim5.6}$ and $2Ta_2O_{\sim3}$	Face centered cubic	a=5.10	Annealing of thin films of tantalum in air, oxygen and in a vacuum of 10^{-3} mmHg at ~700-750 °C and 500-550 °C.	[28]
γ-TaO	Face centered cubic	a_1=4.38, a_2=4.44 (after annealing)	Evaporate from a metal plate onto a NaCl crystal at 10^{-5} to 10^{-6} mm Hg, annealing the films at up to ~400 °C.	[29]
β-Ta_2O_5	Orthorhombic	a=6.20, b=3.60, c=3.89	Anodic oxidation of tantalum in aqueous electrolytes, then annealing amorphous Ta_2O_5 at 1100 °C for 8 hours	[30]
β-Ta_2O_5	Orthorhombic	a=6.325, b=31.6178, c=4.031	Heating tantalum oxalate solution in air at 100 °C for 8 hours then quenched	[31]
δ-Ta_2O_5	Hexagonal	a=7.16, c=11.52	Oxidation of thin tantalum film (100-150Å) in air at 600-900 °C for 1-8 hours	[32]

* The formulas do not reflect the true valence of the atoms in the compound due to the deficit.

Because of the dielectric behavior of tantalum oxide and hence its application to microelectronics, a great deal of studies have been conducted on Ta_2O_5 thin film production by various methods such as anodic oxidation, thermal oxidation, and chemical- and physical- vapor deposition (Table 2.2). Crystalline Ta_2O_5 exhibits a higher dielectric constant than amorphous Ta_2O_5 of which the dielectric constant was observed to be in the range of 22 to 28 [25]. The high dielectric constant values of Ta_2O_5 (either amorphous or crystalline) compared to those (3.7 – 9.5) of glasses demonstrate the importance of tantalum oxide as a barrier in the electrochemical reaction between tantalum and the electrolyte. Etching rates of tantalum pentoxide as thin films (Table 2.3) reveal that they are more easily etched as the deposition temperature decreases. This effect may be due to increased porosity with decreasing deposition temperature and increased crystallinity with increasing deposition temperature. Annealing Ta_2O_5 films potentially leads to a densification of the films, thus reducing the etching rate.

Some researchers [39, 40] have reported that corrosion rates for bulk tantalum in various aqueous, acid, and alkali media are generally less than 5 μm per year. Table 2.4 shows the corrosion resistance of electroplated hard chromium (Cr) and refractory metals including Nb, Ta, Ti, and Zr. Unlike most corrosive media, fluorine, hydrofluoric acid and solutions containing fluoride ions are aggressive environments in which tantalum corrodes even at ambient temperature; exposure results in attack of the tantalum oxide through dissolution and the metal is transformed from a passive to an active state [41]. When tantalum becomes passive by the formation of the oxide film, it occupies a high position toward the electropositive end of the electromotive series, and

Table 2.2 Density and dielectric constant of Ta_2O_5 thin films

Sample preparation	Density (g/cm^3)	Dielectric constant	Ref.
Anodization (H_2SO_4)	7.93 ± 3 %	27.6 ± 5 % (400 nm thick)	[33]
Anodization (citric acid)	8.01 ± 0.08	26.2	[12]
Thermal oxidation	4.7 (12.5 nm thick) 7.3 (110.7 nm thick) -	- - 26 ± 2 (10-100 nm thick)	[34] [35]

Table 2.3 Etching rates of Ta_2O_5 thin films in various solutions

Sample preparation	Solutions	Etching rate (nm/min)	Ref.
Anodic oxidation in H_2SO_4	Concentrated HF saturated with NH_3F	2.5 to 15 (amorphous Ta_2O_5)	[36]
LPCVD (low pressure CVD)	25% HF	0.7, deposition temp. 490 °C (amorphous Ta_2O_5) 4, deposition temp.350 °C (amorphous Ta_2O_5) no etching (crystalline Ta_2O_5) annealed in dry-O_2 at 800 °C	[37]
LPCVD	6 M HCl	No etching (amorphous and crystalline Ta_2O_5)	[38]

CVD is defined as chemical vapor deposition.

Table 2.4 Corrosion resistance of refractory metals in various corrosive media [45]

Media	Conc. (wt.%)	Temp. (F)	Cr (mpy)	Nb (mpy)	Ta (mpy)	Ti (mpy)	Zr (mpy)
Acetic acid	10	135	15	-	-	-	-
Acetic acid	50	Boiling	-	Nil	Nil	Nil	Nil
HCl	5	200	Rapid attack	1	Nil	<100	Nil
HCl	30	200	-	5	Nil	Rapid	Nil
HNO_3	10	135	12	-	-	-	-
HNO_3	65	Boiling	-	<2	<2	<2	<2
NaOH	10	Room	Nil	*	*	Nil	Nil
H_2SO_4	10	55	11	-	-	-	-
H_2SO_4	40	Boiling	-	20	Nil	rapid	3
H_2SO_4	98	Boiling	-	attacked	<2	rapid	<200
HF**	1-100	Room	-	attacked	attacked	rapid	50<

* Material may become brittle due hydrogen absorption

mpy- milliinch per year

tends to become cathodic in the galvanic cell formed in contact with all other metals. Because of this cathodic behavior, atomic hydrogen that is liberated can be absorbed by tantalum resulting in hydrogen embrittlement [41-42], which has been extensively studied in the galvanic coupling of tantalum with other metals including platinum, silver, copper, molybdenum, nickel, lead, zinc, and aluminum in 0.1 N H_2SO_4. Haissinsky [42] found that tantalum became anodic except when coupled with zinc or aluminum and that the galvanic current rapidly decreased as tantalum passivated. However, when tantalum

was exposed to hydrofluoric acid and coupled with other metals except zinc or aluminum, the galvanic current was observed to reach an elevated steady-state current because tantalum became active rather than passivated. Therefore, the corrosion resistance of tantalum appears to depend on the interaction between the passive film and corrosive environment.

The electrochemical behavior of bulk tantalum with respect to the anodic oxide film has been investigated by many researchers [23, 33, 43, 44, 46]. Young [33] reported that the anodic oxide film on tantalum grows linearly with increasing electrode potential through high field ion migration. Additionally, Lehovec and D'Amico [44] investigatedthe spontaneous growth of thin (6-20 Å) oxide films formed on tantalum immersed in H_2SO_4, NaCl, and NaOH solutions at the corrosion (free corroding) potential. They observed that the oxide thickness after an initial growth period increased linearly with the logarithm of time. Vermilyea [47] showed that the relationship between ion current and electrical field strength for anodic oxide formation on tantalum was not affected by the crystallographic orientation of the metal surface. In his experiment, a large-grained (arc-melted) tantalum was anodically oxidized at a constant current to about 300 V. No variation of the oxide thickness was observed on different crystals or differently oriented regions of the same crystal at any time during the period of growth. Although the oxide growth has been studied to some degree, its properties with respect to corrosion are not well understood. Therefore, this research will conduct the unique characteristics of Ta oxide films.

Furthermore, this research aims to assess the effect of coating thickness on defects, which are intrinsic to PVD coatings. Once the corrosion behavior is understood,

a comparison of the Ta versus Cr coatings is considered with full-scale processes. In the next chapter background is presented on electrochemistry and electrochemical techniques in evaluating corrosion.

CHAPTER 3

BACKGROUND

3.1 Electrochemical Theory on Corrosion

Electrochemically corrosion is the deterioration of metal through a chemical or electrochemical action, starting at its surface. This chapter reveals electrochemistry and electrochemical techniques covering reactions, thermodynamics and kinetics. Complex processes occurring in corrosion are addressed with an overview of electrochemical data analysis.

3.1.1 Electrochemical Reaction in Aqueous Corrosion

The fundamental corrosion process is illustrated in Figure 3.1. The overall reaction involves electron transfer at the interface between metal surface and electrolyte where metal undergoes oxidation:

$$M \rightarrow M^{m+} + me^{-} \tag{3.1}$$

and cathodic half-cell reaction, where an oxidizing agent is reduced:

$$X^{n+} + ne- \rightarrow X \tag{3.2}$$

The overall reaction becomes:

$$M + \frac{m}{n} X^{n+} \rightarrow M^{m+} + \frac{m}{n} X \tag{3.3}$$

The anodic and cathodic reactions take place simultaneously. Uniform corrosion occurs when the anodic and cathodic reactions are in the same area such that polarization reversal occurs. When anodic and cathodic sites do not vary with time, localized

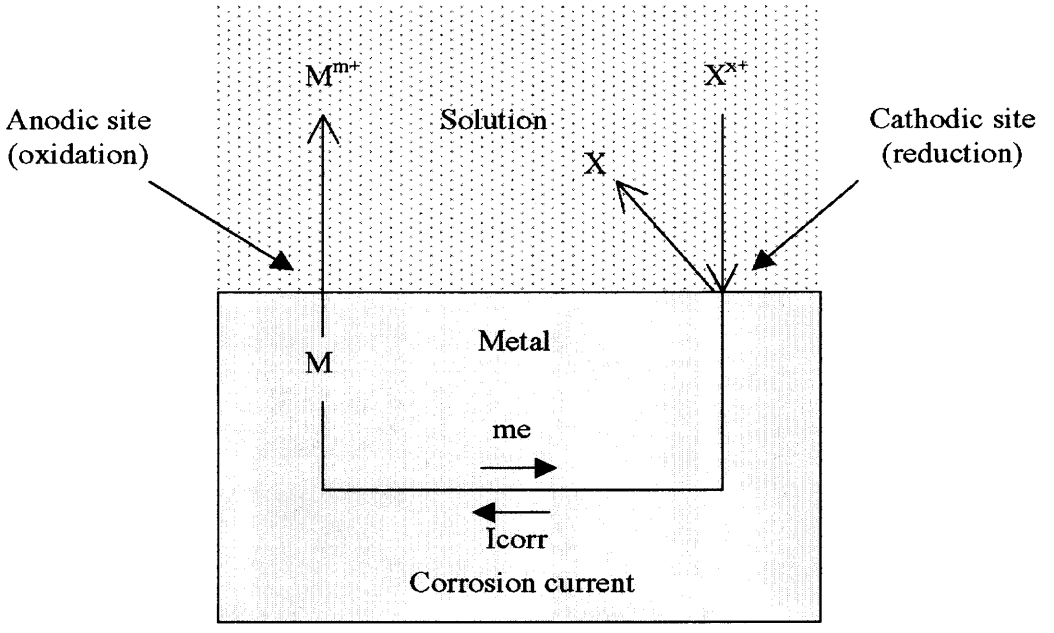

Figure 3.1 Basic corrosion process occurring on the metal surface [48].

corrosion such as pitting is observed.

Two common cathodic reactions are the hydrogen evolution and the oxygen reduction reaction. When dissolved oxygen is not present in the aqueous solution, the cathodic reaction is:

$$2H^+ + 2e^- \rightarrow H_2 \quad \text{at pH} < 7 \tag{3.4}$$

$$2H_2O + 2e^- \rightarrow 2OH^- + H_2 \quad \text{at pH} \geq 7 \tag{3.5}$$

When dissolved oxygen is present in the solution, the following reactions apply:

$$O_2 + 4H^+ + 4e^- \rightarrow 2H_2O \quad \text{at pH} < 7 \tag{3.6}$$

$$O_2 + 2H_2O + 4e^- \rightarrow 4OH^- \quad \text{at pH} \geq 7 \tag{3.7}$$

The rate of this reaction is expressed as a current density since there is a linear correspondence between the flux of ions and the flux of electrons.

3.1.2 Electrochemical Thermodynamics

The direction in which an electrochemical reaction proceeds spontaneously is determined by thermodynamics. A reaction goes in the direction that minimizes its Gibbs-Free Energy. Corrosion in aqueous solutions has been found to involve electron or charge transfer. Thermodynamics gives an understanding of the energy changes involved in the electrochemical reactions of corrosion. These energy changes provide the driving force and control the spontaneous direction for a chemical reaction. Thermodynamics can only tell us the direction in which a reaction will occur, not the rate.

3.1.2.1 Free Energy and Electrode Potential The free-energy change, ΔG, is related to the electrochemical potential, E, at equilibrium, by the following equation [49]:

$$\Delta G = -nFE \tag{3.8}$$

where:

ΔG is the change in Gibb's Free Energy [J/mol]

n is the number of electrons (or equivalents) transferred in the reaction [eq/mol]

F is Faraday's conatant, 96,485 [C/eq]

E is the potential [V]

3.1.2.2 Concentration Effects on Electrode Potential The standard state requires all reactants and products to be at unit activity. Thus, some means must be provided to

calculate half-cell electrode potentials that deviate from the standard state. Considering a general half-cell reaction as follow:

$$aA + mH^+ + ne^- \leftrightarrow bB + dH_2O \tag{3.9}$$

Free-energy changes in the standard, ΔG^0, and nonstandard, ΔG, states are given for reaction (3.9) by

$$\Delta G^o = (bG_B^o + dG_{H_2O}^o) - (aG_A^o + mG_{H^+}^o) \tag{3.10}$$

$$\Delta G = (bG_B + dG_{H_2O}) - (aG_A + mG_{H^+}) \tag{3.11}$$

The departure of free-energy change in the nonstandard from the standard state is found from the difference

$$\Delta G - \Delta G^o = [b(G_B - G_B^o) + d(G_{H_2O} - G_{H_2O}^o)] - [a(G_A - G_A^o) + m(G_{H^+} - G_{H^+}^o)] \tag{3.12}$$

As for the reactant A, the corrected concentration, (A), available for reaction, called the activity of A, is related to free-energy change from standard state, $(G_A - G_A^o)$, by

$$a(G_A - G_A^o) = RT\ln(A)^a \tag{3.13}$$

where R is the gas constant and T is absolute temperature. Substituting the equation (3.13) and equivalent expressions for other reactants and products into equation (3.12) gives

$$\Delta G - \Delta G^o = RT\ln\frac{(B)^b(H_2O)^d}{(A)^a(H^+)^m} \tag{3.14}$$

which is equivalent to

$$E = E^o - \frac{RT}{nF}\ln\frac{(B)^b(H_2O)^d}{(A)^a(H^+)^m} \tag{3.15}$$

Equation (3.15) is the Nernst equation. For the convenience, this form is usually expressed as follows,

$$E = E^o + \frac{2.3RT}{nF}\log\frac{(A)^a(H^+)^m}{(B)^b(H_2O)^d} \tag{3.16}$$

which shows more readily that the half-cell electrode potential becomes more positive (noble) as activities of oxidized species, (H^+), increases. Thus potential is considered to be a measure of the oxidizing power of the solution.

When the potential of an electrode is greater than the equilibrium potential, this can be accomplished only by oxidation. If the electrode potential is lower than the equilibrium potential, the reaction can only occur by reduction.

3.1.2.3 Graphical Representation of Electrochemical Equilibrium The potential/pH diagram, which is known to be Pourbaix diagram [20], shows conditions of solution oxidizing power (potential) and pH for the various possible phases that are stable in an aqueous electrochemical system. Boundary lines on the diagram driving areas of stability for different phases are derived from the Nernst equation (3.16) at equilibrium. In Pourbaix diagram, the line labeled {a} represents the electrochemical evolution of hydrogen from decomposition of water as shown in Equations (3.4) and (3.5). For a potential more active than the half-cell electrode potential (E_{H^+/H_2}), hydrogen is evolved and water is unstable thermodynamically. Thus below line {a}, water is unstable and decomposes to H_2. Above the line, water is stable, and hydrogen gas, if present, is oxidized to H^+ or H_2O. As potential becomes further positive, another reaction involving water as shown in Equations (3.6) and (3.7) becomes thermodynamically feasible. The Nernst equation from these reactions produces the line {b}. At potentials positive to

E_{O_2/H_2O} at any pH, water is unstable and oxidized to O_2. Below the potential water is stable, and dissolved oxygen is reduced to water if present.

Pourbaix diagrams for Fe, Cr, and Ta are shown in Figure 3.2, 3.3, and 3.4, respectively. The shaded areas of Figure 3.2 and 3.3 show stability of soluble dissolution products, where the metal is subject to corrosion. Unshaded areas show either thermodynamic immunity or corrosion resistance due to the stability of an oxide film.

Figure 3.2 shows the domain of thermodynamic stability of iron, which is situated below the thermodynamic stability of water under atmospheric pressure (line {a}). Therefore metallic iron is not stable thermodynamically in the presence of 25 ^{o}C water under 1 atm pressure for the given pH range. Chromium shows corrosion resistance through passivation due to the presence of a resistant, protective oxidized surface film that is stable over a wide range of conditions. Tantalum is more resistant than iron and chromium: the passive oxide film is stable for the entire range of pH and potential shown. Thermodynamics tell us how conditions may be adjusted to make corrosion impossible. When corrosion is possible, thermodynamics cannot predict the rate. The actual rate of corrosion is governed by kinetics discussed in the following section.

3.1.3 Electrochemical Kinetics of Corrosion

Kinetics determines the rate at which electrochemical reaction occurs. This rate can either be controlled by the energy available to drive electron transfer, activation polarization, or the rate at which reactants migrate towards or away from the interface between electrode and electrolyte, otherwise known as concentration polarization.

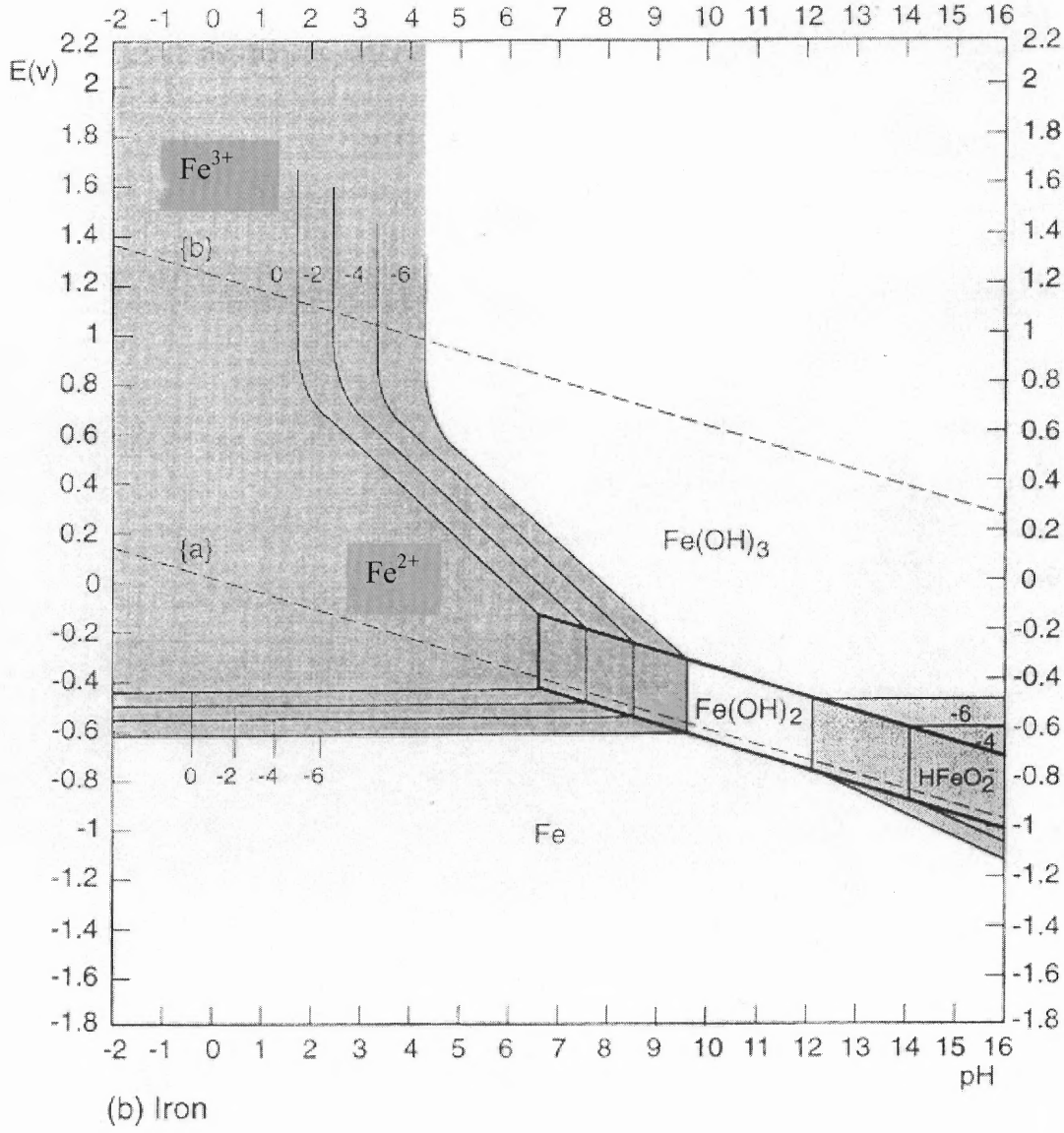

Figure 3.2 Potential – pH diagram for for Iron (Fe) at 25 °C. Dark area indicates corrosion susceptibility. Labels 0, -2, -4, and –6 are the log of solution ion activity for the indicated lines [20].

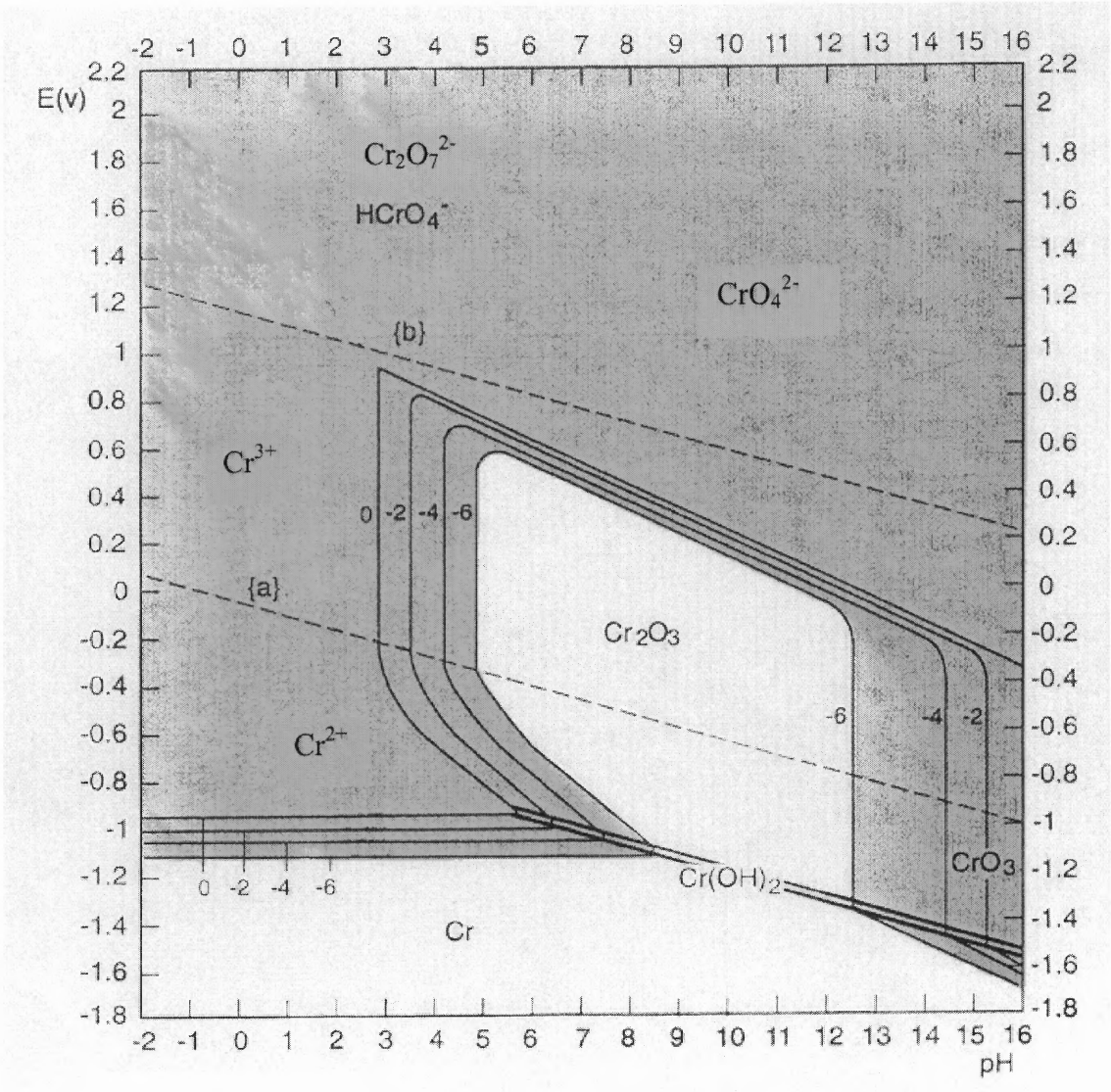

Figure 3.3 Potential – pH diagram for for Cr at 25 °C. Dark area indicates corrosion susceptibility. Labels 0, -2, -4, and –6 are the log of solution ion activity for the indicated lines [20].

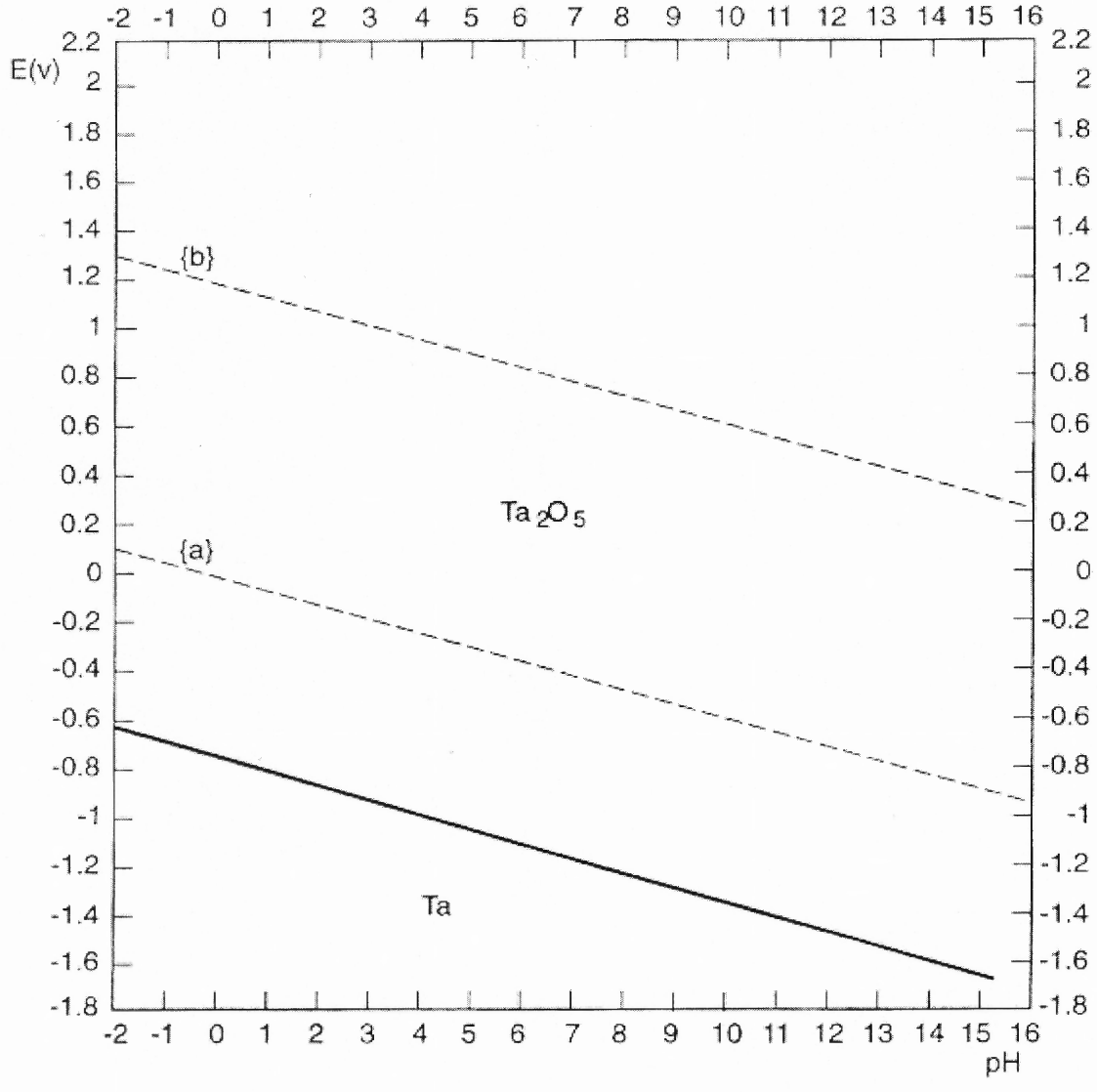

Figure 3.4 Potential – pH diagram for tantalum/water system at 25 °C [20].

3.1.3.1 Activation Polarization Polarization, η, is the potential change, E-E^o, from the equilibrium half-cell electrode potential, E^o, caused by a net surface reaction rate for the half-cell reaction. For anodic polarization, electrons are removed from the metal, a deficiency results in a positive potential change due to the slow liberation of electrons by the surface reaction, and anodic overpotential, η_a, becomes positive. For cathodic polarization, η_c, electrons are supplied to the surface, and a buildup in the metal due to the slow reaction rate causes the surface potential, E, to become negative to E^o. Therefore, η_a is negative by definition.

When a step in the half-cell reaction controls the rate of charge (electron) flow, the reaction is said to be under activation or charge transfer control, and activation polarization results. As shown in Figure 3.5, the Tafel relationships between activation polarization or overpotential, η, and the rate of the reaction represented by current density, i, are

$$\eta_a = \beta_a \log\frac{i_a}{i_o} \tag{2.17a}$$

for anodic polarization, and

$$\eta_c = \beta_c \log\frac{i_c}{i_o} \tag{2.17b}$$

for cathodic polarization

where

η is the overpotential [V]

β is the Tafel constant for half-cell reaction [V/decade]

i is the current density [A/cm^2]

The subscripts a and c represent anode and cathode, respectively.

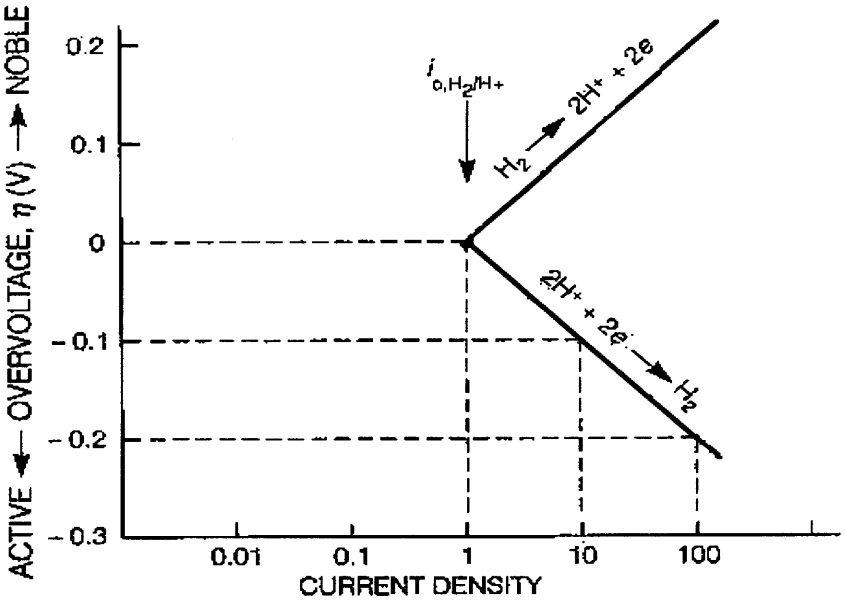

Figure 3.5 Activation overpotential showing Tafel behavior [39].

Taking reaction (3.4) as an example, the half-cell electrode potential, E_{H^+/H_2}, is established when the reaction is at equilibrium. The rate of discharge of H^+ (forward reaction) balances the rate of ionization of H_2 (reverse reaction). The presence of overpotential indicates the presence of energy barriers (activation energies) and the activation energy difference is related to half-cell electrode potential by the following;

$$\Delta G_f^* - \Delta G_r^* = \Delta G_{H^+/H_2} = -nFE_{H^+/H_2} \tag{3.18}$$

where ΔG_f^* and ΔG_r^* are activation energies of the forward and reverse reactions, respectively. The forward and reverse reaction rates as a function of the respective activation energies are expressed as follows:

$$r_f = k_f \exp\left[-\frac{\Delta G_f^*}{RT}\right] \tag{3.19}$$

and

$$r_f = k_r \exp\left[-\frac{\Delta G_r^*}{RT}\right] \tag{3.20}$$

where K_f and K_r are the reaction rate constants for the forward and reverse reactions, respectively. At equilibrium,

$$r_f = r_r = \frac{i_o a}{nF} \tag{3.21}$$

where i_o is exchange current density and a is the atomic weight.

Therefore, the following equation demonstrates that exchange current density is a function of the activation energies.

$$i_o = k_f' \exp\left(-\frac{\Delta G_f^*}{RT}\right) = k_r' \exp\left(-\frac{\Delta G_r^*}{RT}\right) \tag{3.22}$$

When a cathodic overpotential, η_c, is applied to the electrode, the discharge reaction rate in terms of current density becomes

$$i_c = k_f^* \exp\left[-\frac{\Delta G_f^* - \alpha n F \eta_c}{RT}\right] \tag{3.23}$$

and the anodic reaction rate becomes

$$i_a = k_r^* \exp\left[-\frac{\Delta G_r^* + (1-\alpha) n F \eta_c}{RT}\right] \tag{3.24}$$

The factors α and (1-α) in Equation (3.23) and (3.24) are the fractions of η_c taken by the forward and reverse reactions, respectively. The net applied current density is

$$i_{app,c} = i_c - i_a = i_o \exp\left[\frac{\alpha nF\eta_c}{RT}\right] - i_o \exp\left[\frac{-(1-\alpha)nF\eta_c}{RT}\right] \tag{3.25}$$

Similarly, for an applied anodic current density is

$$i_{app,a} = i_a - i_c = i_o \exp\left[\frac{\alpha nF\eta_a}{RT}\right] - i_o \exp\left[\frac{-(1-\alpha)nF\eta_a}{RT}\right] \tag{3.26}$$

where α is the fraction of η_a taken by the anodic reaction. For high values of η_c and η_a, Equations (3.25) and (3.26) with $\beta = 2.3RT/\alpha nF$ become Equations (3.17b) and (3.17a), respectively.

3.1.3.2 Concentration Polarization As a reaction proceeds it consumes reactants and generates products. Either a lack of reactants or an excess of products can impede a reaction and slow its rate. The magnitude of this slowing rate can be found by using the limiting current densities for both the anodic and cathodic reactions. The equations of the anodic and cathodic mass transfer polarization are as follows [50, 51].

$$\eta_{conc,a} = -\frac{2.3RT}{nF}\log\left[1 - \frac{i_a}{i_L}\right] \tag{3.27}$$

and

$$\eta_{conc,c} = \frac{2.3RT}{nF}\log\left[1 - \frac{i_c}{i_L}\right] \tag{3.28}$$

where

$\eta_{conc,\ a}$ and $\eta_{conc,\ c}$ is the anodic and cathodic concentration polarizations, respectively.

i_L is the limiting current density.

The limiting current density can be calculated from

$$i_L = \frac{DnFC_B}{\delta} \tag{3.29}$$

where:

D is the diffusivity of the reacting species.

C_B is the bulk concentration of the reacting species.

δ is the thickness of the diffusion layer.

Limiting diffusion current density is usually only significant during reduction processes and is negligible during metal dissolution reactions [39]. Therefore, concentration polarization is important when reduction is large enough to place it under diffusion control.

3.1.4 Mixed Electrode

During the corrosion of an electrically isolated metal sample, the total rate of oxidation must equal the total rate of reduction. The only point in this system where the total rates of oxidation and reduction are equal is at the intersection represented by a mixed or corrosion potential, E_{corr}. At this point the rate of iron dissolution is equal to the rate of hydrogen evolution expressed in terms of current density as shown in Figure 3.6.

Electrochemical techniques to assess the free corroding potential, corrosion current density, and polarization curve are discussed in the following sections.

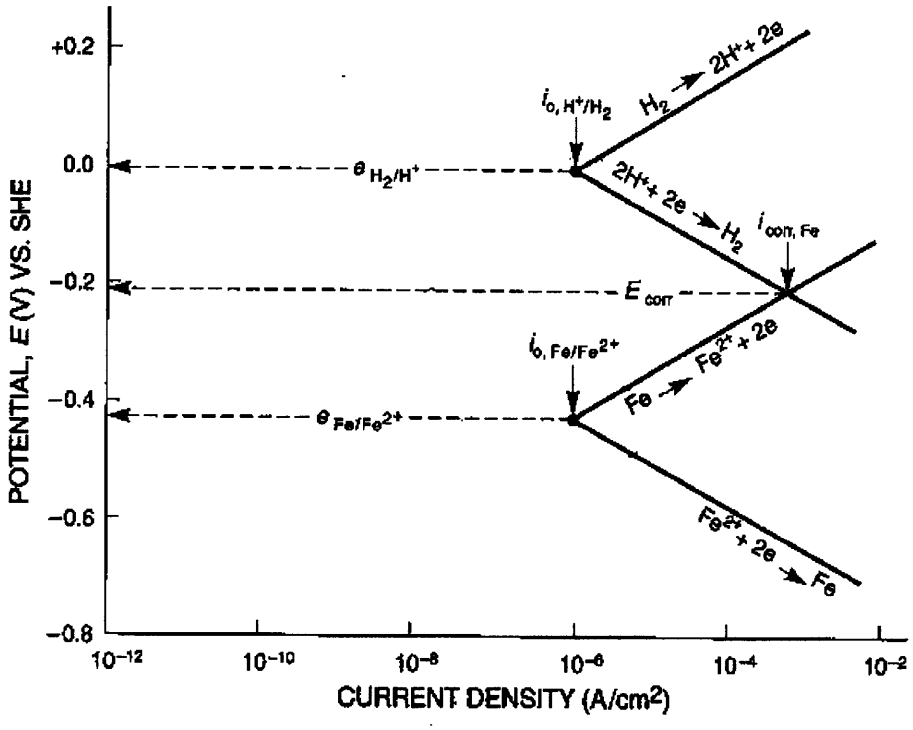

Figure 3.6 Polarization of anodic and cathodic half-cell reactions for iron in acid solution to give a mixed potential, E_{corr}, and a corrosion rate (current density), i_{corr}. [39].

3.2 Electrochemical Impedance Spectroscopy

Electrochemical impedance spectroscopy is a powerful tool for evaluating reaction mechanisms involving for example multistep charge transfer, diffusion, intermediate adsorption steps, and growth of a new phase [52-54]. This section reviews the theory behind electrochemical impedance spectroscopy [48, 55, 56].

To assess corrosion rates, electrochemical techniques including the EIS method are widely employed. The main use of electrochemical techniques is to estimate the

polarization resistance, R_P, for the calculation of the corrosion current density, i_{corr}, using the Stern-Geary relationship [57]

$$i_{corr} = \frac{\beta_a \beta_c}{2.303 R_p (\beta_a + \beta_c)} \tag{3.30}$$

where β_a and β_c are the Tafel constants for the anodic and cathodic reactions, respectively. The corrosion rate is inversely proportional to the polarization resistance.

Electrochemical impedance spectroscopy is based on and developed from ac impedance theory. In general, the ac impedance method involves application of time-varying, small, potential perturbations about E_{corr}, measurement of current response and determination of the system impedance, Z, and the impedance phase angle, δ, over a frequency range. The applied ac potential is normally sinusoidal. In the EIS measurement, a small amplitude signal, usually a voltage between 5 and 50 mV is applied to a specimen over a range of frequency between 1 mHz and 100 kHz [55, 58]. At the highest frequencies (>150 kHz), measurements can be affected by phase shifts arising from the potentiostat [59] and at low frequencies the practical limit is often determined by the stability of the electrode as the longer scanning time may represent multiple mechanisms [55]. In the analysis, the impedance of the system, Z, and phase angle between the impedance and the applied potential, δ, are determined as a function of applied frequency. These quantities are then interpreted in relationship to the electrochemical, chemical, and physical processes associated with the cell.

One of the simplest linear equivalent circuits for a metal-solution interface as shown in Figure 3.7 consists of three elements: polarization resistance (R_P), solution resistance (R_{sol}), and the electrical double layer capacitance (C_{dl}). The values of these

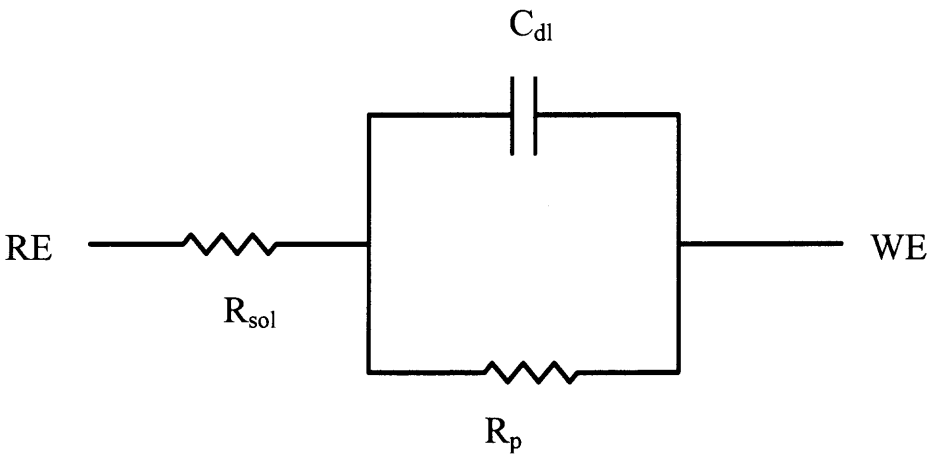

C_{dl}: capacitance of electrical double layer

R_p: polarization resistance of working electrode

R_{sol}: uncompensated solution resistance

RE and WE are reference electrode and working electrode, respectively

Figure 3.7 Equivalent circuit for a simple corroding system with a solution resistance.

three components are generally normalized with respect to electrode area. Physically, the capacitance relates to ions and polar molecules in the electrolyte that undergo charge redistribution and hence produce a current under time-varying potentials, but not after a decay time at constant potentials (steady-state condition). In addition there is a solution resistance between the reference electrode, or Luggin tip, and the metal electrode.

The impedance of the simple equivalent circuit after mathematical treatment becomes:

$$Z = R_{sol} + \frac{R_P}{(\omega^2 C^2 R_P^2 + 1)} - \frac{j\omega C R_P^2}{(\omega^2 C^2 R_P^2 + 1)} \tag{3.31}$$

where ω is angular frequency ($\omega = 2\pi f$)

or

$$Z = Z' + jZ'' \tag{3.32}$$

where

$$Z' = R_{sol} + \frac{R_P}{(\omega^2 C^2 R_P^2 + 1)} \tag{3.33}$$

and

$$Z'' = \frac{-\omega C R_P^2}{(\omega^2 C^2 R_P^2 + 1)} \tag{3.34}$$

Z' and Z'' are the real and imaginary components of the equivalent impedance. The modulus, $|Z|$, of the system impedance is:

$$|Z| = \left[(Z')^2 + (Z'')^2\right]^{\frac{1}{2}} = \left[R_{sol}^2 + \frac{2R_{sol}R_P}{(\omega^2 C^2 R_P^2 + 1)} + \frac{R_P^2}{(\omega^2 C^2 R_P^2 + 1)}\right]^{\frac{1}{2}} \tag{3.35}$$

The impedance phase angle is given by:

$$\tan\delta = \frac{Z''}{Z'} = \frac{-\omega C R_P^2}{R_{sol} + R_P + R_{sol}(\omega C R_P)^2} \tag{3.36}$$

The impedance data are often presented by either the Nyquist impedance plot or Bode plot. The Nyquist plot is a complex plane one, which displays the imaginary, Z'', part versus real, Z', part of the impedance as shown in Figure 3.8. Each point on the plot corresponds to the impedance at one frequency. At the high and low frequency domains the impedance measured from the model corroding system with the equivalent circuit in Figure 3.7 approaches and intersects the real Z' axis at R_{sol} and $R_{sol} + R_P$, respectively. At the apex of the semicircle, the capacitance can be calculated from the equation,

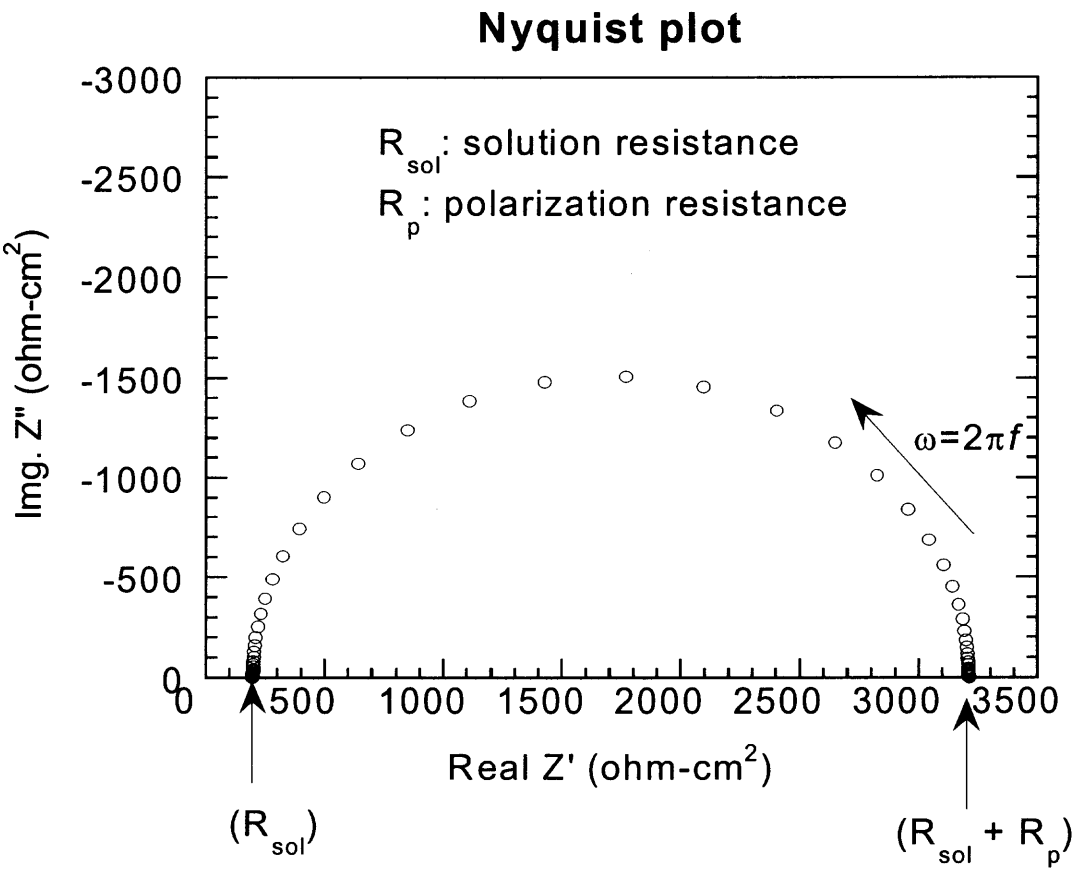

Figure 3.8 Nyquist impedance plot obtained from the EIS measurement consisting of circuit as shown in Figure 3.7.

$C = \frac{1}{\omega R_P}$, driven by differentiating Z'' with respect to Z' and setting it equal to zero.

Unlike the Nyquist plot, in which frequency values are implicit rather than explicit, the Bode plot provides the electrochemical system's frequency-dependent behavior. Figure 3.9 shows a Bode plot for the same impedance data plotted in the Nyquist plot in Figure 3.8. This data presentation involves plots of $\log|Z|$ and phase angle, δ, versus $\log\omega$.

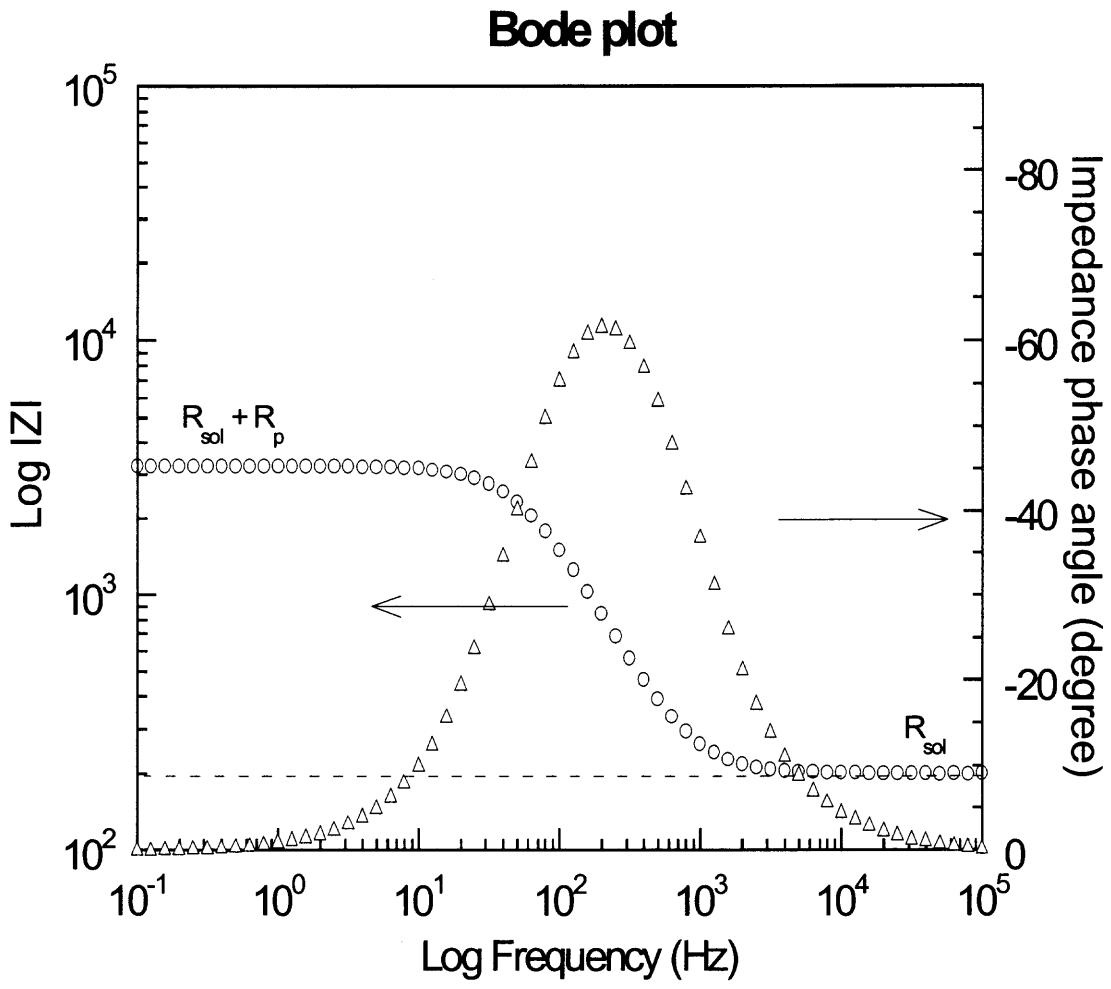

Figure 3.9 Bode plot of electrochemical impedance spectroscopy obtained from measurement on Dummy cell consisting of the circuit shown in Figure 3.7.

From Equation 3.31 $|Z|$ approaches R_{sol} at very high ω and at very low frequencies, $|Z|$ approaches (R_{sol} + R_P) as shown in Figure 3.8. The capacitance is calculated from the analysis of intermediate frequencies, where the magnitude of $|Z|$ is between (R_{sol} + R_P) and R_S. Assuming that R_P is much greater than R_S, Equation (3.35) can be reduced to:

$$|Z|^2 = \frac{R_P^2}{(\omega^2 R_P^2 C^2 + 1)} \tag{3.37}$$

When $|Z|^2 << R_P^2$, the denominator in Equation (3.37) is much greater than one, and therefore, is reduced to $\omega^2 R_P^2 C^2$. Consequently, Equation (3.37) becomes $|Z| = \frac{1}{\omega C}$ or $\log|Z| = -\log\omega - \log C$ and at $\omega = 1$, the capacitance, C, becomes $\frac{1}{|Z|}$.

If the impedance data collected from the EIS measurement are consistent with the physical and chemical aspects of the system under study but do not fit the simplest equivalent circuit model in Figure 3.7, it is necessary to analyze more complex models. A number of equivalent circuits have been developed to model corrosion processes involving diffusion, porous films or coatings, simultaneous electrochemical and chemical reactions, and pitting corrosion.

The rate of an electrochemical reaction can be strongly influenced by diffusion of a reactant towards or a product away from the electrode surface. When diffusion through a surface film or hydrodynamic boundary layer becomes the rate-limiting process in corrosion, a diffusional impedance known as Warburg impedance arises. For this diffusion–controlled process, the current is 45 degree out of phase with the applied potential. With this phase relationship, the real and imaginary components of the impedance vector are equal at all frequencies. The equivalent circuit including the Warburg impedance is shown in Figure 3.10.

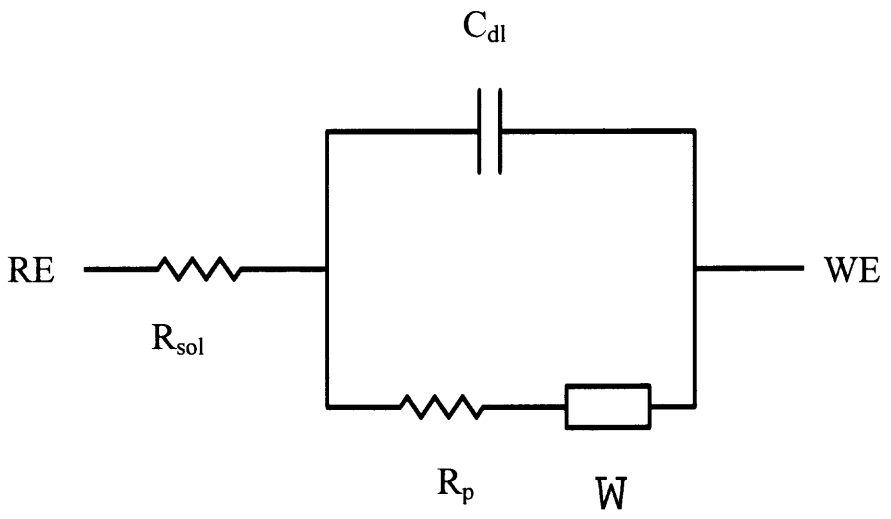

C_{dl}: capacitance of electrical double layer

R_p: polarization resistance of working electrode

R_{sol}: solution resistance

W: Warburg (diffusional) impedance

RE and WE are reference electrode and working electrode, respectively

Figure 3.10 Equivalent circuit for the presence of Warburg (diffusional) impedance.

In real systems, impedance spectra in the Nyquist plot often exhibit some depression below the real axis; causes for this include improper cell design, surface roughness, dispersion of the time constant caused by the reaction having more than one step, and surface porosity [60]. When fitting data with depressed semicircles in Nyquist impedance plot, a constant-phase element (CPE) is widely used. The impedance of a CPE is given by

$$Z = \frac{Z_0}{(j\omega)^n} \tag{3.38}$$

If n=0, then the CPE is a resistor with $R=Z_0$. If n=1, the CPE is a capacitor with $C=1/Z_0$. The physical origins of depressed semicircles are still unclear. Therefore, the meaning of the value of n is also uncertain and if the value of n is 0.8 or greater, the element can be viewed as a capacitor and the capacitance can be calculated from Z_0.

Above the general theory of electrochemical impedance spectroscopy was discussed. To obtain a valid impedance spectrum, the following requirements must be met [61]:

a) Linearity: The response of the system must be a linear function of the perturbation applied. The impedance spectra should be independent of the amplitude of the applied voltage (or current). The simplest method to check linearity is to generate spectra with the excitation amplitude greater and less than that used and to verify that the modulus and phase angle values extracted from the spectra do not change with excitation amplitude at each frequency.

b) Stability: The system must not change during the impedance measurement. In other words, the system returns to its starting state after the perturbation is removed. This is rarely valid for a corroding system, especially when the impedance measurement is conducted during the early stages of the corrosion process. The instability would be most noticeable in the low frequency regime, as the measurement in this range requires longer time than in high frequency. Generating spectra from high to low frequency and repeating from low to high frequency can verify stability. If the spectra are the same, stability is not violated.

c) Causality: The response of the system must be a result only of the applied perturbation.

For any linear system, the phase and amplitude of the impedance are closely linked together. Thus, if we know the phase as a function of frequency we can calculate the amplitude of the impedance from the phase and vice versa by using the Kramers-Kronig (K-K) transform. Therefore, by comparing the results of the K-K transform with the observed phase and impedance, the validity of a measured impedance spectrum can be checked. However, if the impedance measured at the lowest frequency is far from the value that it would have at zero frequency and additional time constants are present in that region, the transform cannot be computed [62].

As briefly mentioned earlier, the impedance spectra are modeled by assuming a circuit made up of resistors, capacitors, and inductors and then fitting that circuit to the spectra to extract values of the circuit elements. The circuits are related to physical phenomena verified with complementary tests to ensure that it is a reasonable representation of the corrosion process. However, like all models, because one fits experimental data, the mechanism is not necessarily isolated as the impedance spectrum for a faradaic electrode reaction at a certain potential usually has several equivalent circuits, differing from each other in structure though essentially equivalent in overall response [63]. However, other analyses can be applied to help isolate the most likely mechanism.

To analyze EIS data, based on equivalent circuit model, some software such as the Kendig's Cirfit [59], the Zellar's Cirfit II and III [64], and the Boukamp's EQUIVCRT [65] have been designed. Nonlinear regression is used to curve fit the equivalent circuit model to the spectra. It is important to note that the number of circuit elements (independent variables) does not exceed the number of data points or even approach the

number of data points. Usually, the simpler the model, the more likely it represents the physical process [66]. The EIS300 software from Gamry Instruments provides a set of analytical tools run from Microsoft Excel and includes a complex non-linear least squares algorithm to fit equivalent circuit models to impedance spectra.

The two types of equivalent circuit models discussed earlier are often used to fit impedance spectra (Figures 3.7 and 3.10). The behavior of passive films formed on bulk niobium and tantalum has been studied using EIS [67]. The impedance measurement on the two metals, which was initially passivated in 0.33 M H_3PO_4 solution, was conducted in 1 M HNO_3. To fit the experimental impedance data Al-Kharafi and Badawy [67] used a theoretical model with the same circuit configuration as shown in Figure 3.7. In other words the rate is due to passive Ta oxide film. In their model, the anodic film was represented by a parallel capacitor/resistor network consisting of the oxide capacitance in parallel with the oxide resistance. Their results showed that the phase angle of impedance spectra obtained from Nb-Nb_2O_5-1M HNO_3 system deviated noticeably from 90° indicating that the Nb passive film did not approach ideal capacitor behavior. Unlike Nb, the tantalum passive oxide film showed a negligible deviation of impedance phase angle and a high stability with various immersion times (15 and 180 minutes), which implied that tantalum oxide passive film (Ta_2O_5) behaved ideally as a capacitor under the given condition.

Kerrec et al. [23] investigated the electrochemical behavior of Ta-TaO_x-electrolyte structure by using impedance spectroscopy in 0.5 M H_2SO_4 solution with the 5 Hz to 1 MHz frequency range. For the EIS data analysis, they used the equivalent circuit model shown in Figure 3.11 (a), where the constant phase element (Q) representing the

oxide capacitance is in parallel with a resistor representing polarization resistance (R_p) and this parallel RC network is in series with a resistor (solution resistance, R_{sol}) and an inductor (L) being attributed to the inductance of cable wires, which was an artifact of the instrument and not originating from the corrosion process. With this theoretical model, the experimental impedance data were fitted by using the LEVM (Levenberg-Marquardt algorithm) [68] complex nonlinear least-square fitting program. According to Kerrec et al. [23] the inductance (L) cannot be neglected when large values of the frequency are used. However, the inductive behavior at high frequencies, showing positive imaginary impedance is always artificial, which means the impedance is not involved in the electrochemical reaction [55]. Therefore, the equivalent model of charge transfer process through electrical double layer and passive Ta oxide film used by Kerrec et al. [23] is that shown in Figure 3.7.

Figure 3.11 (b) shows an equivalent circuit proposed for a corroding metal coated with a porous, non-conductive film [69]. The additional circuit elements to the simple circuit in Figure 3.7 are the coating capacitance (C_c) dependent on its dielectric constant and its thickness and the pore resistance (R_{po}). In their studies on corrosion of an organic coating, Mansfeld [70] and Kendig [58] considered the pore resistance to be due to the formation of ionically conducting paths in the coatings. In addition, R_p is the polarization resistance of the area at the coating/metal interface at which corrosion occurs and C_{dl} is the capacitance due to the electrical double layer at the corresponding interface. This equivalent circuit was employed [71] to fit the EIS data obtained from PVD-TiN coatings on mild steel and AISI 316 substrates in 3 % NaCl solution. In addition, this equivalent

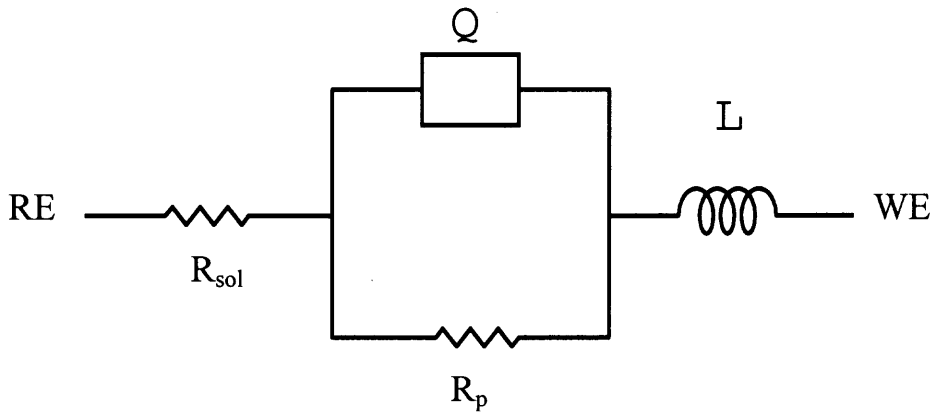

(a)

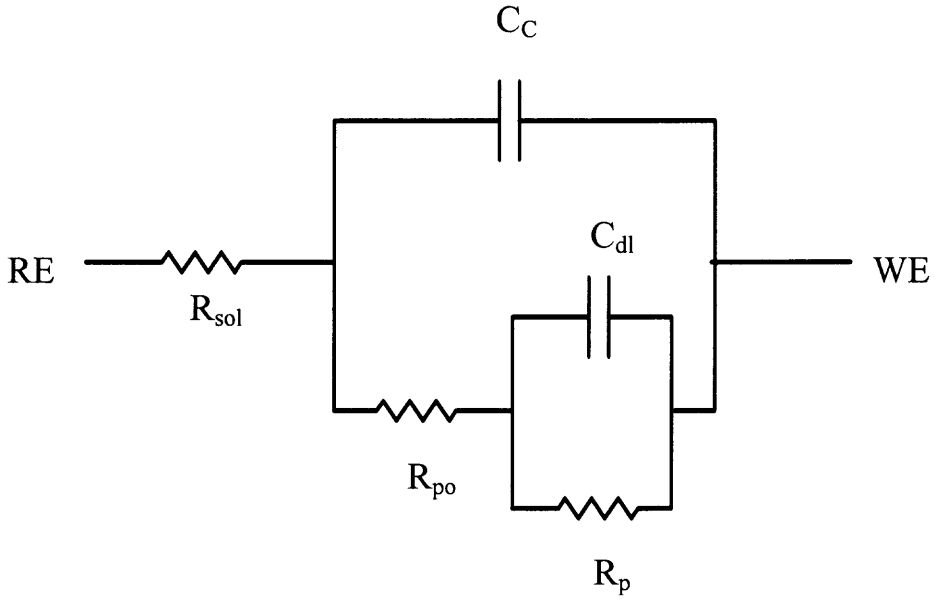

(b)

R_{sol}: uncompensated solution resistance, R_p: polarization resistance, R_{po}: pore resistance, C_dl: double layer capacitance, C_c: coating capacitance, Q: constant phase element, L: inductance, RE: reference electrode, WE: working electrode

Figure 3.11 Equivalent circuit models for analyzing EIS spectra: (a) a simple faradaic electrode process with inductance and (b) a metal coated with a porous, nonconductive film.

circuit, with two time constants was proposed to model the impedance behavior of the chromate film on aluminum alloys two days after exposed to salt fog [72]. In the first 24 hours, Treacy et al. [72] observed that the chromate film on aluminum alloy behaved as a barrier to the aggressive anions and its impedance data were fitted with the model shown in Figure 3.7. After 2 days exposure, however, the chromate-passivated aluminum alloy exhibited a two-time constant response in the impedance data, indicating the onset of chromate coating deterioration. In the next section, the general overview of galvanic corrosion is addressed to obtain an insight for potential galvanic effect between tantalum and steel substrate, when the steel substrate is exposed to electrolyte through open pores.

3.3 Galvanic Corrosion

Galvanic corrosion is a general type of corrosion. In many cases, galvanic corrosion may cause rapid deterioration of the metals but, in other cases, the galvanic corrosion of one metal may induce corrosion protection of an attached metal through cathodic protection by sacrificial anodes. Although galvanic corrosion has been qualitatively described through the extensive investigations, the quantitative evaluation of galvanic corrosion has been difficult until recently because of its highly complex nature [73].

All metals and alloys have a unique corrosion potential (E_{corr}) when immersed in a corrosive electrolyte. For two dissimilar metals or alloys connected electrically in an electrolyte, the one with the more negative corrosion potential has an excess activity of electrons, which are lost to the more positive metal. Therefore a current, called the galvanic current, flows form one (anode) to the other (cathode) [74]. The galvanic series

is a list of corrosion potentials of various alloys and pure metals, which are measured in real or simulated service condition, whereas the electromotive force (emf) series is a list of half-cell potentials proportional to the free energy change of the corresponding reversible half-cell reactions under standard state conditions [74]. The galvanic series does not give any information about the rate of attack but only tendencies for galvanic corrosion between two dissimilar metals or alloys. In addition, changes in electrolyte composition and temperature can cause significant changes in the position of corrosion potential in the galvanic series.

Many factors affecting the electrode properties such as those under categories (a) - (g) as listed in Figure 3.12 can influence on galvanic action between any two different metals or alloys [73]. The intrinsic polarity of a galvanic couple is determined by the reversible electrode potentials of the two-coupled metals, whereas the reactions, metallurgical factors, and surface conditions determine the actual polarity under a given situation because the actual potential (E_{corr}) of a metal in an electrolyte is usually different from its thermodynamic equilibrium value. For example, titanium has a very negative reversible electrode potential in the emf series. However it has a noble position in the galvanic series in many practical environments due to its passivation [73]. Additionally, for alloys with more than two phases, there is significant galvanic action between the different phases. Morris and Smyrl [75] mathematically modeled potential and current distributions on the surface of a metal, consisting of two randomly distributed phases.

The effect of anode and cathode areas on galvanic corrosion depends on whether the galvanic system is under cathodic or anodic control. Galvanic currents in many

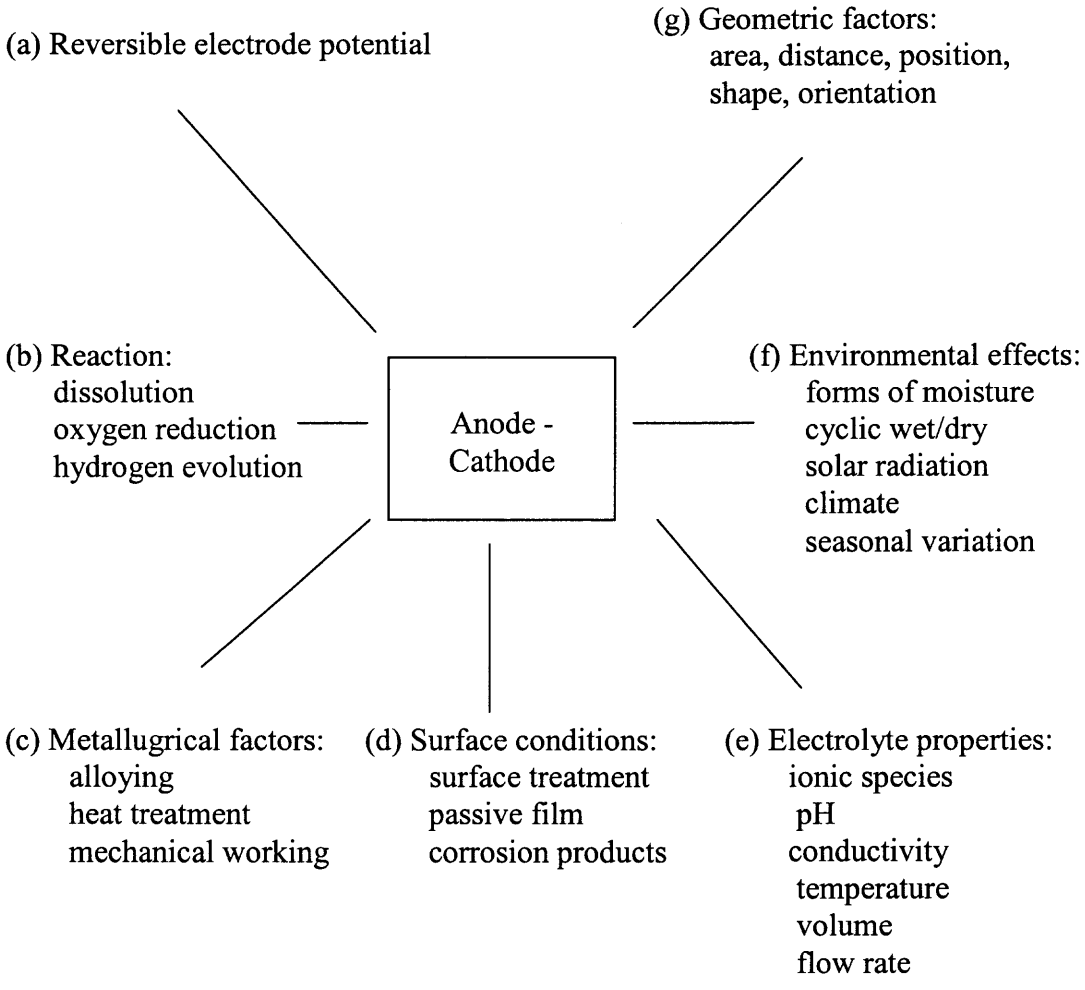

Figure 3.12 Factors affecting galvanic corrosion

situations are proportional to the surface area of the cathode [74]. Larger cathode areas provide more surface for the reduction reaction and the anodic dissolution current increases to compensate.

Corrosion of a cathodic member in a galvanic couple can be influenced by the change of local environment. For instance, aluminum is cathodic to zinc in 3.5 % NaCl solution. However, the corrosion rate of aluminum is greater when coupled to zinc than in the uncoupled condition [76]. The increased corrosion rate of the coupled aluminum is

attributed to the increased alkalinity as it is not stable in a caustic solution. Similar to aluminum, tantalum is attacked by highly alkaline solutions [41]. The solubility of tantalum oxide in 1.0 M KNO_3 solution increases from 6×10^{-6} to 1.06×10^{-5} M between pH 9.0 and 9.8 [77].

In a corroding system, surface interactions include adsorption and film precipitation. The formation of a surface film may significantly change the electrochemical properties of the metal surface, resulting in varying galvanic action [73]. In addition, a corrosion product may serve as a physical barrier between the metal surface and the environment. It may also be directly involved in the electrochemical reactions if it conducts electrical current as either a conductor or a semiconductor. Most metal oxides are conductive materials, mainly as semiconductors [78]. Schultze and Macagno [79] studied the electrochemical behavior of anodic oxide formed on tantalum substrate by using potentiostatic polarization. They reported that thin layers (<15 nm) showed an n-type semiconductor behavior, while the thicker films showed insulating behavior.

Depending on the electronic structure, oxide films exhibit potentials that are generally different from the base metals. In many cases, the electrode potential in the galvanic series is determined by the oxide rather than the metal itself. Wilhelm [80] studied a galvanic series and the cathodic efficiency for oxygen reduction on a number of metal oxides. In his study, the highest current densities for oxygen reduction were observed for n-type oxides (i.e., Fe_2O_3) and metal-like oxides (i.e., Cr_2O_3). Insulator (Al_2O_3) and p-type oxides (i.e., NiO) are inefficient cathodes. The oxides that have a higher cathodic efficiency and exhibit a more noble potential in a galvanic couple result in a greater galvanic corrosion rate of the coupled metal.

Corrosion is a transient process therefore surface conditions change. As exposure time varies, two basic changes occur in a corroding system: (1) the physical structure and chemical composition of the corroding metal surface vary and (2) the composition of the solution, particularly in the vicinity of the electrode surface changes [73]. Other changes as a function of time include surface roughness and area, adsorption of species, formation of passive films, saturation of dissolution products, precipitation of a solid layer, and exhaustion of reactants. In terms of mechanisms, these changes can lead to alteration in the equilibrium potentials, the type of reactions, and the rate-controlling process [73]. The corrosion potential is greatly influenced by the nature and extent of these changes and the rate of galvanic corrosion may vary with time as a result of changes in polarity and in potential difference between metals of a galvanic couple.

As mentioned earlier, galvanic corrosion is influenced by the surface condition of the metals, which in turn, is determined by environmental conditions. Table 3.1 shows the corrosion potentials of a number of metals in four different electrolytes with similar ionic strength. The normal polarity of some galvanic couples under conditions may reverse as function of time. The degree of passivity, the nature of the redox couples in the solution, and the stability of the system determine the polarity and its variation with time [73]. For zinc and steel, the change in potential of the zinc electrode reflects the reversal of polarity, as the potential of the steel remains relatively unchanged with time in hot water [81]. Polarity reversal of the aluminum-steel couple has been found to occur in natural environments, where aluminum is used as a sacrificial anode for cathodic protection of steel. However, aluminum is usually passivated in most natural environments. The potential of aluminum is dependent on the degree of passivation,

Table 3.1 Corrosion potential (mV_{SCE}) of Metals after 24-h immersion if four different solutions, compared with the emf series[a] [73].

Emf	0.1 M HCl	0.1 M NaCl	0.1 M Na_2SO_4	0.1 M NaOH
Ag +799	Ag +48	Ag -60	Ag +147	Ag -64
Cu -324	Ni -135	Ni -142	Cu -43	S. Steel -96
Pb -126	Cu -139	Zr -150	Cr -45	Ni -171
Sn -138	Ta -213	Cu -189	Ti -66	Cu -231
Ni -257	Ti -221	Cr -270	Ni -70	Cr -303
In -338	Zr -297	Ti -272	Ta -157	Fe -389
Fe -447	Cr -347	Ta -295	Zr -218	Ta -500
	S. Steel -473	S. Steel -320	S. Steel -348	Zn -555
Cr -744	Pb -487	Pb -565	Sn -421	Ti -591
Ta -750	Sn -497	Sn -565	Al -505	In -600
Zn -762	Fe -557	In -646	Pb -545	Zr -631
Zr -1553	In -680	Fe -710	In -651	Pb -757
Ti -1630	Al -731	Al -712	Fe -720	Mg -809
Al -1660	Zn -989	Zn -1019	Zn -1049	Sn -1096
Mg -2370	Mg -1894	Mg -1548	Mg -1588	Al -1351

[a] Sample surface area about 1 cm^2; polished with 600-grade emery paper; solution open at air at room temperature

which is sensitive to ions in solution. Gabe and Hassan [82] found that carbonate and bicarbonate ions promoted passivity of aluminum of the aluminum-steel couple and hence, produced more noble potential values, while chloride ions gave rise to the opposite effect.

As discussed above, metallic coatings on a metal substrate generally undergo galvanic corrosion and many factors affecting the electrode properties can influence galvanic action between two dissimilar metals. In addition the galvanic corrosion rate is significantly affected by the area ratio of cathode to anode where actual potential changes with exposure time. The purpose of conducting galvanic corrosion tests in this study is not to evaluate the effect of such factors listed in Figure 3.12, but to assist the interpretation of corrosion behavior of the tantalum coating. The experimental conditions for galvanic corrosion tests with tantalum and steel were equivalent to those for the electrochemical corrosion studies of the tantalum coatings. Specifically, the tests were conducted in 0.5 M H_2SO_4 (pH 0.6) solution at room temperature ($\pm$ 2 ^{o}C). The systems were being purged with N_2 gas to remove dissolved oxygen and isolate the system from air. The volume of the solution per exposed area of specimen should be greater than the minimum of 0.40 mL/mm^2 required for the standard laboratory immersion corrosion test [83] to avoid any appreciable change in the solution corrosivity during the test. For Ta_2O_5, pH has little effect on the solubility over the range of 0 – 2. Furthermore, because the system was completely mixed, bulk transport limited processes could be neglected. Therefore, the factor affecting galvanic action can be limited to for the most part the oxidizing agent, in this case the hydrogen ion. As tantalum tends to be cathodic in coupling with steel substrate, hydrogen evolution occurs on tantalum and hydrogen

embrittlement discussed in the next section can be a serious problem in highly corrosive environments.

3.4 Hydrogen Embrittlement

Hydrogen that enters the metallic lattice and permeates through the metal can cause embrittlement and failure of structures in service environments. It is generally observed that if large amounts of hydrogen are absorbed, there may be a loss in ductility and if large amounts of hydrogen are collected in localized areas, internal blisters may occur [84, 85]. Even small amounts of dissolved hydrogen may react with the microstructure of alloys to cause failures at applied stress far below the yield strength [86]. All these phenomena are referred to as hydrogen embrittlement.

Hydrogen can be absorbed by metal during aqueous corrosion or cathodic charging. When corrosion occurs at low-pH, reduced hydrogen may diffuse into the metal. Environments containing hydrogen sulfide are especially dangerous for alloys and metals. When tantalum interacts with hydrogen gas, a considerable amount of hydrogen can diffuse into tantalum even at relatively low temperatures. The maximum limit of solubility of hydrogen was reported to be 50 at. % [87]. Although tantalum corrodes at very low rates, it may take up large amounts of hydrogen resulting in embrittlement [88] and for coatings failure. The following section illustrates how electrochemical techniques are applied to measure porosity of metallic coating on metal substrate.

3.5 Evaluation of Porosity of Metal Coatings by Electrochemical Techniques

The main purpose of a metal coating is to protect the substrate from corrosion. Ideally the coating would exhibit the same corrosion behavior as its bulk form. However, it is not feasible to achieve such a perfect coating in practice. As mentioned in the Introduction, the presence of defects such as open pores in a metal coating is a critical problem in obtaining a protective coating, especially when the metal coating becomes cathodic to the metal substrate such as in the case of tantalum coated steel. In addition such defects lead to a rapid localized galvanic attack at the coating/substrate interface and pitting corrosion of the substrate occurs. Therefore, the evaluation of porosity is critical in assessing its performance.

Pores classified as "through pores" or open pores as referred to here, are ones that extend from the base metal to the surface of the coating, while "masked pores" are ones that do not provide free access through the coating to the base metal [14]. This implies that "through pores" can cause more severe corrosion than "masked pores". Also, pores have been categorized into gross pores that are visible to unaided eyes, fine pores that are identified by a microscope, and submicroscopic pores (intrinsic pores) that are owing to imperfections in the crystal lattice. According to Notter and Gabe [14], porosity of electroplated coatings is generally associated with pores that are randomly distributed over the coating surface, and defects existing on the substrate before plating increase porosity. Porosity can be reduced by increasing coating thickness [17].

In general porosity tests involve pore detection tests, where the number of pores are evaluated indicating the pore distribution, and porosity index tests measuring the total exposure area of substrate through pores which is expressed as the area ratio of the

exposed substrate surface to the total coating surface [14]. The objective of pore detection tests is to assess porosity particularly for open pores. Several pore detection methods, including chemical, electrochemical, and physical, have been developed. Porosity index tests include chemical and electrochemical porosity index measurements. Most chemical porosity index methods are based on measuring the dissolution rate of the substrate metal through pores.

Electrochemical porosity index measurements, including corrosion potential, corrosion rate, and polarization resistance measurements, were developed from electrochemical theory on corrosion and are based on the mixed potential theory of the galvanically coupled metals. The corrosion potential measurement was systematically investigated as a porosity test by Morrisey [89] who evaluated the porosity of gold coatings on copper and observed that the corrosion potential was related to the logarithm of the exposed area of substrate through open pores. He formularized the relation between the corrosion potential and the exposure area by using model polarization diagrams:

$$E_{corr} = C - \frac{\beta_a \cdot \beta_c}{\beta_a + \beta_c} \log Af^A \qquad (2.39)$$

where E_{corr} is corrosion potential, C is constant and Af^A is the area fraction of exposed substrate, such that $Af^A+Af^C=1$ (Af^C is the area fraction of the coating material). β_a and β_c are the anodic Tafel slope of the substrate and the cathodic Tafel slope of the coating material, respectively. This equation was modified as follows by Notter and Gabe [14] who studied the porosity of thin tin coatings on steel in a 0.5 M ammonium thiocyanate electrolyte:

$$E_{corr} = C' - \frac{\beta_a^A \cdot \beta_c^C}{\beta_a^A + \beta_c^C} \log \frac{A^A}{A^C} \tag{2.40}$$

where C´ is a constant and A^A and A^C are the anodic (substrate) and cathodic (coating) fraction, respectively. According to the equation, the corrosion potential is determined by the ratio of the area of coating to that of exposed substrate.

From the electrochemical point of view, the pores were considered to play the role of resistors connected in parallel because of the electrolyte resistance through the coating pores [14]; this is called pore resistance. In addition there is a polarization resistance caused by the electrochemical reaction at the substrate electrolyte interface (via through pores). Therefore, the total polarization resistance obtained during the polarization resistance measurement is expressed as follows:

$$\frac{dV}{di} = R + \frac{dE}{di} \tag{2.41}$$

where *dE* is the potential displacement of the substrate with respect to the applied current density (*di*), R is the normalized pore resistance with respect to the surface area of the coating, and *dV* is the displacement of the potential due to the polarization resistance of the substrate through pores and the pore resistance. From their review on the electrochemical measurements for porosity, Notter and Gabe [14] outline experimental conditions required for measuring polarization resistance in pores, which include:

a) The coating passes a negligible current compared to that passed through the pores.

b) There must be no local attack of the coating.

c) Polarization of the base metal is insensitive to changes in current density. In other words, the term, $\frac{dE}{di}$ from the above equation should be small compared to R.

d) The electrolyte present in the pores is not affected by the passage of current; the pore resistance should be stable.

Morrisey [89] derived the following equation for expressing the relationship between the polarization resistance and the exposed area of the substrate from his study on gold-coated copper:

$$\log\left(\frac{\Delta I}{\Delta E}\right) = K + \frac{\beta_a \cdot \beta_c}{\beta_a + \beta_c} \log Af^A \tag{2.42}$$

where K is a constant, Af^A is the fraction of exposed anode (substrate) area, and β_a and β_c are the anodic Tafel slope of the substrate and the cathodic Tafel slope of the coating material, respectively.

The above equation was later modified by Notter and Gabe [90] as follows:

$$\log\left(\frac{\Delta I}{\Delta E}\right) = K' + \frac{\beta_a}{\beta_a + \beta_c} \log\frac{A^A}{A} + \frac{\beta_c}{\beta_a + \beta_c} \log\frac{A^C}{A} \tag{2.43}$$

where K′ is a constant, A^A and A^C are the anodic (substrate) and cathodic (coating) fraction, respectively ($A^A + A^C = A$ where A is defined as total exposed area). As A^C is close to A in most cases, this equation can be simplified to:

$$\log\left(\frac{\Delta I}{\Delta E}\right) = K' + \frac{\beta_a}{\beta_a + \beta_c} \log\frac{A^A}{A} \tag{2.44}$$

Methods for evaluating porosity on metal coatings have been reviewed. The porosity is evaluated by assessing the number of pores per unit area of coating surface and the area of substrate exposed by these pores. Therefore, as part of this study on corrosion behavior of tantalum coatings, the porosity will be evaluated electrochemcally.

3.6 Summary

Overall, the following summarizes the important points reviewed in this chapter:

1. The high corrosion resistance and inertness of tantalum is mainly attributed to a thin, impervious, protective oxide film (mostly tantalum pentoxide). Therefore, the corrosion resistance of tantalum is characterized by the passivation of tantalum and hence the stability of tantalum oxide in corrosive media from an electrochemical viewpoint.
2. In galvanic corrosion of two dissimilar metals, the corrosion potential of each metal is the critical factor in determining which metal becomes cathodic or anodic and is dependent on the electrode surface properties. Additionally, the ratio of cathodic to anodic area is proportionally related to the galvanic current. The polarity of galvanic couples may reverse as a function of time.
3. The corrosion potential of tantalum in a corrosive medium is greater than that of stainless steel and iron because of the formation of tantalum oxide. Therefore, tantalum has tendency to become cathodic when galvanically coupled with steel.
4. When tantalum becomes cathodic in a galvanic couple, reduced hydrogen can diffuse in and be absorbed by tantalum. As a result of hydrogen absorption, tantalum undergoes hydrogen embrittlement.
5. The presence of defects such as open pores in a metal coating is a critical problem in obtaining a protective coating, especially when the metal coating becomes cathodic to the metal substrate. Such defects lead to a rapid localized galvanic attack at the coating/substrate interface and pitting corrosion of the substrate

occurs. Generally the porosity of a metallic coating is inversely proportional to coating thickness.

6. The application of electrochemical techniques to the porosity evaluation of metallic coatings has been developed.
7. Electrochemical impedance spectroscopy has been widely used as a powerful tool to evaluate the corrosion process. The impedance spectra are modeled by assuming a circuit made up of resistors, capacitors, and inductors and fitting that circuit to the spectra to extract values of the circuit components. The values can be related to physical phenomena by verifying the circuit model through complementary measurements to ensure that it is a reasonable representation of the corrosion process.

In short, tantalum is very corrosion resistant to most environments because of spontaneous growth of the extremely stable oxide. However, when tantalum is galvanically coupled to other metals, it becomes cathodic and undergoes hydrogen embrittlement through hydrogen reduction. Metallic coatings on metal substrates in the presence of defects such as cracks and open pores experience localized and accelerated corrosion, especially when a metallic coating tends to be cathodic against the metal substrate in galvanic coupling. In addition, the porosity of such open pores is reduced as the coating thickness increases. Therefore, it is necessary to obtain an optimum coating thickness in which the metallic coating shows similar properties to its bulk form with respect to corrosion. Once a viable coating thickness is defined, the corrosion behavior of Ta can be investigated and specifically, corrosion rates and mechanisms can be evaluated.

CHAPTER 4

OBJECTIVES AND OVERALL APPROACH

The overall objective of this study is to understand the corrosion behavior of tantalum coatings. Therefore, supporting objectives include

- Evaluating the porosity of the Ta coating as a function of thickness. Using electrochemical techniques the optimum thickness resulting in a viable (defect free) coating will be determined. The presence of open pores results in localized corrosion of the steel substrate, where the overall rate then is a function of exposed metal areas. For a defect free coating, the corrosion behavior including corrosion rate, polarization behavior, and impedance behavior would be similar to the bulk tantalum as a function of immersion time.
- Assessing the corrosion behavior of α- and β-phase Ta and steel substrate as a function of time to obtain information on corrosion properties of the individual specimen.
- Modeling the corrosion process to obtain a physically meaningful equivalent circuit model for fitting the EIS impedance data. Thus, the corrosion mechanism will be evaluated.
- Evaluating the impact of substrate surface roughness on corrosion resistance of coating as surface modification (i.e., polishing) is not feasible in full-scale processes.
- Comparing the performance of Ta versus Cr coatings produced in full-scale operation; and,

- Determining structural properties of the passive Ta oxide film to assist in better understanding its unique properties that provide an effective corrosion barrier.

In the corrosion process, the passivation of tantalum results in tantalum oxide, which plays an important role as a barrier. One hypothesis in this research is that tantalum pentoxide (Ta_2O_5) is expected to be the most dominant oxide present during passivation. The additional hypotheses include

- The presence of open pores decreases corrosion resistance of Ta coatings.
- Corrosion behavior of defect-free Ta coating is equivalent to that of bulk Ta.
- Ta is comparable to Cr with respect to corrosion performance in full-scale processes for the coatings.

To achieve the objectives of this research and test the hypotheses, Ta coated steel is analyzed before and after the electrochemical corrosion tests by means of:

- X-ray diffraction (XRD) for crystallographic analysis
- Field emission-scanning electron microscopy with energy dispersive x-ray spectroscopy for morphological and elemental analysis and defect-identification
- Atomic force microscopy for roughness assessment

The corrosion experiments are isolated from dissolved oxygen by purging with N_2 gas, and sulfuric acid (0.5 M) was used as a supporting electrolyte. Therefore, the hydrogen ion is the only oxidizing agent. To reduce resistance from external film mass transfer, the systems are completely mixed.

The electrochemical experiments to evaluate corrosion involve potentiodynamic polarization for the assessment of corrosion rate and anodic polarization behavior, and the electrochemical impedance spectroscopy for evaluating polarization resistance as a

function of immersion time and modeling the corrosion process by fitting impedance data with equivalent circuits. The mass loss method for assessing corrosion rate is widely used especially for long-term studies but is not useful for localized corrosion with metallic coatings. In addition x-ray absorption fine structure spectroscopy (XAFS) is used to compare the local structure of anodic oxides formed on Ta foil to that of thermally formed Ta oxide. In the next chapter, a detailed description of the methods is provided and followed by the four studies conducted to address the objective and hypotheses of this research.

CHAPTER 5

METHODS

5.1 Materials

In this study, AISI 4340 steel, pure tantalum foil (99.9 % purity from Goodfellow), and tantalum coatings on steel substrates were investigated. In addition, in Chapter 8 Cr coatings are studied as a comparison for the performance of the Ta ones. AISI 4340 steel is used as it has the closest composition to gun-barrel steel [92]. The chemical composition of AISI 4340 is compared with gun-barrel steel (Table 5.1). Before mechanical polishing, electrolyte cleaning was applied to remove heavy machining oils from steel substrate. AISI 4340 steel and a pure tantalum disk were polished using silicon carbide paper of 320 grit followed by 600 grit and down to 0.05 μm of polycrystalline diamond suspension cleaned with methyl alcohol, and rinsed with deionized water in an ultrasonic cleaner. For thermal and anodic oxidation a pure tantalum foil was polished using 0.05 μm alumina suspension. The overall procedure of steel substrate preparation is listed in Table 5.2. The mechanical polishing procedure for steel substrate (AISI 4340 steel) before tantalum coating is based on technical information provided by Buehler Company (Table 5.3). The reason of single type of abrasive such as polycrystalline diamond suspension instead of using silicon carbide paper for rough polishing and alumina abrasive for fine polishing is to reduce the number of contamination sources by polishing abrasive particles. Prior to sputtering, specimens were examined by FE-SEM/EDX and AFM. The tested coating samples consisted of α- and β-phase Ta coatings with various coating thicknesses, which were obtained from Dr. Sosnowski's

Table 5.1 Typical chemical composition of AISI 4340 steel [93] and gun-barrel steel [2]

Element	AISI 4340 (wt. %)	Gun steel (wt. %)	Element	AISI 4340 (wt. %)	Gun steel (wt. %)
Aluminum	0.021	-	Nickel	1.99	3.17
Antimony	0.0042	-	Niobium	0.22	-
Arsenic	0.017	-	Phosphorus	0.015	0.006
Bismuth	0.0004	-	Selenium	0.004	-
Carbon	0.392	0.37	Silicon	0.223	0.02
Cerium	0.0013	-	Silver	0.0004	-
Chromium	0.69	0.85	Sulfur	0.015	0.01
Cobalt	0.032	-	Tantalum	0.020	-
Copper	0.042	-	Tellurium	0.0006	-
Lanthanum	0.0004	-	Tin	0.011	-
Lead	0.000025	-	Titanium	0.020	-
Manganese	0.66	0.47	Tungsten	0.017	-
Molybdenum	0.19	0.65	Vanadium	0.011	0.10
Neodymium	0.0003		Zirconium	0.009	
Balanced Fe				95.405	94.354

Table 5.2 Procedure of steel substrate preparation prior to Ta coating

Step	Method	Condition	Purpose
1	Electrolyte cleaning	Current density - 100 mA/cm^2 Temperature – 77 °C Polarity – Anodic Duration – 5 minutes	To remove heavy machining oil
2	Mechanical polishing	Refer to Table 4.3	
3	Ultrasonic cleaning	Duration – 5 minutes Solution – methanol or acetone	For final degreasing
4	Rinsing	Deionized water	-
5	Drying with N_2 gas	Blowing wet specimen	-
6	Ar sputtering etching	Ar pressure – 230 mTorr Voltage – 400 ~ 500 V Current – 100 $\mu A/cm^2$	To remove adsorbed gas from the steel surface

Table 5.3 Mechanical polishing for steel substrate

Abrasive (diamond suspension) Size	Load (N)	Base speed*	Time (minutes)
45 μm	25	50	Until plane
9 μm	25	45	10
3 μm	25	45	10
1 μm	25	45	10
0.05 μm	25	45	5

*: Setting-speed by MINIMET 1000 Grinder/Polisher (Buehler Ltd.)

group (NJIT). The α-Ta, β-Ta, and Cr coatings were produced in full-scale cylindrical processes by Benet laboratory. Additionally, details of sample preparation and coating conditions are presented in Chapters 6 through 9.

5.2 X-ray Diffraction

Before an electrochemical test, x-ray diffraction (XRD) patterns of each specimen are measured using a Philips X'Pert-MPD XRD system with PC-APD software. X-rays are generated with a Cu $K\alpha$ x-ray source (λ=1.54056Å) operating at 45 kV and 40 mA. The data are collected over the 2θ range of 10° to 120°. XRD was conducted to evaluate the phase and texture. In addition, one variable that can influence corrosion is the crystal plane, which is exposed to corrosive environment [48]. Mauvais et al. [94] from their corrosion study on single crystals of nickel observed that the anodic polarization behavior was dependent on crystal orientation, indicating that the passive film structure and/or thickness is sensitive to the arrangement of atoms at the surface. Therefore, the crystallography of specimens was examined by XRD.

5.3 Electrochemical Tests

The electrochemical tests used in this research include EIS, potentiodynamic polarization, galvanic corrosion tests, and anodic oxidation. The electrochemical tests were conducted by using a Gamry PC4/300 system consisting of potentiostat, galvanostat, zero-resistance ammeter, and frequency response analyzer with an electrochemical cell (Figure 5.1). The

reference and counter electrodes used are a saturated calomel electrode (SCE) and a platinum electrode, respectively. The exposed circular area of the working electrode is 1 cm^2. The internal calibration for the potentiostat was conducted using a high precision 100 ohm resistor prior to each EIS test, and the stability of the EIS system was tested by using a dummy cell consisting of a resistor in series with a parallel connection of a resistor and a capacitor.

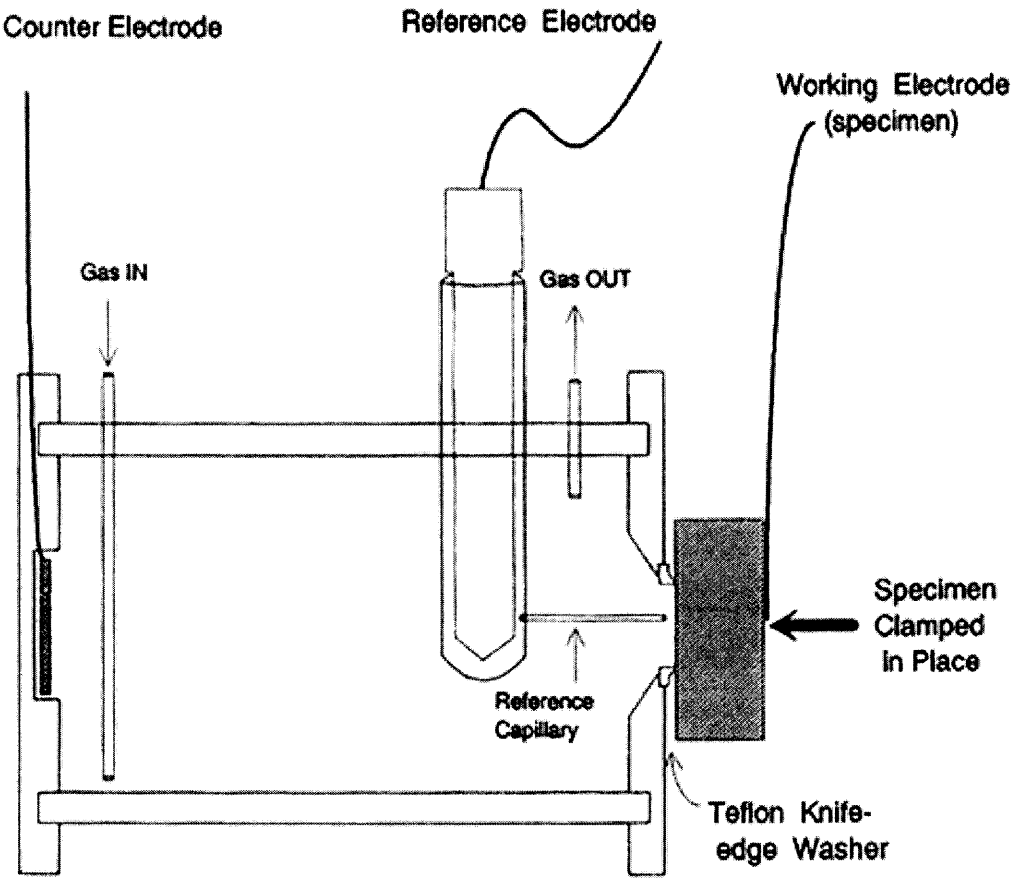

Figure 5.1 Flat electrochemical cell

The test electrolyte is 0.5 M H_2SO_4 solution, which is prepared by diluting 10 N H_2SO_4 stock solution (LabChem, Inc.) with deionized water (Type I reagent water). Before the corrosion test, the electrolyte was purged with N_2 gas at a flow rate of 1 L/min for at least 30 minutes to remove dissolved oxygen from the solution. The purge continued throughout corrosion test to isolate the test system from air and to maintain complete mixing. All electrochemical tests were carried out at room temperature. The volume of test solution for the exposed surface area (100 mm^2) is 250 mL, which meets the minimum of 0.40 mL/mm^2 required for standard laboratory immersion corrosion test (ASTM G31-72) [83] to avoid any appreciable change in its corrosivity during the test.

The electrochemical corrosion tests are conducted to evaluate the corrosion performance of each specimen as function of immersion time within 4 to 5 days. The duration of immersion time is continued to assess stability of the coating. During the immersion period, potentiodynamic polarization and electrochemical impedance spectroscopy are used to examine the anodic polarization behavior and polarization resistance, which represents corrosion resistance.

In addition to the corrosion test, an anodic oxidation experiment using the galvanostatic technique detailed in Chapter 9 is conducted on tantalum foil to obtain a thicker tantalum oxide than the passive film formed on tantalum under a free corroding system. The purpose of this experiment is to evaluate the local structure of the passive film formed on different phases by extended x-ray absorption fine structure (EXAFS) using total electron yield (TEY) mode. The passive film from free corrosion is too thin to be examined by EXAFS-TEY. Therefore, it was necessary to produce a thick anodic oxide passive film.

5.3.1 Potentiodynamic Polarization

Measurement of the polarization behavior is a powerful method for determining the corrosion behavior of a metal over a wide range of oxidizing conditions in a single test solution. A polarization curve is a plot of the current from the working electrode surface versus the electrochemical potential applied to the electrode. The corresponding current provides a measure of the rate of the overall process at each potential. There are in general two techniques to obtain the polarization curve: potentiostatic and potentiodynamic polarization methods. The potentiostatic polarization technique measures the polarization behavior of a working electrode by applying a series of discrete potential steps (for example, increasing or decreasing potential (50 mV) vs. open circuit potential in increments of 5 minutes) and monitoring the current response at each applied potential. Potentiostatic polarization is employed for two basic reasons: (1) the potentiodynamic polarization technique is not available, and (2) the current is measured as a function of time after each potential step to examine true steady-state [91]. However, with the widely available modern instrumentation, most anodic polarization curves are now obtained potentiodynamically [74]. In potentiodynamic polarization, the potential is changed continuously with a constant scan rate (for example, 10 mV/min) and the response current is measured. From this study, characterization of a metal specimen by its current-potential relationship provides important information such as: the ability of the material to spontaneously passivate in a particular medium; the potential region over which the specimen remains passive; and the corrosion rate. In anodic polarization, the working electrode (metal specimen) potential is scanned continuously in the positive direction versus open circuit potential and hence acts as an anode in such a way that

metal corrodes or forms a metal oxide, the passive film. This method permits the easy automation of curves and real time plots of the experimental data. Because of the ability to automate data collection, potentiodynamic polarization techniques have become more popular than potentiostatic for producing polarization curves [91].

There are two experimental parameters in potentiodynamic polarization measurement; scan rate and scan range with respect to the applied potential. In general a scan rate is selected to minimize testing time but slow enough to obtain a polarization curve at near steady-state conditions. The magnitude of the current measured at each potential is a function of the scan rate [91]. ASTM Standard G5-94 [95] specifies a scan rate of 10 mV/min for potentiodynamic polarization measurements conducted on stainless steel (Type 430) in 0.5 M H_2SO_4 solution. Thompson and Payer [91] state that 10 mV/min is an appropriate starting point in selecting an optimum scan rate by performing potentiodynamic polarization measurement with several scan rates. Therefore, a scan rate of 10 mV/min was applied here for AISI 4340 steel in 0.5 M H_2SO_4 to obtain a polarization curve at near steady-state conditions. From a study on passive behavior of tantalum, Wilhelmsen [46] observed that the measured current at an applied potential (1.0 V) becomes approximately constant after a stabilization period of about 20 hours. Based on this observation and preliminary studies, a scan rate of 10 mV/min was found to be appropriate tantalum samples.

The fundamental procedure for experimentally evaluating corrosion current density is by Tafel extrapolation. In general, a potential scan greater than ± 100 mV versus corrosion potential is required to reach potentials at which the anodic and cathodic Tafel behavior dominates and to determine whether a linear section of at least one decade

of current is present [48]. To obtain anodic and cathodic polarization curves with a single scan, the starting potential in the scan is a negative (-200 to -400 mV) [91]; however, a larger starting potential can alter the steady-state condition established at the corrosion potential and influence the measurement of the corrosion current density. Additionally, the ASTM Standard G5-94 [95] recommends a potential range of 0 to 1.6 V versus corrosion potential for anodic polarization curves. Therefore, a range of -200 to 1500 mV was selected in this study.

Potentiodynamic polarization measurements were carried out with a scan rate of 5 mV/sec from -200 mV to 1.5 V versus open circuit potential (OCP) at the initial and final immersion times. The OCP obtained from this measurement is plotted versus immersion time. These experiments were conducted to study the passive behavior of tantalum and tantalum coatings including the assessment on corrosion current density as a function of time.

5.3.2 Electrochemical Impedance Spectroscopy

AC impedance measurements are performed at open circuit potential with the amplitude of perturbation 10 mV (r.m.s.) in the frequency range between 10 mHz and 100 kHz. The EIS spectra were collected during immersion. The evolution of impedance spectra is presented as a Bode plot from which the magnitude of polarization resistance and characteristic corrosion behavior are seen. Using these data, mechanistic modeling was accomplished in tandem with complementary studies that include microscopic and spectroscopic analyses.

5.3.3 Galvanic Corrosion Test

To assist the evaluation on the corrosion behavior of tantalum coatings, the galvanic corrosion test was conducted. Experimental conditions such as electrolyte, temperature, and exposure time was equivalent to those for the electrochemical corrosion tests. The test specimens are bulk tantalum foil (α-phase, Goodfellow) and steel substrate (AISI 4340). The volume of the solution per exposed area of specimen should be greater than the minimum of 0.40 mL/mm^2 required for standard laboratory immersion corrosion test (ASTM G31-72) [83] to avoid any appreciable change in solution corrosivity during the test. In the galvanic tests detailed in Chapter 6, area ratios of cathode (tantalum) to anode (steel) (i.e. 0.82, 3.4, and 11.33) were evaluated. In order to measure the galvanic corrosion current produced by the coupling of bare metals (tantalum foil and steel substrate), a zero-resistance ammeter equipped in Gamry PC4/300 system was utilized.

5.3.4 Anodic Oxidation

The anodic oxidation experiments are conducted to produce a thicker tantalum oxide than that formed in a free corroding system. The local structure of this oxide was studied by EXAFS. In anodic experiments, galvanostatic current (i=0.7 mA/cm^2) is applied to fine-polished tantalum foil and beta tantalum coating to form the anodic oxide in 0.5 M H_2SO_4 at room temperature [23]. Kerrec et al. [23] found that anodic oxides of tantalum appear to be produced with a faradaic yield of 100 % in 0.5 M H_2SO_4 solution at 25 °C. This was verified in their results where the thickness of the anodic oxide deduced from the capacitance measured in electrochemical impedance spectroscopy was in good agreement with that calculated based on Faraday's law. In the calculation they considered that the

anodic oxide was composed of Ta_2O_5 based on angle-resolved x-ray photoelectron spectroscopy (AR-XPS) measurements indicating that thicker layers (> approx. 15 nm) of the oxide were 95 mol % Ta_2O_5.

5.4 Scanning Electron Microscopy (SEM) and Energy Dispersive X-ray Spectroscopy (EDX)

The morphological information of the tantalum coating specimens before and after an electrochemical tests is obtained by using SEM. Field-emission scanning electron microscopy (LEO 1530 FE-SEM) was employed to obtain better quality of morphological information on uncorroded and corroded samples because the resolution of FE-SEM (LEO 1530) is approximately five times greater than that of ESEM (ElectroScan 2020). The resolution of FE-SEM (LEO 1530) is 1 nm at the acceleration voltage of 20 kV under high vacuum mode. In addition the corrosion product formed by dissolution of the steel substrate through coating pores is evaluated using EDX (OXFORD INCA EDX system) in cooperation with FE-SEM. The quantitative EDX analysis was carried out using OXFORD INCA EDX analysis software.

5.5 Extended X-ray Absorption Fine Structure Spectroscopy (EXAFS)

EXAFS provides the most reliable means for obtaining the local structural environment in situ. EXAFS does not require information on long-range order and is equally applicable to amorphous materials in its ability to probe the environment of an element in

the sample by selecting and tuning to the edge energy [96]. The use of a synchrotron source produces a high flux of x-rays needed for data acquisition [97].

The simplest EXAFS experiments may be conducted in transmission mode as shown in Figure 5.2. The sample is mounted on the stage and the incident and transmitted x-rays are detected with an ion chamber as the energy is varied over the absorption edge. The spectra include the near edge and fine structure over the edge; both providing information on the coordination environment with respect to the types of atoms surrounding the probe species, bond distances, and the oxidation state. EXAFS refers to the sinusoidal variation of the x-ray absorption coefficient as a function of photon energy occurring beyond each absorption edge of an element.

In the classical limit, the fine structure above the absorption edge can be viewed as interference between the photoelectron wave ejected from the target atom and waves scattered from its neighboring atoms. The Fourier transform of these spectral features

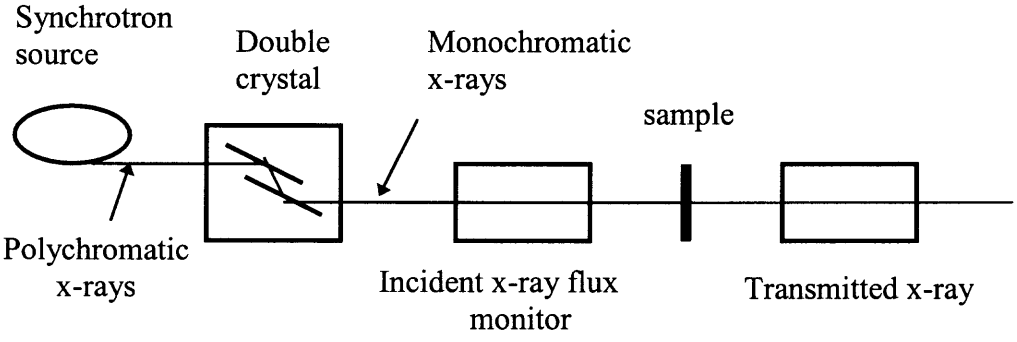

Figure 5.2 Schematic XAFS experiment in transmission mode

yields a qualitative representation of the radial distribution function. Structural parameters are determined by least-squares analysis providing the distance, number, type of neighboring atoms, and an estimate of the disorder affecting the interatomic distance [96].

CHAPTER 6

CORROSION BEHAVIOR OF MAGNETRON SPUTTERED α- AND β-Ta COATINGS ON AISI 4340 STEEL AS A FUNCTION OF COATING THICKNESS

6.1 Introduction

Tantalum coatings produced by sputtering, one form of physical vapor deposition (PVD) have been investigated as a replacement for Cr coatings to protect gun-bore from erosion and corrosion [6, 98]. Bulk Ta (α phase) shows excellent physical and chemical properties such as a high melting point (2996 °C), good ductility, and excellent corrosion resistance in aggressive environments. However, under varying deposition conditions, α-Ta (body-centered cubic structure), β-Ta (tetragonal structure), or a mixture of both phases have been observed [99, 100]. Because of the brittle nature of β-Ta, the α-phase is preferred in protecting gun-bore against erosion.

A metal coating deposited without impurities or defects should exhibit corrosion behavior comparable to that of the bulk metal. However, in practice it is generally not feasible to achieve such coatings, especially thin ones. Consequently, the potential presence of defects (i.e., pinhole, open pores) in coatings may result in severe localized corrosion due to the galvanic action when the coating is cathodic with respect to the substrate [14]. This galvanic effect, localized at open pores, is increased by an unfavorable surface ratio, when the cathodic area is much greater than the anodic area. One method to minimize the presence of defects penetrating the coating from the surface to the substrate is to increase the coating thickness. Coating porosity is in general

inversely proportional to coating thickness; this reduction has been observed to be for the most part irrespective of the coating process [14]. Therefore, it is critical to obtain a minimum thickness for defect-free coatings, which have corrosion performance similar to that of the bulk metal.

Electrochemical techniques including DC corrosion and electrochemical impedance spectroscopy (EIS) have been employed to evaluate the corrosion behavior and porosity of metallic and ceramic coatings [15, 90, 101-104]. For example, Elsener et al. [101] evaluated porosity of PVD and chemical vapor deposition (CVD) TiN coated steel at the free corroding potential. Assuming that the coating is electrochemically inert at the open circuit potential the authors estimated the porosity from polarization resistance and reported that the PVD coatings were 25 times less porous than the CVD ones. However, both coatings on mild steel showed severe localized corrosion at film defects. In addition, Liu et al. [104] compared the degree of delamination of TiN and CrN coatings as a function of time and found delamination was greater for the TiN coating than the CrN one. Their study demonstrated that as immersion time increased, galvanic corrosion localized at open pores where the steel substrate dissolution occurred causing delamination of the adjacent coating.

In this part of study, α-Ta and β-Ta coatings with thicknesses of 5 μm, 10 μm, 50 μm, and 100 μm deposited on AISI 4340 steel using DC magnetron sputtering were investigated with potentiodynamic polarization and EIS. Morphological evaluation of the surface and cross-sections after corrosion tests was conducted using scanning electron microscopy (SEM). In addition, galvanic corrosion behavior of Ta and steel substrate was studied by varying the area ratio of Ta to the steel substrate.

6.2 Experimental Methods

6.2.1 Preparation of Substrates and Ta Deposition

The substrates machined from AISI 4340 steel had the form of square coupons, 12.6 mm × 12.6 mm, 6 mm thick. Before loading, the substrate was electrochemically cleaned and mechanically polished with diamond suspensions of decreasing particle size, down to 0.05 μm. The polished steel substrates were then ultrasonically cleaned in acetone and methanol. The surface roughness of the polished steel substrates measured by AFM was 12.4 ± 1.9 nm (r.m.s.).

Tantalum was deposited using a DC magnetron sputtering system [105]. The base pressure in the process chamber was 1.1×10^{-5} Pa. A tantalum target (99.95 %) with a 50 mm diameter was mounted 50 mm below the substrate holder. Prior to sputtering, the substrates were baked in the chamber at 200 °C and sputter-etched with Ar (99.995 %) for 10 min. The α-Ta coatings of 5, 10, 50, and 100 μm and β-Ta coatings of 5 and 10 μm were produced within 20% variation of the desired thickness; production of thicker coatings of the β-phase were not possible due to its metastability. A deposition rate of 1.2 nm/sec with the source current of 0.5 A and a target voltage of 330 V was used for the 5 and 10 μm coatings. For thicker coatings, the initial deposition rate was 1.2 nm/sec, up to 3 μm thickness, and then the source current was increased to 1 A with a target voltage of 375 V, resulting in a deposition rate of 2.4 nm/sec. In producing the α-phase, the steel substrate was heated to approximately 420 °C during the sputtering process. Polished Ta foils (99.9 %) and polished steel substrates (AISI 4340) were used as references for electrochemical tests.

6.2.2 Coating Characterization

The crystallographic phase identification and microscopic roughness of the deposited coatings were investigated by x-ray diffraction (XRD) and atomic force microscopy (AFM), respectively. Before and after the corrosion tests, the surface and corrosion features of coated samples were examined using an electron microscope with a field emission electron source and capable of qualitative elemental analysis by energy dispersive X-ray spectroscopy (EDX). The corrosion products could therefore be qualitatively assessed at the pinhole defects.

6.2.3 Electrochemical Tests

The test solution for electrochemical investigations was a deaerated 0.5 M H_2SO_4, which was prepared by diluting the standardized 10 N H_2SO_4 (ACS reagent grade) with deionized (DI) water and purging with N_2 gas (99.999% purity) at a rate of 1.0 L/min for 1 h before an electrochemical test. The solution was also continuously purged with the N_2 gas at a rate of 0.5 L/min during the experiment. All studies were conducted at room temperature (22 ± 3 ^{o}C).

6.2.3.1 Galvanic Current Measurement Tantalum is an electrochemically active metal as its thermodynamic nobility lies below zinc. However, once passivated, its stable oxide film places tantalum above gold in practical nobility [12]. Therefore, Ta has the tendency to be cathodic to steel when exposed to an electrolyte through open pores. To assess the galvanic behavior of the Ta and steel (AISI 4340) couple, galvanic currents with cathodic (Ta foil) to anodic (AISI 4340 steel) area ratios of 0.82, 3.4 and 11.33 were

measured using a zero resistance ammeter (ZRA) during a total immersion time of 24 hours.

6.2.3.2 Potentiodynamic Polarization and EIS Potentiodynamic polarization and EIS measurements were carried out using a Gamry PC4/300 computerized system for collecting and analyzing electrochemical data. A Flat cell (Princeton Applied Research) was used with a three-electrode configuration including a saturated calomel electrode (SCE) and platinum gauze as reference and auxiliary electrodes, respectively. All electrochemical corrosion tests were carried out with an exposure area of 1 cm^2.

Potentiodynamic polarization was measured 1 h after immersion with a scan rate of 10 mV/min from –0.2 to +1.5 V versus the open circuit potential (OCP). EIS data were collected at OCP with a sinusoidal voltage perturbation of 10 mV (r.m.s.) over the frequency range of 10 mHz to 100 kHz with 7 to 10 points per decade; these spectra were obtained over 0.5, 1, 4, 8, 24, 48, 72, and 96 h of exposure time. The data were analyzed using complex nonlinear least squares fitting (CNLS) LEVM algorithm [68] in the Gamry Echem Analyst software.

6.3 Results and Discussions

6.3.1 Phase and Microstructure of Ta Coatings

The thin α-Ta coatings of 5 and 10 μm show (110) preferred orientation (Figure 6.1), while thicker α-Ta coatings show (222) preferred orientation; presence of β-phase was not observed in these coatings. For the β-Ta coatings three peaks (Figure 6.1), referred to

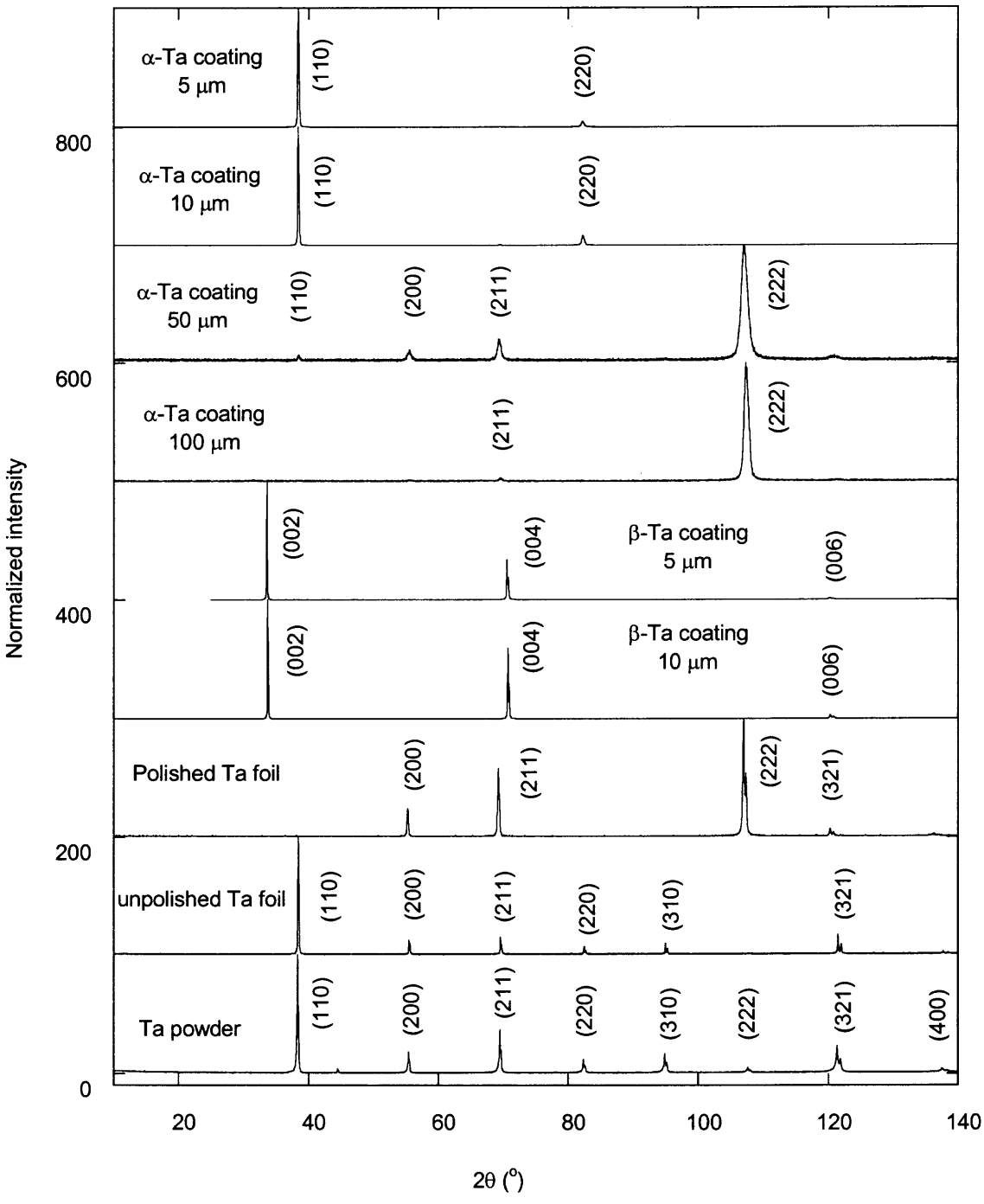

Figure 6.1 X-ray diffraction patterns of α- and β-Ta coatings, Ta foil (polished and unpolished) and Ta powder.

as (002), (004), and (006) are observed with no trace of the α-phase. In general, β-Ta films exhibit (002) texture [106]. Bulk Ta foil shows a slightly preferred (110) orientation with a very similar pattern to that of Ta powder. Interestingly, mechanical polishing changed the foil orientation to the (222) reflection.

Thin α-Ta coatings were relatively smooth with the roughness (Rrms) of 5 μm and 10 μm coatings measured at 5.6 nm and 9.8 nm, respectively (Figure 6.2a, b). The roughness clearly increased with coating thickness and was significantly greater for 50 μm and 100 μm α-Ta coatings (Figure 6.2c, d). Thin β-Ta coatings had similar roughness to that of thin α-Ta coatings but exhibited somewhat finer surface features (Figure 6.2e, f). As discussed earlier, 50 and 100 μm Ta coatings were deposited at a higher sputtering rate, which appears to increase the surface roughness as compared to the slower process. Nevertheless, the coating surfaces are smooth as the roughness factor (f_r = real surface area/geometric surface area) over a scan area of 100 × 100 μm^2 was less than 1.02. SEM images of the coatings surface morphology showed uniform coverage of the steel substrate area without any cracks. However, the presence of some defects such as pinhole and droplet-like clusters that are commonly found in PVD processes [104, 107, 108] is observed on the coated surface regardless of thickness and phase (α and β). Pinholes (Figure 6.3c) are observed only on the surface of thin coatings, while the droplet shape defects are seen on both thin (Figure 6.3a, b, d) and thick coatings (Figure 6.3e and f). The formation of pinholes is relatively rare, compared to droplet-like defects. The distribution of droplet-like defects appears to be random and their density is reduced as the coating thickness increases. Defects in the form of open pores or voids extending from the coating surface to the substrate are of most concern as they provide a channel

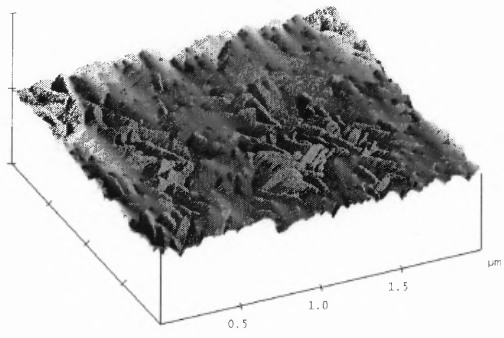

(a) α-Ta 5 μm, R_{rms} = 5.6 nm

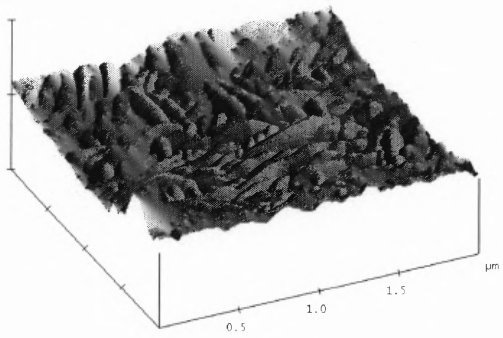

(b) α-Ta 10 μm, R_{rms} = 9.8 nm

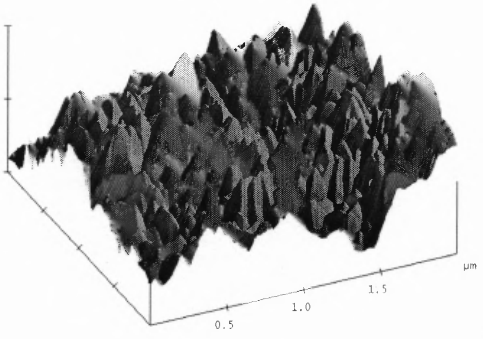

(c) α-Ta 50 μm, R_{rms} = 29.3 nm

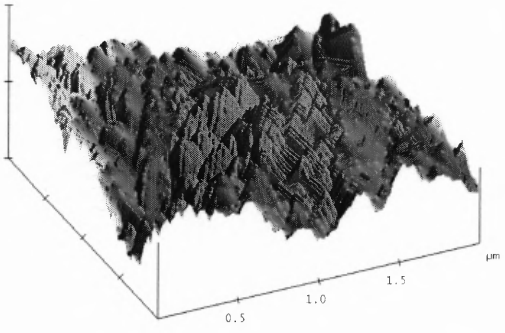

(d) α-Ta 100 μm, R_{rms} = 22.1 nm

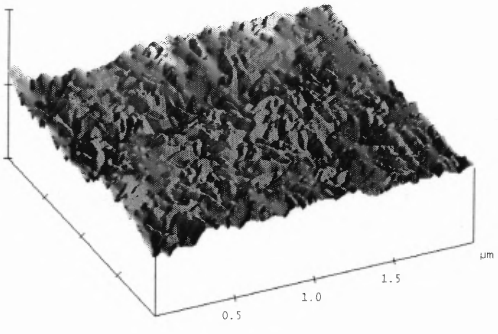

(e) β-Ta 5 μm, R_{rms} = 7.2 nm

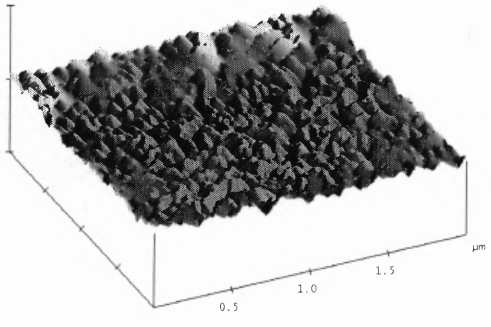

(f) β-Ta 10 μm, R_{rms} = 6.2 nm

Figure 6.2 Surface plot of Ta coatings obtained by AFM.

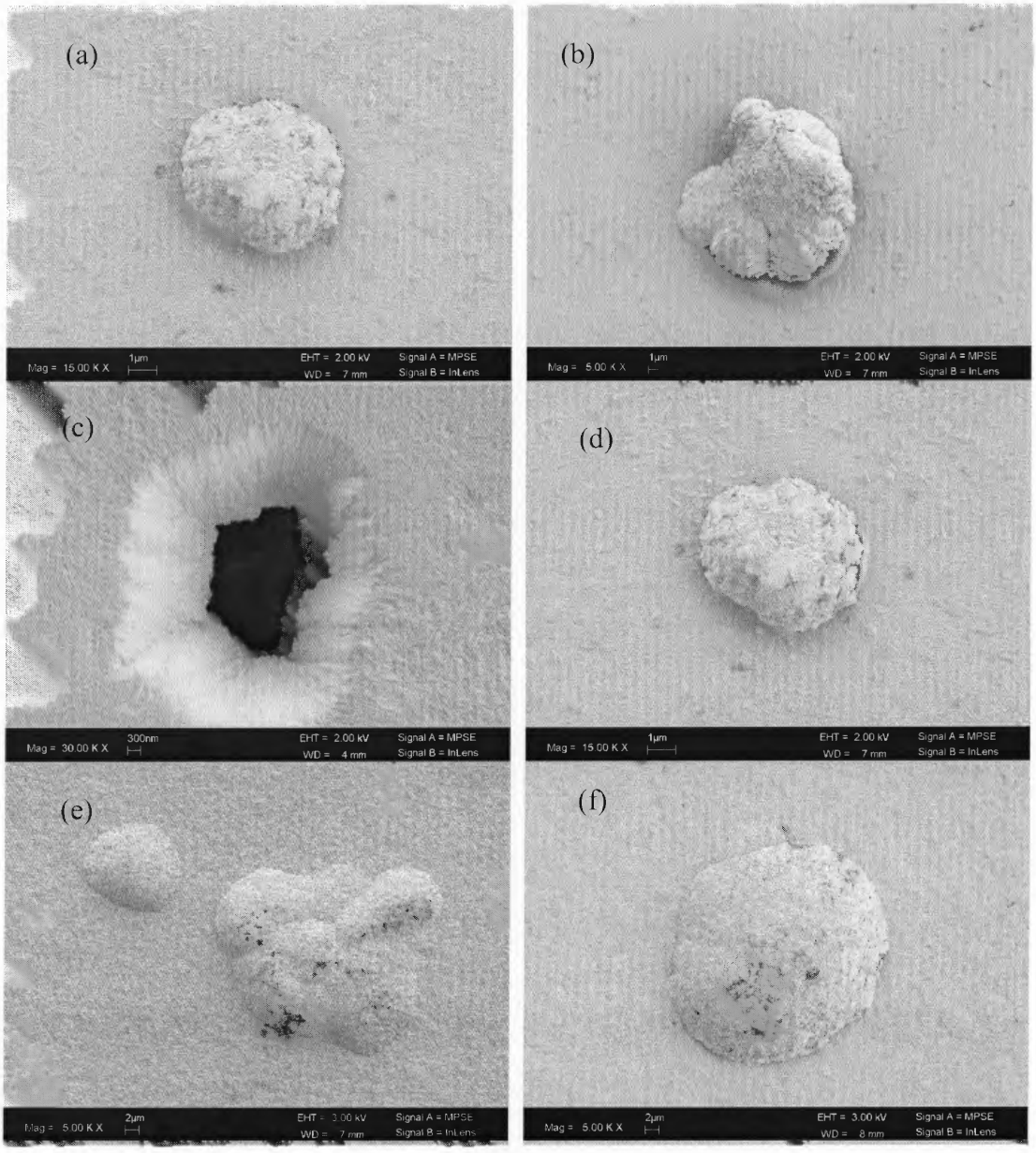

Figure 6.3 SEM images showing defects observed on (a) 5 µm thick α-Ta coating; (b) 10 µm thick α-Ta coating; (c) 5 µm thick β-Ta coating; (d) 10 µm thick β-Ta coating; (e) 50 µm thick α-Ta coating; (f) 100 µm thick α-Ta coating.

for electrolyte penetration to the steel and hence, initiate localized corrosion, enhanced by the galvanic effect.

6.3.2 Galvanic Corrosion

To evaluate the galvanic corrosion effect between Ta and steel (AISI 4340) substrate, the evolution of the galvanic current was measured as a function of the surface area ratio of cathode (Ta foil) to anode (AISI 4340 steel) (0.82:1 to 11.33:1). During the measurement, the galvanic current density (i_g) was quite constant and no reversal in polarity was observed, indicating the surface conditions for the both electrodes appear to be stable. The current density was observed to increase as the cathode to anode areas ratio increased (Figure 6.4). Nevertheless, the magnitude of the current density was much smaller than the corrosion current density of the steel substrate (ca. 0.558 mA/cm^2). However, the galvanic potential measured in Ta/steel coupling was close to the open circuit potential of the steel (-454 mV vs. SCE). These results demonstrate that the galvanic current density is not equivalent to the steel dissolution rate when the anode is polarized slightly from its corrosion potential [109]. In Ta/steel coupling, the contribution of cathodic reduction of H^+ to the dissolution of steel appears to be insignificant.

When the steel substrate is exposed to electrolyte through open pores in Ta coating, localized corrosion is accelerated due to the galvanic action. To understand better the relationship between porosity, open pores, and coating viability, measurements of potentiodynamic polarization were conducted.

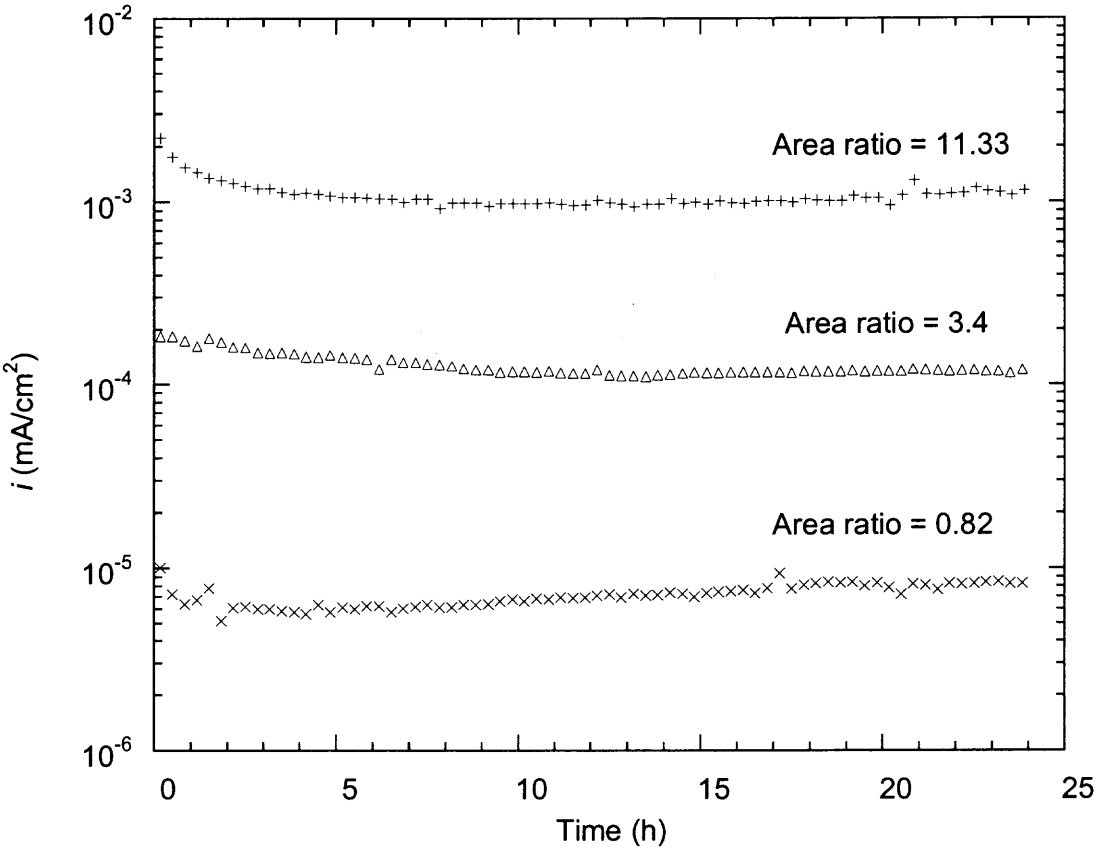

Figure 6.4 Evolution of galvanic current density measured from different ratios of cathodic (Ta foil) to anodic (AISI 4340 steel) areas in deaerated 0.5 M H_2SO_4 with N_2 at room temperature during 24 h.

6.3.3 Potentiodynamic Polarization

The polarization curves of the Ta coatings of different thickness, Ta foil, and AISI 4340 steel were obtained 1 h after immersion (Figure 6.5). The corrosion and passivation current densities of α- and β-Ta coatings decreased with increasing coating thickness. For 50 and 100 μm, the corrosion resistance is comparable with that of a polished Ta foil. The latter exhibits almost the same behavior to that of the unpolished Ta foil, except for

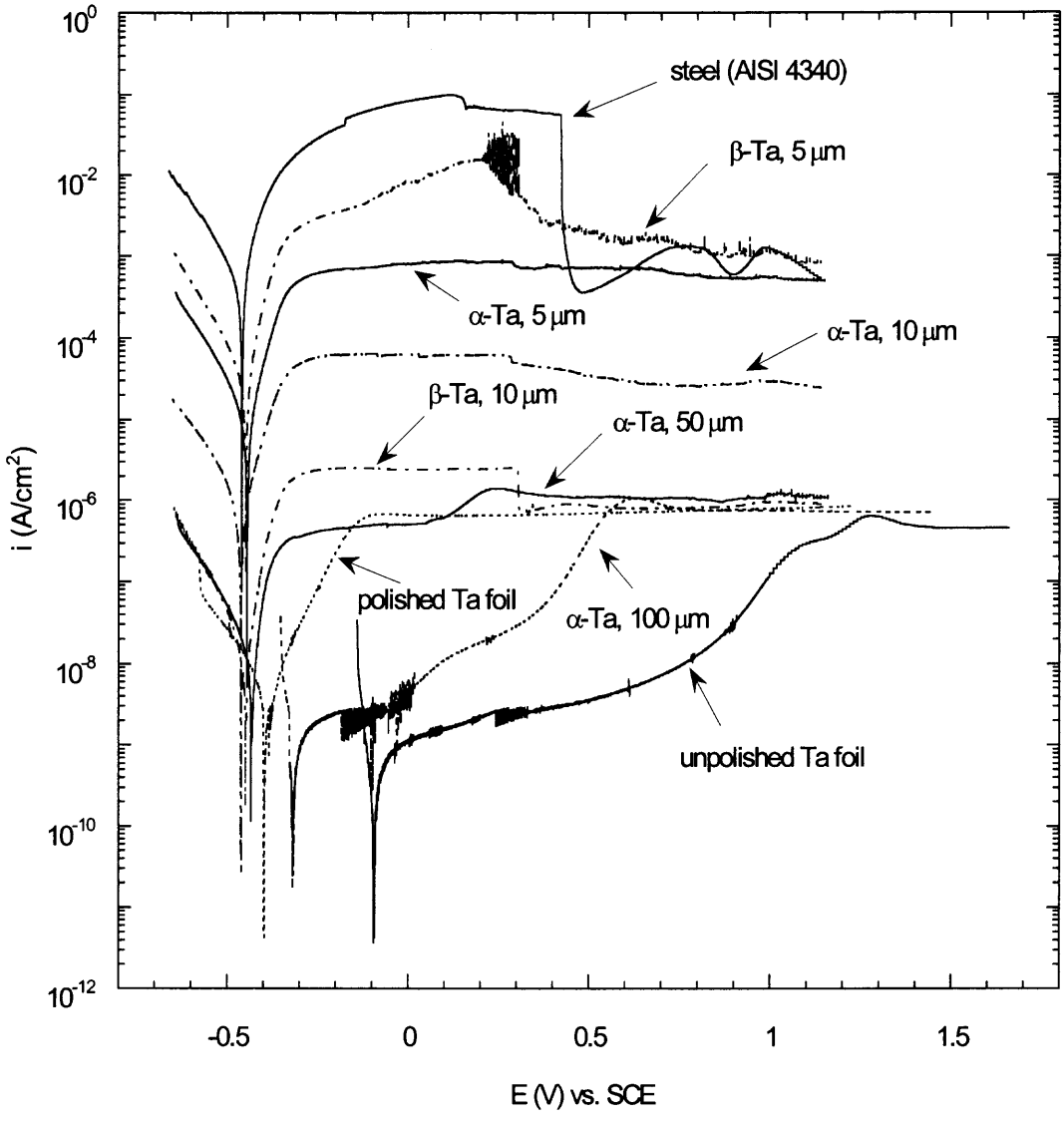

Figure 6.5 Anodic polarization curves of α- and β-Ta coatings with different thicknesses, Ta foil, and steel substrate (AISI 4340) in deaerated 0.5 M H_2SO_4 purged with N_2 at room temperature.

the open circuit potential difference (Table 6.1). Moreover, the polarization resistance of the 100 μm coating falls between that of the unpolished and polished Ta foil; therefore, this coating produced in our PVD system behaves like that of bulk Ta foil with respect to corrosion performance.

The polarization measurements on α-Ta foils showed that the corrosion potential of unpolished Ta foil is greater than that of polished Ta foil and that the resistance of unpolished Ta foil at the corrosion potential is approximately one order of magnitude greater than that of polished Ta foil (Table 6.1). The resistance of the polished foil is still very high. The difference in the resistances may be due to the difference in thickness or composition of the native oxide film present on the surface of the foils [45].

SEM images of defects in a thin Ta coating on steel, after the potentiodynamic polarization test, are shown in Figure 6.6. The results of EDX measurements indicate the presence of Fe, O and S elements related to the corrosion products. These results reveal that corrosion of the steel substrate covered with thin α- and β-Ta coatings occurs through defects. There was no evidence of steel substrate dissolution for the 50 and 100 μm coatings. Therefore, defects such as pinholes and porosity are major factors and the overall corrosion process appears to be dominated by locally active substrate dissolution through open pores. Porosity evaluation is thus critical for the quality control of the coatings.

As the polarization resistance of Ta foil at open circuit potential is five to six orders of magnitude greater than that of AISI 4340 steel (Table 6.1), the Ta coating is chemically inert and hence, the polarization resistance of Ta coatings measured at open circuit potential is represented by the resistance of the steel substrate exposed to the

Table 6.1 Electrochemical characteristics of Ta coatings, Ta foil and steel (AISI 4340) substrate.

	α-Ta coating/steel (AISI 4340)				β-Ta/steel (AISI 4340)		Ta foil		Steel (AISI 4340)
Thickness (μm)	5	10	50	100	5	10	bulk	polished	polished
E_{corr} (mV vs. SCE)	-444	-461	-433	-318	-445	-450	-58 ± 159	-388 ± 44	-454 ± 9
Rp (Ω cm^2)	1.60×10^3	2.27×10^4	1.09×10^6	1.67×10^7	4.58×10^2	7.54×10^5	3.14×10^7 ± 1.98×10^6	3.14×10^6 ± 1.29×10^6	23.8 ± 8.1
b_a (mV/decade)									47.7 ± 2.3

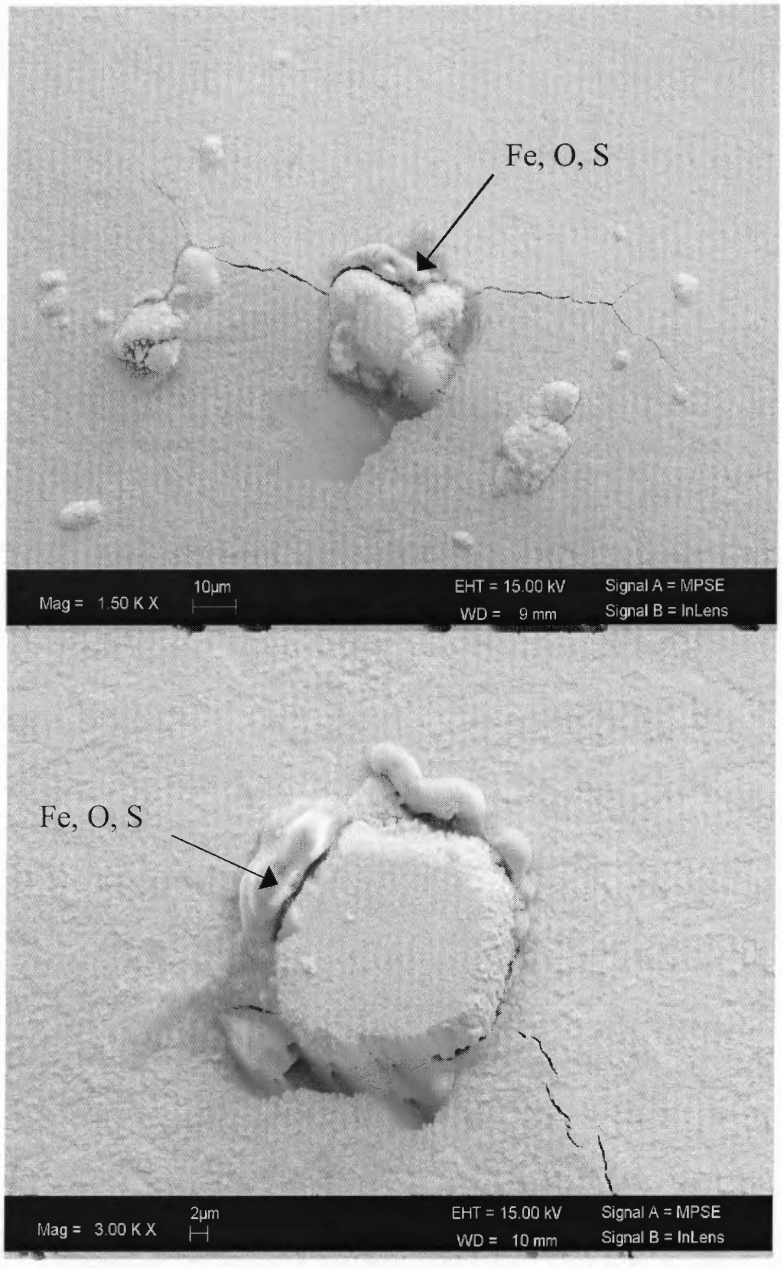

Figure 6.6 Typical SEM images of thin Ta coating (α-phase and 5 µm thickness) showing the corrosion of the steel substrate through defects and propagation of cracks initiated from defects after potentiodynamic polarization measurements in deaerated 0.5 M H_2SO_4 purged with N_2 at room temperature. Arrows indicate location of the elements detected with EDX.

electrolyte through open pores. In addition, the corrosion potential of Ta coatings less than 100 μm thick is slightly shifted from that of the bare steel substrate and far below its passivation potential, indicating the steel substrate was actively dissolving. In this case, the total coating porosity index P, which represents the area ratio of total pores to total exposed surface is estimated using the following equation [101]:

$$P = \left(\frac{R_{p,bs}}{R_p} \right) \times 10^{-|\Delta Ecorr|/b_a} \tag{6.1}$$

where R_p and $R_{p,bs}$ are the polarization resistances of the Ta coated steel and bare steel substrate, respectively, ΔE_{corr} is the difference in the corrosion potential between the Ta coating and the bare steel substrate, and b_a is the anodic Tafel slope of the bare steel substrate. Increasing coating thickness reduced porosity (Table 6.2), which is attributed to a void masking effect, i.e. covering the voids (closing pores) by the depositing material. Such mechanism is effective in coatings with thickness significantly greater than the void size. The effect appears to be more pronounced for thin β-Ta coatings than for α-Ta coatings (in 5 – 10 μm range), probably due to the finer grain structure of β-Ta (Figure 6.2). Using Equation (6.1) without a calibration procedure may not provide a highly accurate porosity for submicroscopic pores because the equation is dependent on the corrosion resistance of the coating. For example, even polished Ta foil with a R_p of 3.14×10^6 ohm exhibits a porosity, 3.1×10^{-5} %, which is greater than that for the 100 μm coating, 2.0×10^{-7} %; however, both are insignificant.

The corrosion resistance of a coating in general varies with increasing immersion time due to potential delamination of the coating and/or blocking of pores by corrosion

Table 6.2 The porosity of α- and β-Ta coated steel (AISI 4340) as a function of thickness evaluated from polarization resistance 1 h after immersion.

	α-Ta coating/steel (AISI 4340)				β-Ta/steel (AISI 4340)	
Thickness (μm)	5	10	50	100	5	10
P (%)*	0.94 ± 0.12	0.073 ± 0.047	0.00079 ± 0.00013	$2.0 \times 10^{-7} \pm 8.8 \times 10^{-8}$	3.8 ± 0.76	0.0026 ± 0.00068

E_{corr}, R_{ps} and b_a of AISI 4340 steel for porosity estimation were –454 mV (vs. SCE), 23.8 Ω cm^2, and 47.7 mV/decade, respectively. The error in P is estimated based on the variation in E_{corr}, R_{ps}, and b_a of AISI 4340 steel shown in Table 1.

product [104, 110, 111]. Therefore, the stability of the Ta coating as a function of immersion time was investigated using EIS.

6.3.4 Corrosion Behavior as a Function of Immersion Time Evaluated by EIS

The impedance spectra, which were collected over 4 days at the corrosion potential, are compared to that of the Ta foil and AISI 4340 steel (Figure 6.7). The impedance at the low frequency plateau in the Bode plot is indicative of the sum of the polarization and the electrolyte resistance; the latter of which is seen at the high frequency plateau. The impedance of Ta foil appears to be at least five orders of magnitude greater than that of AISI 4340 steel, and is in good agreement with that observed in potentiodynamic polarization measurements. Tantalum shows consistent and stable impedance behavior as a function of exposure time. This stability and large impedance may be attributed to the very stable tantalum oxide film. In addition, the maximum phase angle for Ta foil over all immersion times is close to $\pi/2$, representing a good capacitive response [110] throughout the 4 day exposure. This capacitive behavior has been reported to be due to the passive film as well as the electrical double layer [23].

The impedance spectra of α-Ta coatings, 50 μm and 100 μm thick, reveal that there was no significant change over 4 days of exposure (Figure 6.8). The phase angle response is very similar to that of Ta foil. In addition only one relaxation time constant in the EIS spectra is observed, as in the case of Ta foil. Therefore, with respect to corrosion performance, the α-Ta coating with a thickness greater than or equal to 50 μm appears to behave in a similar manner to that of Ta foil over long exposure times.

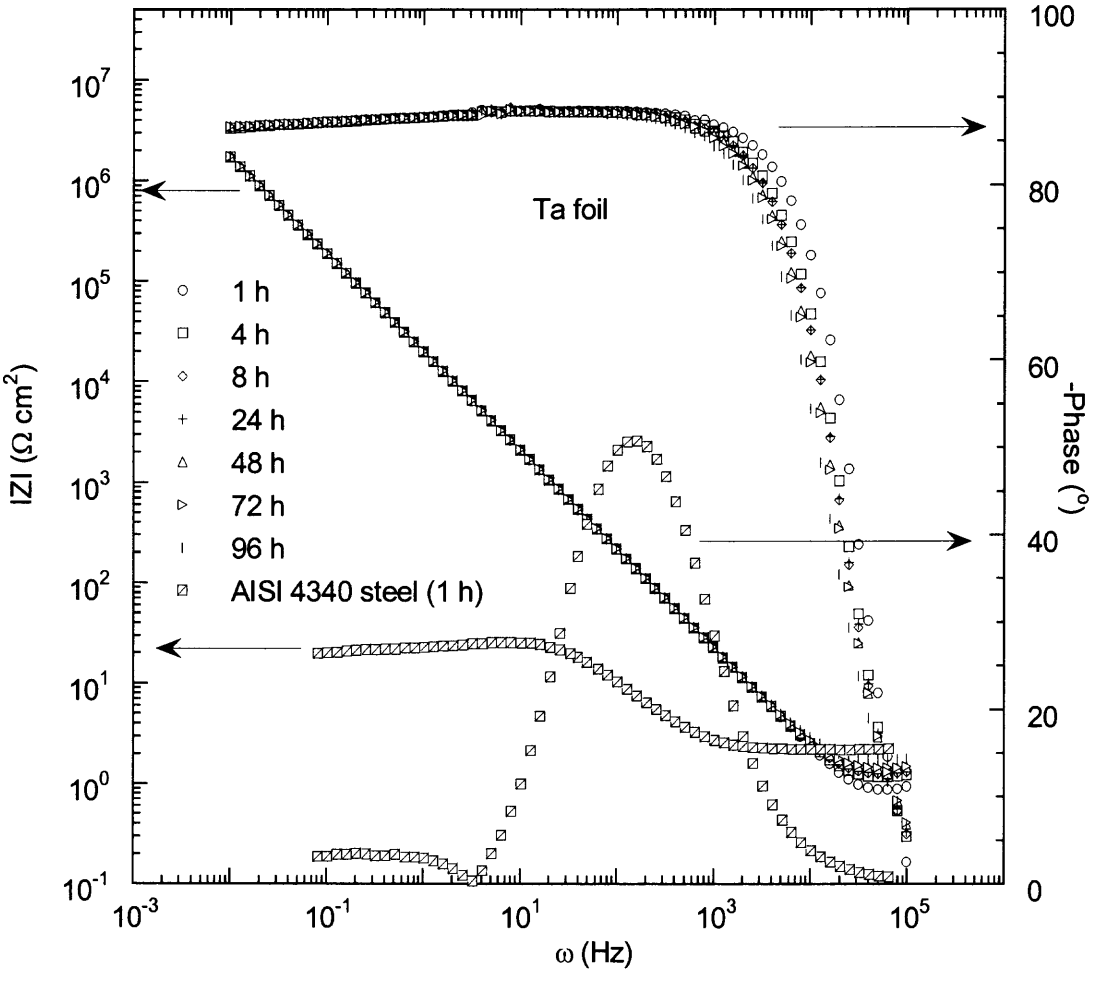

Figure 6.7 Impedance spectra of Ta foil after different immersion time and AISI 4340 steel for 1 h exposure in deaerated 0.5 M H_2SO_4 purged with N_2 at room temperature.

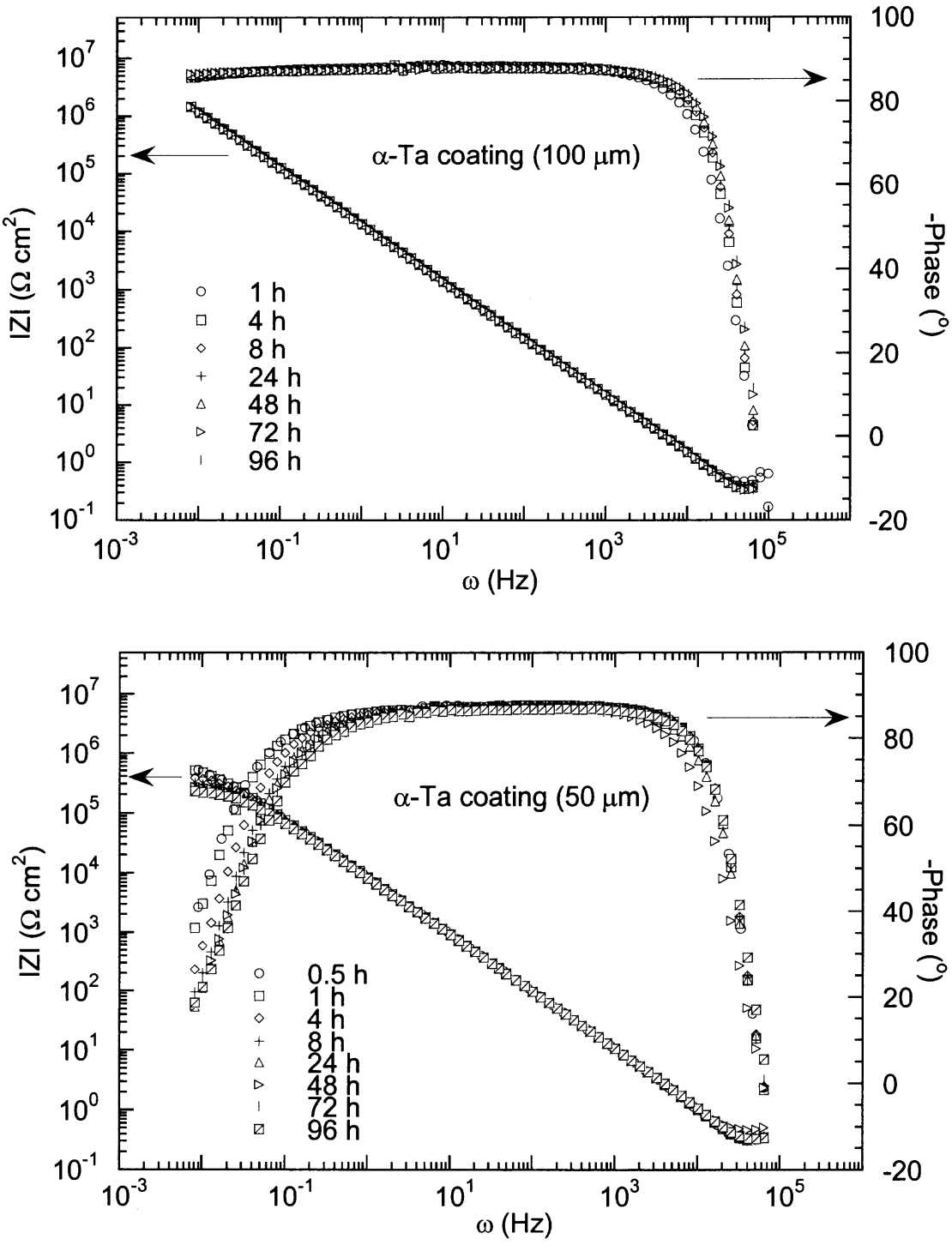

Figure 6.8 Impedance spectra of the 100 and 50 μm α-Ta coatings after different immersion time in deaerated 0.5 M H_2SO_4 purged with N_2 at room temperature.

In contrast to thick Ta coatings, the impedance of the thin Ta coatings decreases with increasing immersion time (Figure 6.9). This continuous impedance reduction for the thinner coatings can be explained by the steel substrate corrosion through open pores. Localized corrosion and delamination of the coating increase in the exposed area of steel substrate with time. While the impedance of the thin α-Ta coatings shows a gradual decrease, the impedance of the thin β-Ta coatings decreases gradually up to 24 h and then falls dramatically to that of AISI 4340 steel. Accordingly, the degree of delamination was greater for β-Ta coatings than α-Ta ones for the same time of immersion. Although some cracks and pinholes were observed in thin α-Ta coatings, β-Ta coatings were cracked around defects and delaminated by the end of experiment (Figure 6.10). The greater degree of delamination of β-Ta coatings may be caused by its brittle nature. Nevertheless, the cross sectional SEM images (Figure 6.10) show severe localized corrosion of the steel substrates under both thin α- and β-Ta coatings.

The initial phase angle responses of the thin Ta coatings, however, are very similar to that of Ta foil, reflecting capacitive behavior, which is not representative of steel substrate corrosion through open pores. However, as exposure time increases, the development of two time constants becomes evident. The short relaxation time constant, associated with a high-frequency process is related to the coating/solution interface and the dielectric characteristic of the native oxide film, whereas the low-frequency process is related to the substrate/solution interface at the open pores and represents corrosion of the steel substrate.

To analyze the impedance spectra, two equivalent circuit (EC) models are proposed, as schematically shown in Figure 6.11. The EC model in Figure 6.11a has been

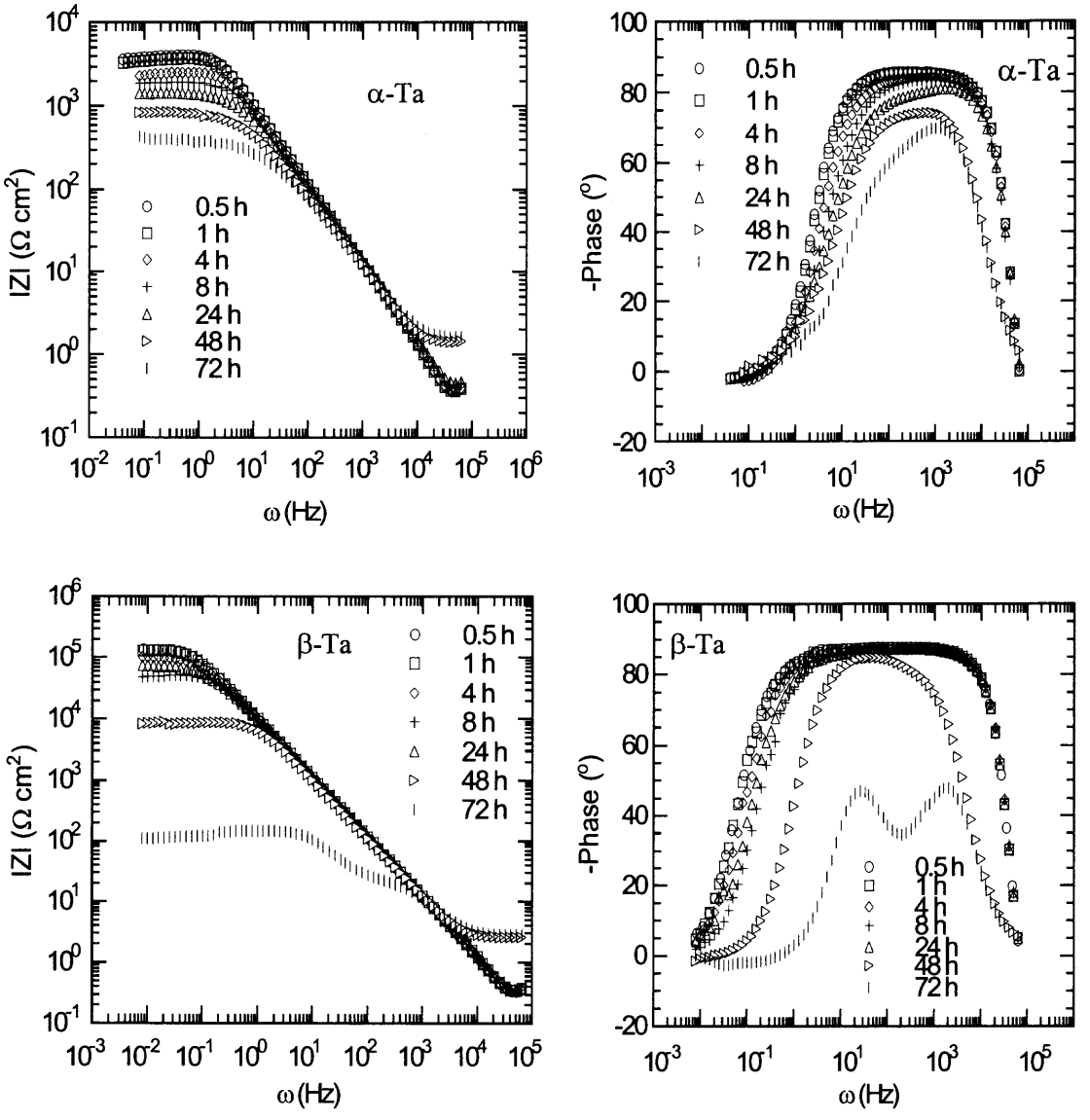

Figure 6.9 Typical impedance spectra of thin α- and β-Ta coatings (10 μm thickness) after different immersion time in deaerated 0.5 M H_2SO_4 purged with N_2 at room temperature.

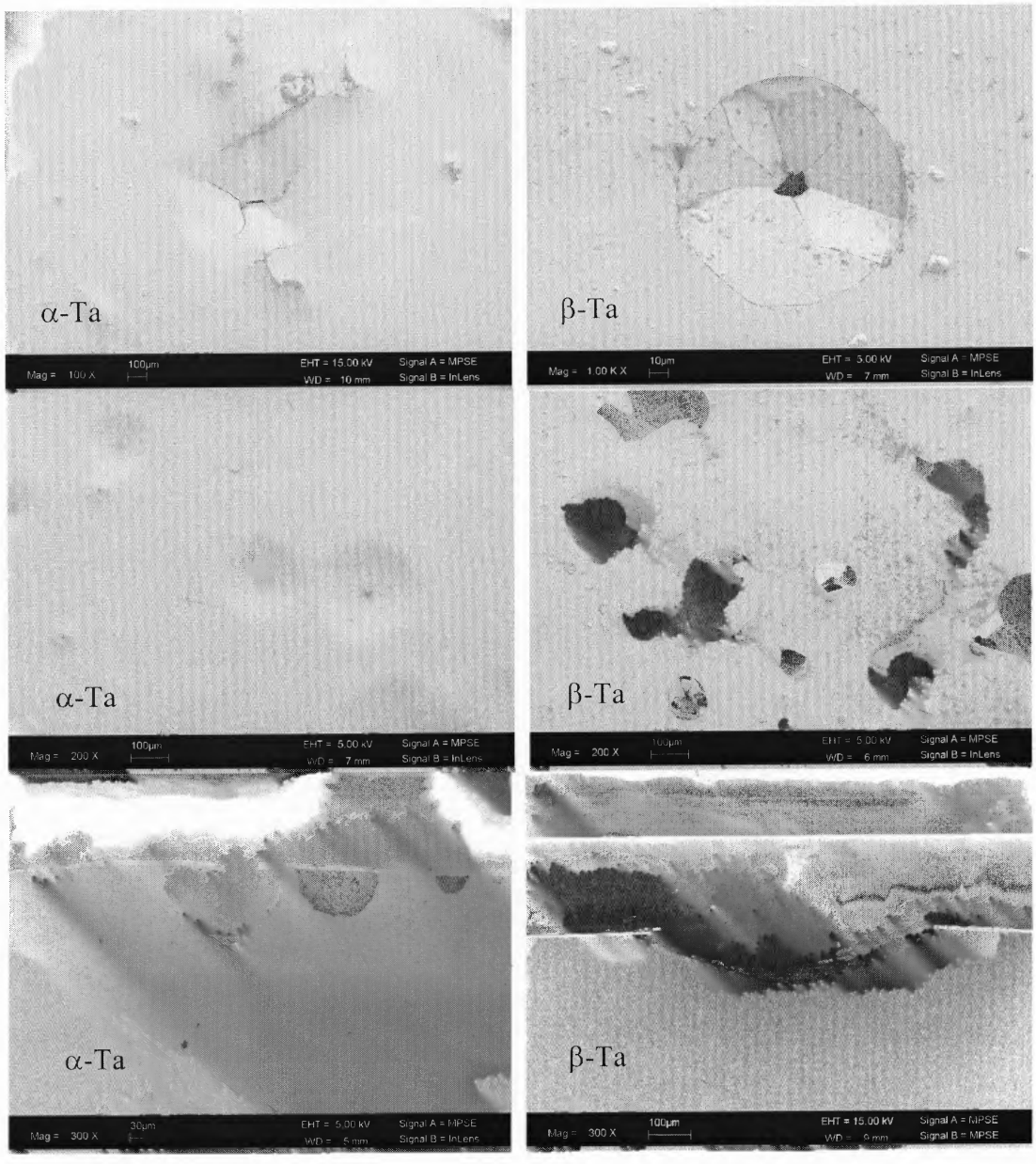

Figure 6.10 FE-SEM images of the surface and cross sections of thin α- and β-Ta coatings after the EIS measurement.

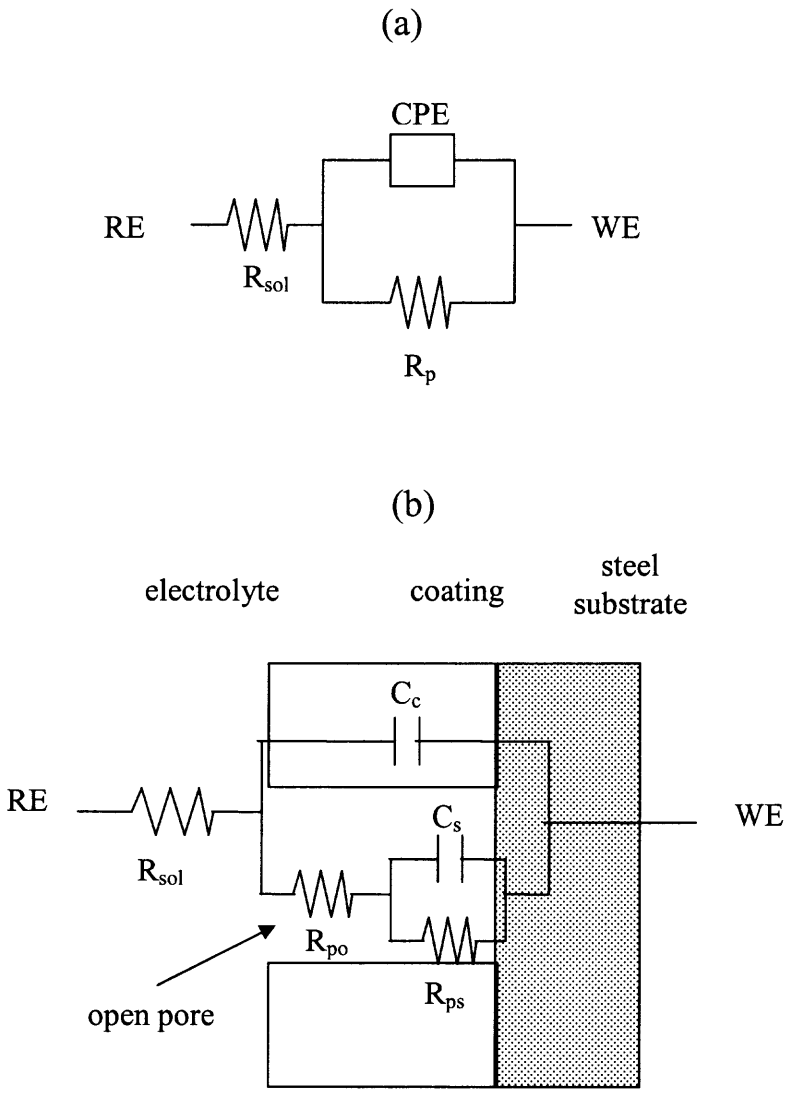

Figure 6.11 Equivalent circuit models to fit experimental EIS data: (a) used for Ta foil and the 50 and 100 μm α-Ta coatings and (b) used for thin α- and β-Ta coatings.

used for describing the impedance spectra of Ta/Ta oxide/electrolyte structure [23, 112]. Kerrec et al. [23] reported that a constant phase element (cpe) behavior, indicative of capacitance dispersion, is attributed to the heterogeneities in the tantalum oxide composition. As thick α-Ta coatings (Figure 6.8) showed very similar impedance behavior to that of Ta foil (Figure 6.7), the EC shown in Figure 6.11a was used to fit the EIS data. Here, R_p for Ta foil represents the polarization resistance of the interface between Ta and the electrolyte, and for the α-Ta coating, the total resistance is sum of the polarization resistance of the steel substrate through open pores (should any exist) and the resistance of the electrolyte in the pores of Ta coating. The evolution of R_p (Figure 6.12) reveals that the resistance of Ta foil increases with increasing immersion time up to 4 h, and then remains constant over 4 days. The increase in R_p may be due to passivation, which is confirmed by the increase in the open circuit potential as a function of time. For the 100 μm coating, however, both an increase and decrease in R_{tot} at initial exposure time was observed, while only a decrease can be seen for the 50 μm coatings. This decrease at initial times reflects electrolyte penetration in the very fine pores [104]. When open pores exist, continuous reduction in R_{tot} may be due to dissolution of the steel substrate. However, no further decrease in R_{tot} of either 50 μm or 100 μm is observed 8 h after immersion and R_{tot} becomes almost constant as seen with Ta foil.

In addition, an EDX analysis showed no evidence of corrosion from the steel substrate through pores. Therefore, the presence of open pores for such thick coatings is not likely. Nonetheless, impermeable and/or permeable pores may be important factors causing differences in the magnitude of R_{tot}; increasing coating thickness enhances the corrosion resistance. Additionally, the duplicate samples of the same thickness produced

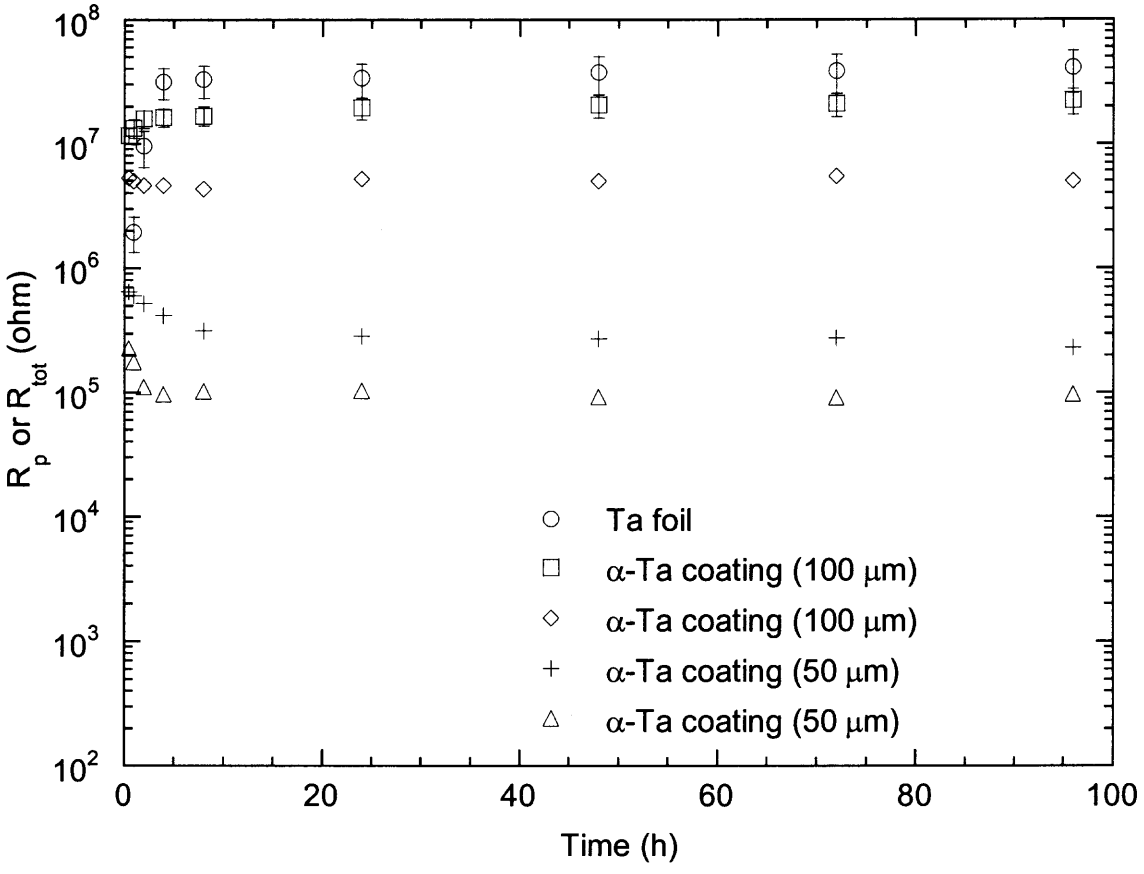

Figure 6.12 R_p of Ta foil and R_{tot} of the 50 and 100 μm α-Ta coatings as a function of time. Error bars not visible are present within symbol.

under the same sputtering conditions revealed little variation in R_{tot} for a given thickness indicating that the formation and distribution of pores are random. Overall, the thick α-Ta coatings behave like bulk Ta with respect to corrosion performance.

The EC shown in figure 6.11b has been invoked for fitting the EIS spectra of thin α- and β-Ta coatings. The model represents localized corrosion of the steel substrate exposed to the electrolyte through permeable defects in the coating, such as open pores 104, 110]. The parallel connection of R_{ps} and C_s, the polarization resistance and capacitance of the steel substrate, respectively, is representative of the electrical charge

transfer at the steel substrate/coating interface through open pores. R_{po} in series with R_{ps} and C_s is the pore resistance to the ionic current and provides information on degradation of the coating [58]. C_c represents the coating capacitance. As thin α- and β-Ta coatings show two time constants in the EIS spectra (Figure 6.9), the impedance Z at high frequency is represented by the parallel circuit (R_{pore}, C_c), with a characteristic a time constant τ_c that corresponds to the dielectric behavior of the coatings. The active pits produced at open pores are described using the other parallel subcircuit (R_{ps}, C_s) with a second time constant τ_s, reflected in the low frequency part of the EIS spectra.

Based on the model, the evolution of pore resistance (R_{po}) and polarization resistance of the steel substrate (R_{ps}) through open pores is shown in Figure 6.13. At initial exposure, the thicker β-Ta coating has a much greater R_{po} value than the thinner one, while there is no significant difference between R_{po} values of α-Ta coatings with different thickness. These results suggest that the thin β-Ta coatings have smaller voids than the thin α-Ta coatings, which results in the decreased porosity of the former coatings as their thickness increases from 5 to 10 μm, due to the void masking effect.

The continuous decrease in R_{po} and R_{ps} as a function of time is observed for both thin α- and β-Ta coatings. Specifically, the thin β-Ta coatings show a rapid decrease in R_p after 8 h for 5 μm and 24 h for 10 μm, while the thin α-Ta coatings undergo a gradual decrease in R_p during long exposure. The decrease in R_{po} is indicative of a change in pore size due to cracking and/or delamination of the coating, which is seen for thin β-Ta coatings (Figure 6.10). In contrast large pinholes and cracks were observed in α-Ta coatings after corrosion. As mentioned earlier, the greater degree of delamination of the

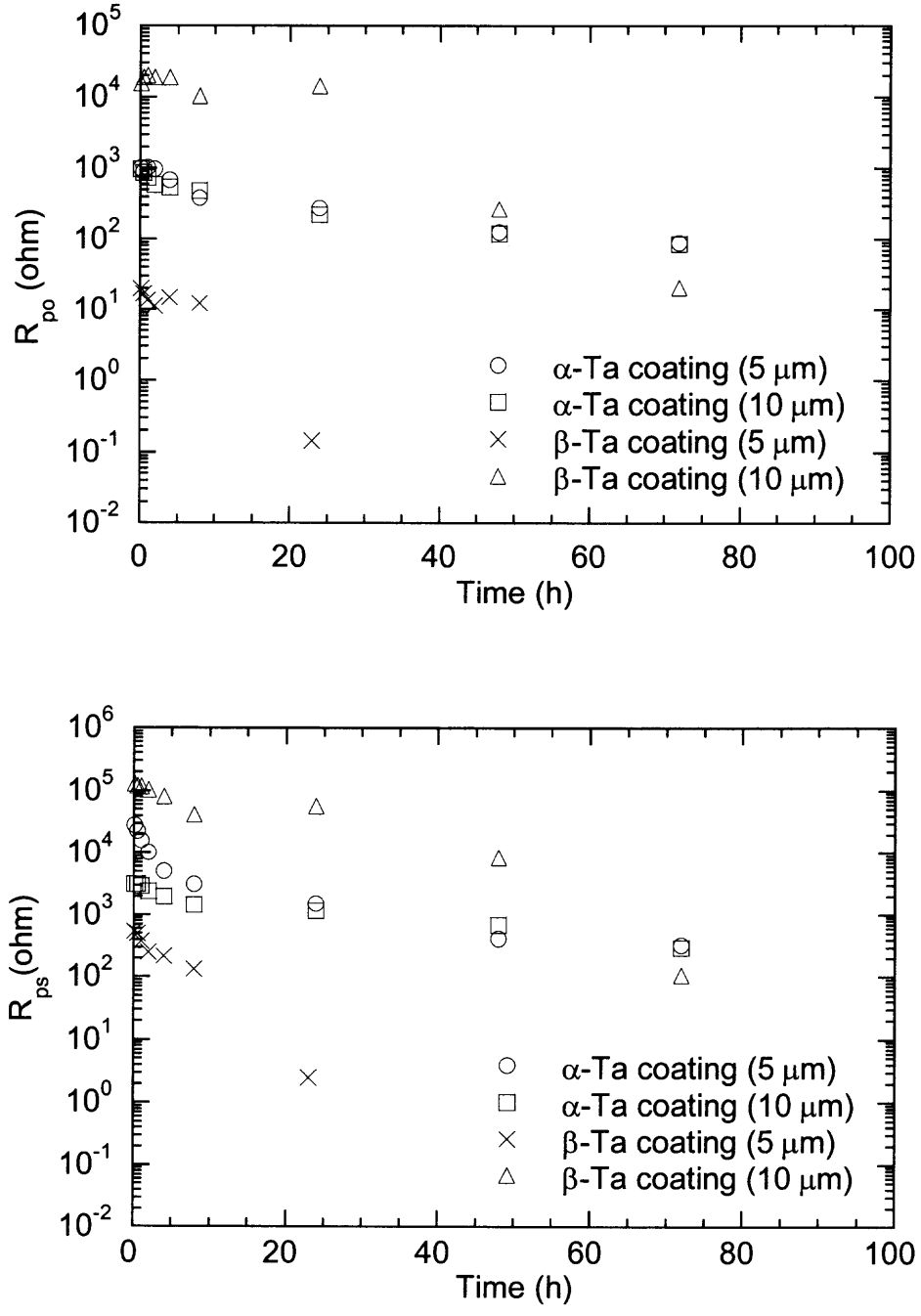

Figure 6.13 R_{ps} and R_{po} of thin Ta coatings as a function of time. Error bars are within the symbols.

β-Ta coating over α- is attributed to the brittle nature of the β phase. Therefore, the α phase is preferred over β phase with respect to corrosion performance.

The reduction of R_{ps}, indicating an increase in the surface area of steel substrate exposed to electrolyte through open pores, may be related to (a) increasing open pore area with immersion time (change in R_{po}), or (b) increasing a surface area in steel under the pore, without significant change of the pore size (small or no change in R_{po}). These two models are depicted schematically in Figure 6.14. This study reveals that β- and α-Ta coatings are more likely to exhibit case (a) and (b), respectively (Figure 6.14), when the coatings undergo corrosion over long exposure time and dissolution of the steel substrate occurs through open pores.

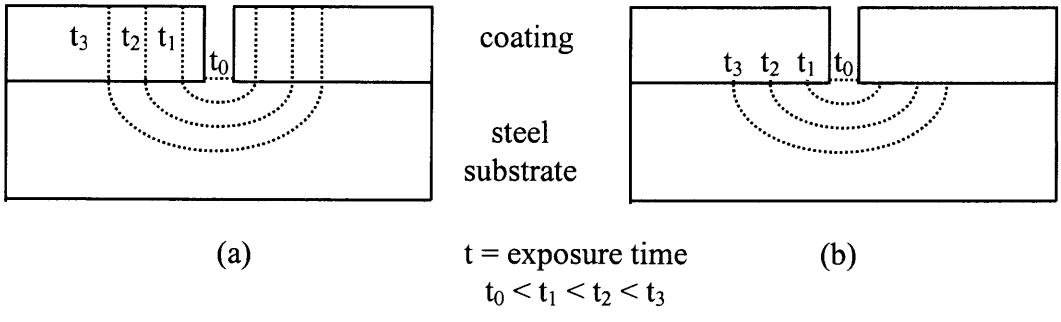

Figure 6.14 Schematic of two models for depicting the relationship between pore resistance (R_{po}) and polarization resistance (R_{ps}) of the steel substrate at open pores: (a) both R_{po} and R_{ps} decrease with time and (b) mainly R_{ps} decreases with time.

6.4 Summary

The corrosion behavior of magnetron sputtered α- and β-Ta coatings as a function of thickness was evaluated electrochemically in a deaerated 0.5 M H_2SO_4 solution. The galvanic current measurement revealed that the current density increases with an increasing ratio of cathodic (Ta) to anodic (AISI 4340 steel) areas. In galvanic coupling, the contribution of the cathodic reaction was not significant. However, the galvanic measurements demonstrated that localized corrosion is accelerated by the galvanic action when the steel substrate is exposed to electrolyte through open pores in the coating.

The polarization curves showed that the corrosion and passivation current density of α-Ta and β-Ta coatings decreased significantly with increasing coating thickness. Furthermore, at 100 μm, the polarization behavior is approximately equivalent to bulk Ta foil. The most important factor in corrosion of Ta coatings is the presence of defects such as pinholes and porosity formed during sputtering. Thus the overall corrosion process is dominated by locally active dissolution of steel, which takes place as the substrate was exposed through open pores. The impedance behavior of thin α- and β-Ta coatings over long exposure times showed that the β-Ta coating is more susceptible to delamination due to its brittle nature. Therefore, the α-phase is preferred for protecting steel. In contrast to the thin Ta coatings, no degradation was observed in the α-Ta coatings of 50 and 100 μm, of which electrochemical impedance behavior is comparable to that of bulk Ta foil. In the next chapter, the effect of the steel substrate roughness on the coating quality of α-Ta coating was studied at the minimum thickness (50 μm).

CHAPTER 7

CORROSION BEHAVIOR OF MAGNETRON SPUTTERED α-Ta COATINGS ON SMOOTH AND ROUGH STEEL SUBSTRATES

7.1 Introduction

Tantalum hard coatings deposited by sputtering, one form of physical vapor deposition (PVD) has been investigated to protect gun-bore from erosion and corrosion as bulk Ta (α phase) exhibits excellent physical and chemical properties such as a high melting point (2996 °C), good ductility, and excellent corrosion resistance in aggressive environments [6, 98]. However, when deposited as a film on steel substrates, either the α-phase (body-centered cubic structure), β-phase (tetragonal structure), or a mixture of both phases have been observed under varying deposition conditions [99, 105]. Since β-Ta is brittle, α-phase is preferred in protecting gun-bore against erosion. Additionally, the β phase has been reported to be more susceptible to delamination than the α-phase and hence to be less corrosion resistant [113].

Coating qualities such as density, thickness, and porosity are important in corrosion resistance [101, 114, 115]. The previous study investigating corrosion behavior as a function of thickness showed that α-Ta coatings 50 μm or more in thickness, behaved as well as Ta foil [113]. In this earlier work, the steel substrate was polished down to the rms roughness of 50 nm using a diamond suspension. Surface preparation of substrates can critically affect the morphology of PVD deposits. In particular, substrate surface roughness have been shown to influence the corrosion behavior [103], as an

increased substrate roughness resulted in more coating defects due to a shadowing effect during PVD film growth. A study on the relationship between surface roughness and pinhole formation in TiN films showed that a smoother substrate surface yielded a lower pinhole density, resulting in improved corrosion resistance [116]. As the peak-to-valley height on the substrate profile increases, there is an increasing tendency for coating defects to form. Liu et al. [71] studied the coating porosity of a PVD CrN on mild steel substrates prepared by grinding with 220 grit SiC and polishing with 6 and 45 μm diamond paste. They observed a reduction in coating defects with decreasing surface roughness. While the previous work demonstrated that viable corrosion resistant α-Ta coatings with a thickness of 50 μm or greater were produced on polished AISI 4340 steel substrates, the objective of this study is to compare the corrosion behavior of the coatings deposited on smooth and rough surfaces, the latter of which may be more representative of the actual gun-bore condition.

7.2 Experimental Methods

AISI 4340 steel coupons (1.26 × 1.26 cm^2) were prepared by grinding with 60 grit aluminum oxide for the rough surface simulating potentially the gun-bore, and by mechanical polishing with a diamond suspension down to 0.05 μm for the smooth surface. Both types of substrates were then cleaned electrochemically and in an ultrasonic baths of organic solvents (acetone, followed by alcohol). The final cleaning steps performed in the process chamber consisted of baking at 200°C for 7 h in high vacuum (1×10^{-5} Pa), sputter etching in an argon plasma. The α-Ta coatings of 50 μm (± 20%)

thickness were deposited by DC magnetron sputtering. The details of the process are described elsewhere [105, 113]. Ta foil (99.9 %) and the rough and polished steel substrates (AISI 4340) were used as reference samples in electrochemical tests.

Characterization included crystallographic phase identification with x-ray diffraction (XRD) and microscopic roughness measurements with atomic force microscopy (AFM). Before and after the corrosion tests, the surface and corrosion features of coated samples were examined using a field emission scanning electron microscope (FE-SEM) with qualitative elemental analysis by energy dispersive X-ray spectroscopy (EDX). Additionally, to obtain the local structural information, extended x-ray absorption spectroscopy (EXAFS) experiments using total electron yield (TEY) mode were carried out at the Ta L_{III} edge (E_0 = 9881 eV) on beamline X11A at the National Synchrotron Light Source (NSLS), Brookhaven National Laboratory. The storage ring operated at the energy of 2.80 GeV with an average current of 180 mA. A Si (111) double-crystal monochromator was used for the photon energy selection, and the second Si crystal was detuned to approximately 80% of maximum transmitted x-ray intensity to minimize the presence of higher harmonics in the beam. Data from the coating and a reference Ta foil were collected over the energy range of 9.732 – 10.986 keV and analyzed following standard procedures [96].

The electrochemical corrosion behavior was studied with potentiodynamic polarization and electrochemical impedance spectroscopy (EIS) in deaerated 0.5 M H_2SO_4 using a Gamry PC4/300 potentiostat/galvanostat/ZRA system. Additional experimental details are described in Chapter 5 [113]. The working electrode (WE) was the coating with an exposure area of 1 cm^2 and a saturated calomel electrode (SCE) was

employed as a reference electrode to measure the potential across the electrochemical interface. A platinum grid was used as the counter electrode (CE). Potentiodynamic polarization was measured at the corrosion potential (E_{corr}) 1 h after immersion in an effort to reach the quasi-stable potential. The polarization curves were obtained by sweeping from –0.2 to +1.5 V (vs. E_{corr}) with a scan rate of 10 mV/min. Impedance spectra in the frequency range from 10 mHz to 100 kHz, with an excitation signal amplitude of 10 mV (r.m.s) at E_{corr}, were collected over 0.5, 1, 4, 8, 24, 48, 72, and 96 h. The EIS data were interpreted on the basis of an equivalent circuit using complex nonlinear least squares fitting (CNLS) LEVM algorithm [68] in the Gamry Echem Analyst software.

7.3 Results and Discussions

7.3.1 Phase and Structure of the Ta Coatings

The α-Ta coating on the polished steel substrate shows (222) preferred orientation, while the coating on the rough substrate exhibits a very similar pattern to Ta powder, in which (110) peak has the highest intensity (Figure 7.1). All peaks can be indexed as α Ta peaks. Peak broadening observed in all the peaks of both coatings, as compared to Ta powder, can be attributed to microstrain and particle size. In addition to the long range structure, the short range structure of both coatings was compared by conducting EXAFS. The Fourier transforms (FT) of the EXAFS ($\chi(k)k^3$) spectra (Figure 7.2) over 1.78 to 3.05 Å correspond to the first coordination shell in the vicinity of the absorbing atom. This atomic short-range structure for both coatings is consistent with the theoretical EXAFS of

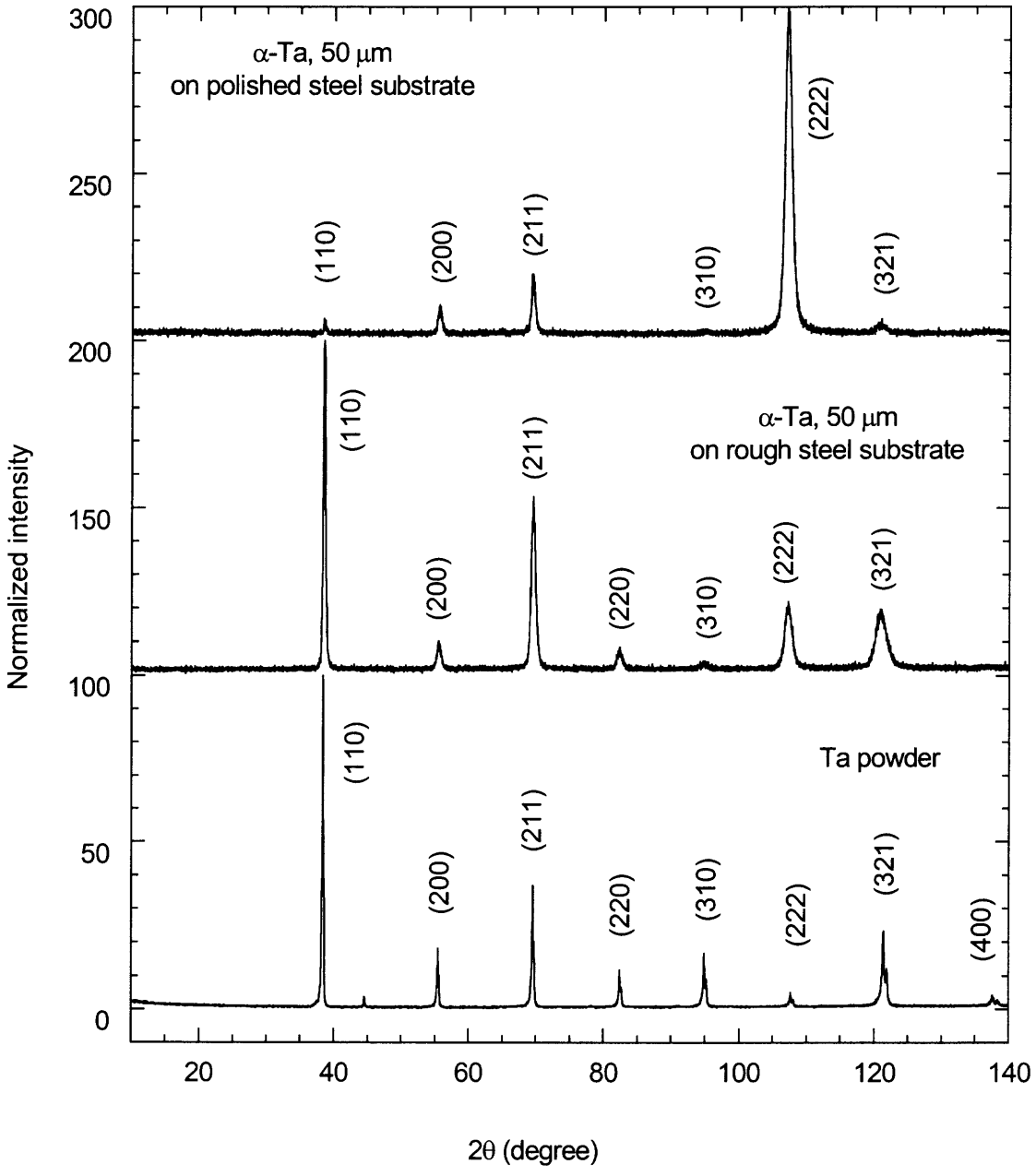

Figure 7. 1 X-ray diffraction patterns of α-Ta coatings on the smooth and rough steel substrates and Ta powder. XRD patterns are normalized with respect to the peak with maximum intensity in each spectrum.

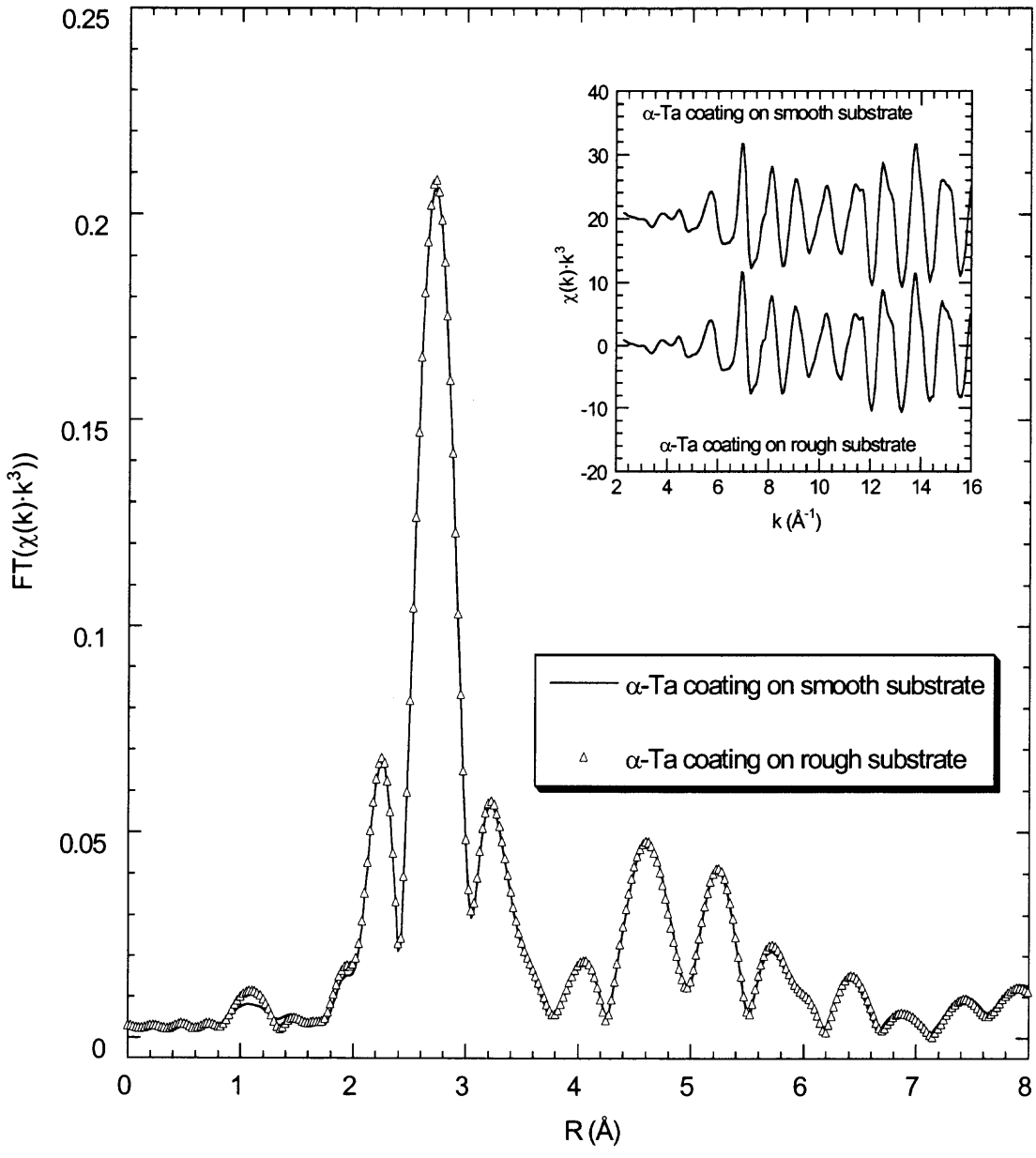

Figure 7.2 Fourier transforms of Ta L_{III}–edge $\chi(k)k^3$ spectra of α-Ta coatings on the smooth and rough steel substrates over the k range 2.85 – 16.3 Å. Ta L_{III}–edge $\chi(k)k^3$ spectra is shown in the insert.

Table 7.1 Results of EXAFS fits* on the first shell for α-Ta coatings on the smooth and rough steel substrate Fourier transformed over 2.85 to 15.8 $Å^{-1}$ k-range and fitted over 1.78 to 3.05 Å r-range.

	α-Ta coating on smooth steel substrate	α-Ta coating on rough steel substrate	α-Ta XRD model
N	8.81	8.60	8.00
R (Å)	2.85	2.85	2.86
σ^2 ($Å^2$)	0.005792 ± 0.000064	0.005739 ± 0.000120	0

N, R, and σ^2 are coordination number, interatomic distance, and Debye-Waller factor, respectively.
* S_0^2 was set as 1.0. N and R have errors of ± 20% and ± 0.02 Å, respectively.

α-Ta (Table 7.1) with 8-9 Ta atoms at 2.85 Å. It is interesting to note that only the long-range order is affected by the surface roughness while the short-range structure of the coatings on the two types of substrates appears to be the same.

The surface roughness of the substrates over 100 × 100 μm^2 area was measured by AFM to be 12.4 ± 1.9 nm (r.m.s) for the smooth surface and 929.5 ± 246.1 nm (r.m.s) for the rough surface (Figure 7.3a and b). Subsequent to sputtering, the coating revealed the same order of magnitude in roughness with 62.6 ± 4.6 nm (r.m.s) for the smooth substrate and 824.9 ± 80.6 nm (r.m.s) for the rough one (Figure 7.3c and d). These results indicate conformal coverage, with the film following the substrate topography (Figure 7.3b and d). Interestingly, over 2 × 2 μm^2 scanned area (Figure 7.3e and f), the roughness of Ta coatings on the smooth and rough substrates are 26.6 ± 2.7 and 33.1 ± 5.0 nm, respectively, indicating no significant difference in the microscopic roughness for the Ta coatings. Because of the limited vertical range of the AFM, the surface was also

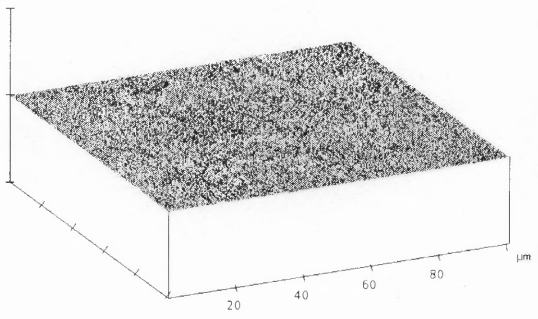

(a) Polished steel substrate

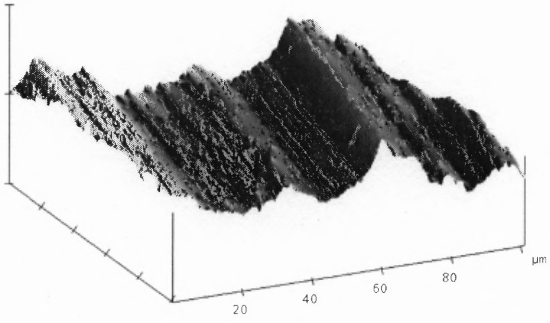

(b) Rough steel substrate

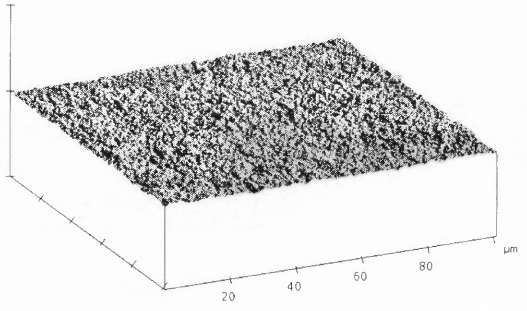

(c) α-Ta 50 μm on polished steel substrate

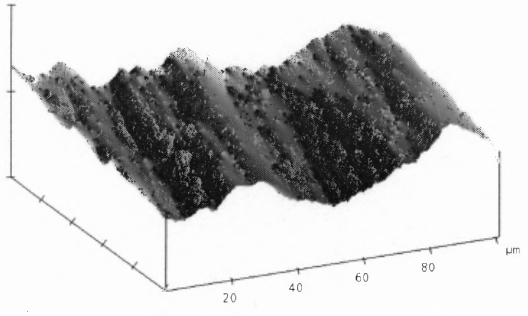

(d) α-Ta 50 μm on rough steel substrate

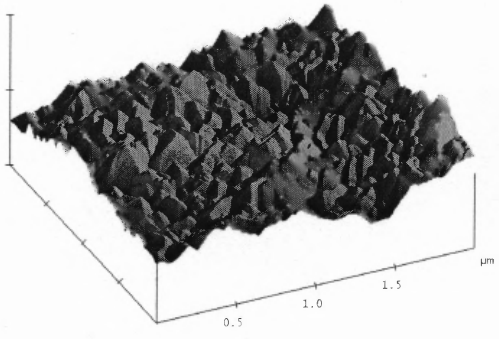

(e) α-Ta 50 μm on polished steel substrate

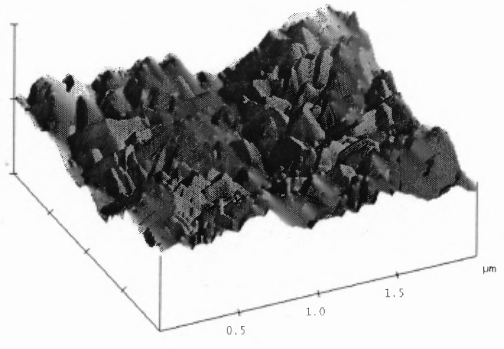

(f) α-Ta 50 μm on rough steel substrate

Figure 7.3 AFM surface plots of the smooth and rough steel substrates (a, b) and α-Ta coatings on these substrates (c – f). Scans (a – d) were performed over 100 × 100 μm^2 area and scans (e – f) over for 2 × 2 μm^2. The vertical, z scale, unit is 5 μm for (a – d) and 200 nm for (e, f).

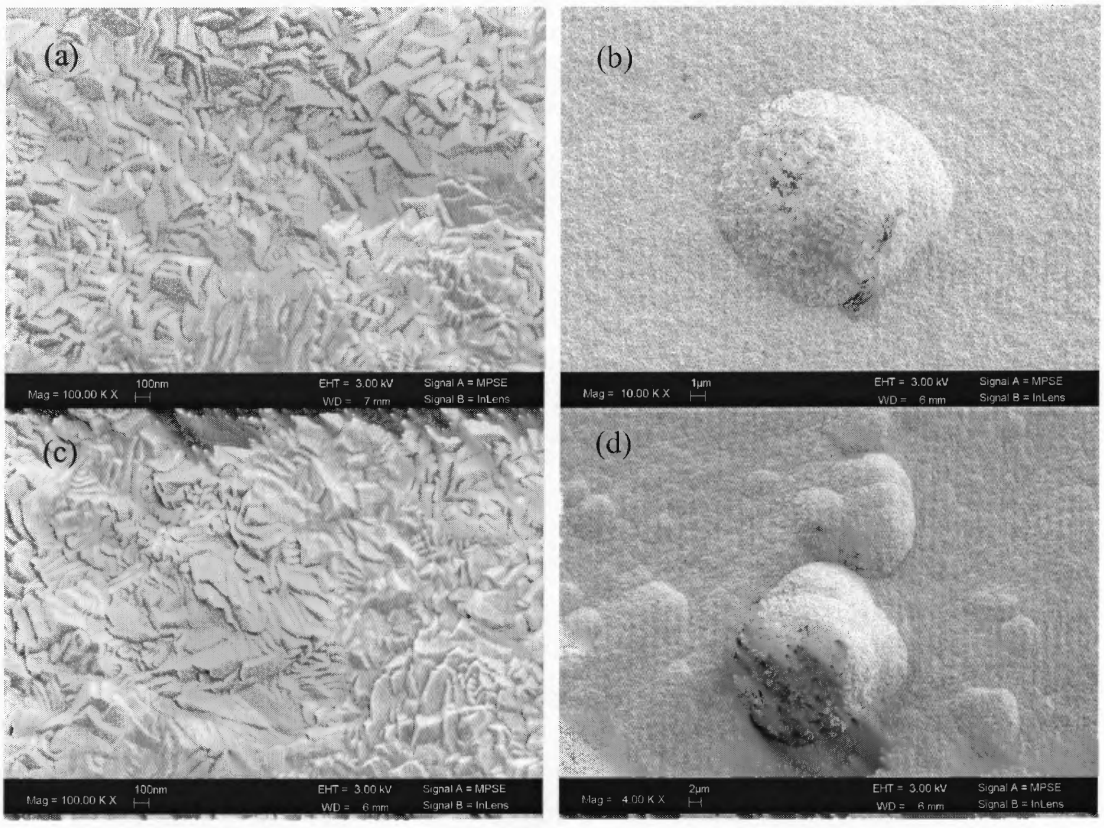

Figure 7.4 SEM images of α-Ta coatings (50 µm thick) on the smooth and rough steel substrates showing droplet like defects; (a) α-Ta coating on smooth steel substrate and (b) β-Ta coating on rough steel substrate.

examined with a profilometer (Dektak) over 2 mm and showed an average roughness (Ra) of 1100.0 ± 51.3 nm and 1054.5 ± 129.7 nm, before and after deposition on the rough substrate (APPENDIX B). The peak to valley distance was approximately 5 µm. Furthermore, the FE-SEM images of the Ta coating on both types of substrates showed no apparent difference in their morphology (Figure 7.4a and c). Droplet-like defects, which are commonly observed in the PVD films [104, 108], are seen on the coated surface regardless of surface roughness (Figure 7.4b and d). Although the AFM images at multiple scales suggest uniform coverage of both types of substrates, an analysis of open

pores, or porosity, due to defects is critical before concluding that the substrate roughness is not important for the coating viability.

7.3.2 Porosity Assessment

Anodic polarization curves measured on smooth and rough steel substrates (AISI 4340), and the α-Ta coatings deposited on these substrates, in 0.5 M H_2SO_4 deaerated with N_2 at room temperature are shown in Figure 7.5. The results of measurements performed on Ta foil are also shown for reference. Both the smooth and rough steel substrates show very similar polarization behavior, except that the current density of the rough substrate before the passivation potential is greater than that of the smooth substrate (Figure 7.5). The current density is based on 1 cm^2 of the exposed area. Therefore, considering that the actual surface area is proportional to surface roughness, the larger current density for the rough substrate may be attributed to a larger actual area as compared to the smooth substrate.

The α-Ta coatings on both substrates show almost identical polarization behavior regardless of surface roughness; however, the current density for the coating on the rough substrate is shifted upwards, which may be attributed to the roughness and coating porosity. Additionally, our previous study suggested no significant effect of crystallographic orientation on anodic polarization behavior of α-Ta [113]. Therefore, the difference in the current density over the passive region was not likely to be caused by the different orientation of the α-Ta coatings. At open circuit potential, the coatings exhibit approximately two orders of magnitude smaller polarization resistance than the Ta foil (Table 7.2). Nevertheless, the coating is chemically inert [113] and hence, the

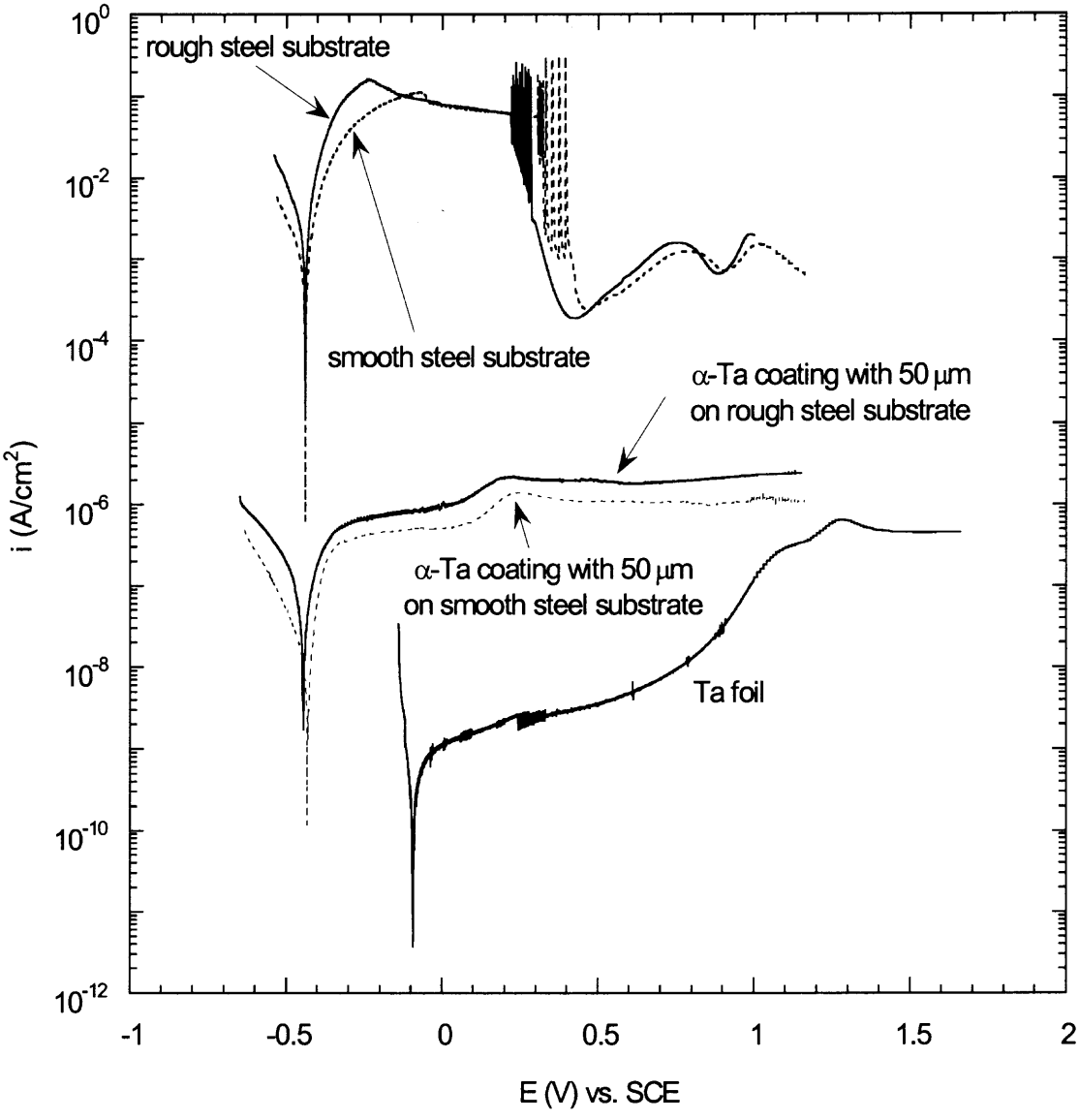

Figure 7.5 Anodic polarization curves of smooth and rough steel substrates (AISI 4340), α-Ta coatings deposited on these substrates and of Ta foil, in 0.5 M H_2SO_4 deaerated with N_2 at room temperature.

Table 7.2 Electrochemical characteristics of α-Ta coatings with different roughness, the smooth and rough steel substrates and Ta foil.

	α-Ta coatings with 50 μm thickness		Steel substrate		Ta foil
	on smooth substrate	on rough substrate	smooth surface	rough surface	
E_{corr} (mV vs. SCE)	-433	-445	-439	-440	-94
R_p (ohm)	1.09×10^6	2.97×10^5	13.54	5.20	3.14×10^7
b_a (mV/decade)			50.7	46.8	

polarization resistance at the open circuit potential represents the resistance of the steel substrate exposed to the electrolyte at the open pores. The porosity index, P, representing the area ratio of total pores to total exposed surface can be estimated using Equation [101]:

$$P = \left(\frac{R_{PS}}{R_P} \right) \times 10^{-|\Delta Ecorr| / b_a} \tag{7.1}$$

where R_p and R_{ps} are the polarization resistances of the Ta coated steel and bare steel substrate, respectively; ΔE_{corr} is the difference between the corrosion potentials of the Ta coating and the bare steel substrate; and b_a is the anodic Tafel slope for the bare steel substrate (Table 7.2). Equation (7.1), with the measured polarization resistance data, gives the porosity of the coatings on the smooth and rough steel substrates as 7.92×10^{-4} and 9.43×10^{-4}%, respectively, indicating a negligible difference. This result implies that

the surface roughness of steel substrate does not significantly influence the quality of Ta coatings at 50 μm. However, the corrosion resistance may be impacted as a function of immersion time due to potential delamination of the coating initiated at open pores and/or blocking of open pores by corrosion product [104, 110, 111].

7.3.3 Corrosion Behavior as a Function of Time

The results of the electrochemical impedance spectroscopy measurements are shown in Figure 7.6. The spectra of α-Ta coatings on the smooth and rough steel substrates show that there is no significant change in the impedance at the lowest frequency over 4 days of exposure. The phase angle responses on these coatings are very similar to that measured on Ta foil, shown in Figure 6.7. Only one relaxation time constant is present in the EIS spectra of the coatings and of Ta foil [113]. In the case of ceramic and polymer coatings, the magnitude of the impedance in low frequency range represents total resistance, which is sum of the polarization resistance of the metal substrate through open pores and the pore resistance [104, 108, 110, 111]. Our previous EIS study demonstrated that as the degradation of the protective coating proceeds, a transformation from a single to two relaxation time constants was observed in the phase angle spectra [113]. However, substrate corrosion and coating delamination were not seen in that study.

The equivalent circuit (EC) model consisting of a parallel combination of a polarization resistance (R_p) and a constant phase element (CPE) in series with solution resistance (R_{sol}) was applied to fit the EIS data for Ta foil and the coatings (Figure 7.7). For Ta foil, R_p represents the polarization resistance of the interface between Ta and electrolyte. As for the α-Ta coating, R_p characterizes the total resistance, which is the

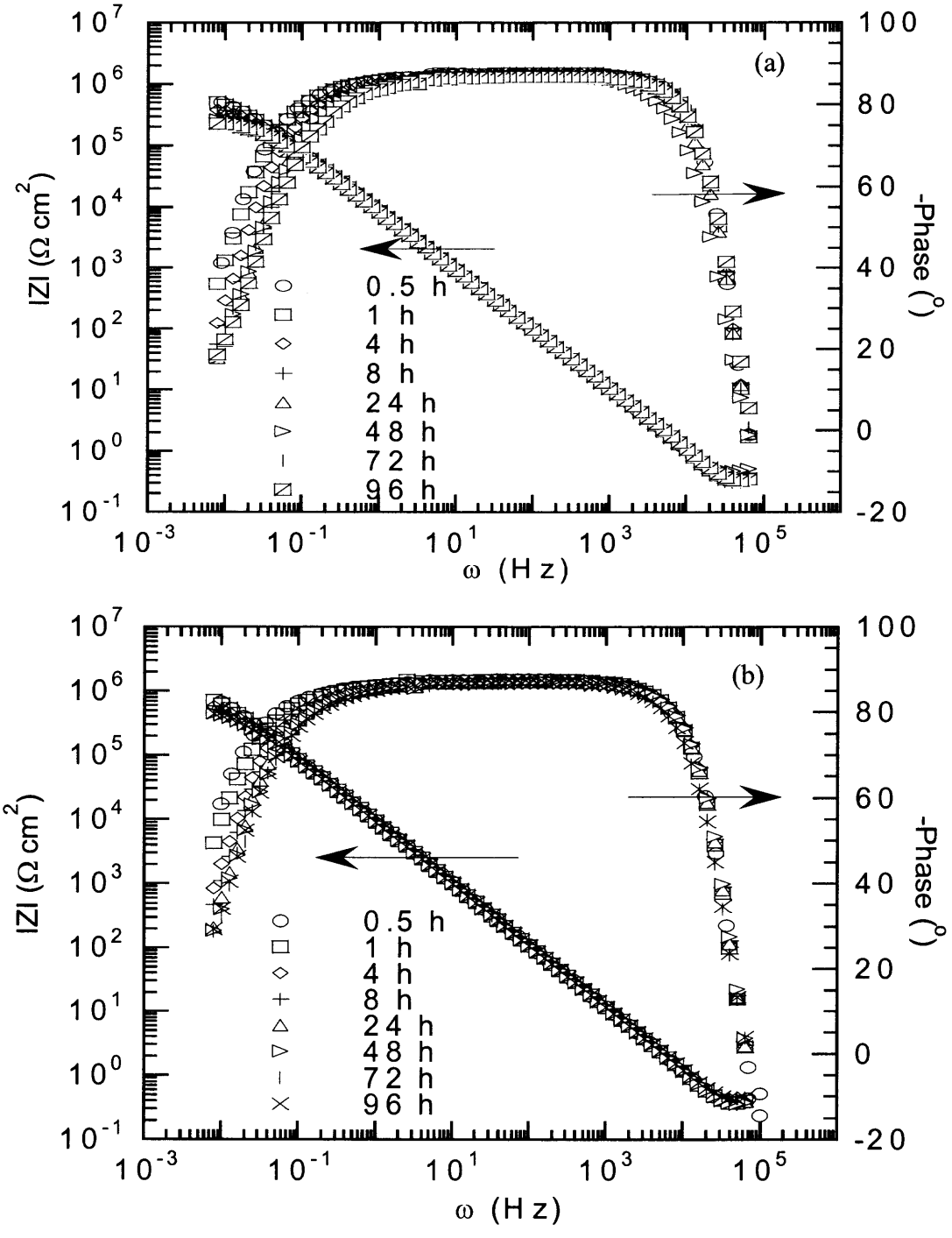

Figure 7.6 Impedance spectra of α-Ta coatings for different immersion time in deaerated 0.5 M H_2SO_4 with N_2 at room temperature; (a) and (b) represent α-Ta coatings on smooth steel substrate; (c) and (d) α-Ta coatings on rough steel substrate.

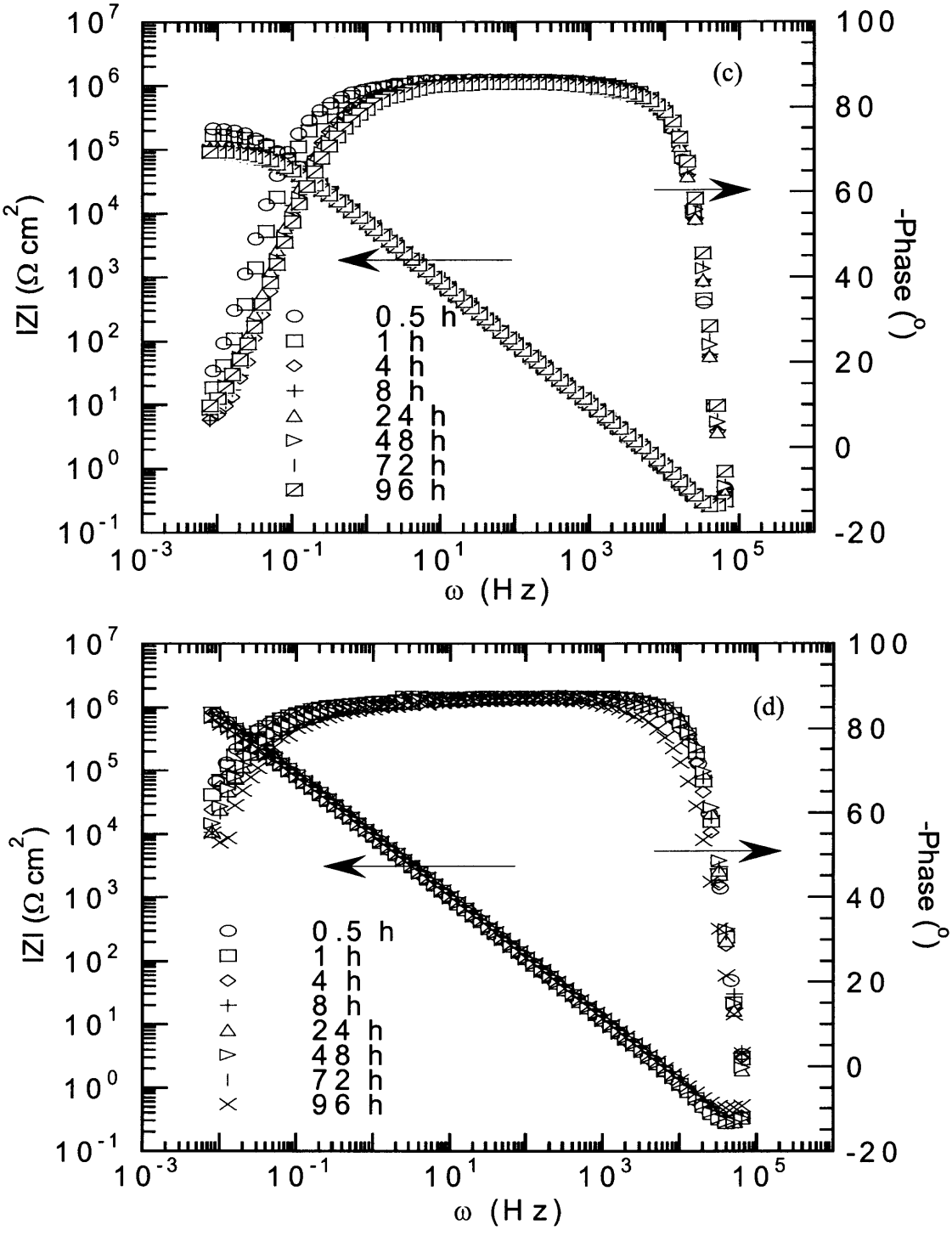

Figure 7.6 (continued)

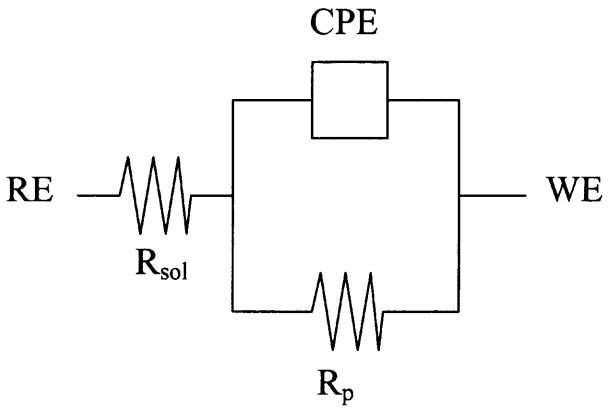

Figure 7.7 Equivalent circuit models for fitting experimental EIS data of Ta foil and α-Ta coatings.

sum of the polarization resistance of the steel substrate through open pores and the resistance of the electrolyte in the pores of the Ta coating. The data presented in Figure 7. 8 show that R_p of Ta foil increases with the immersion time up to 4 h, and then remains constant for over 4 days. The increase in R_p may be due to passivation, which is confirmed by the increase in the corrosion potential as a function of immersion time. For the Ta coatings, R_{tot} decreases at initial times reflecting electrolyte penetration in the fine pores (Figure 7.8) [110]. No further decrease in R_{tot} on either smooth or rough steel substrates is observed 8 h after immersion and in fact it becomes almost constant, as seen also with Ta foil. In addition, an EDX analysis showed no evidence of substrate corrosion through open pores. Therefore, the presence of open pores for such thick coatings is in question. Additionally, repeated depositions under the same sputtering conditions produced samples with the same values of R_{tot} regardless of the substrate roughness. This result demonstrates that there is no significant effect of substrate roughness on the coating quality for at least 50 μm with respect to corrosion performance. Additionally, the

small variation of total resistance (R_{tot}) for each sample indicated that the formation and distribution of pores were random.

Lee et al. [107] studied the corrosion behavior of 2.36 μm CrN films on steel substrate with roughnesses of 0.10, 0.20 and 0.31 μm (Ra), of which the ratio of coating thickness to substrate roughness was 23.6, 11.8, and 7.61, respectively. They observed that the coating porosity increased with increasing roughness and thus the corrosion rate increased. In all cases, coating failure was observed. Similarly, for a PVD CrN coating,

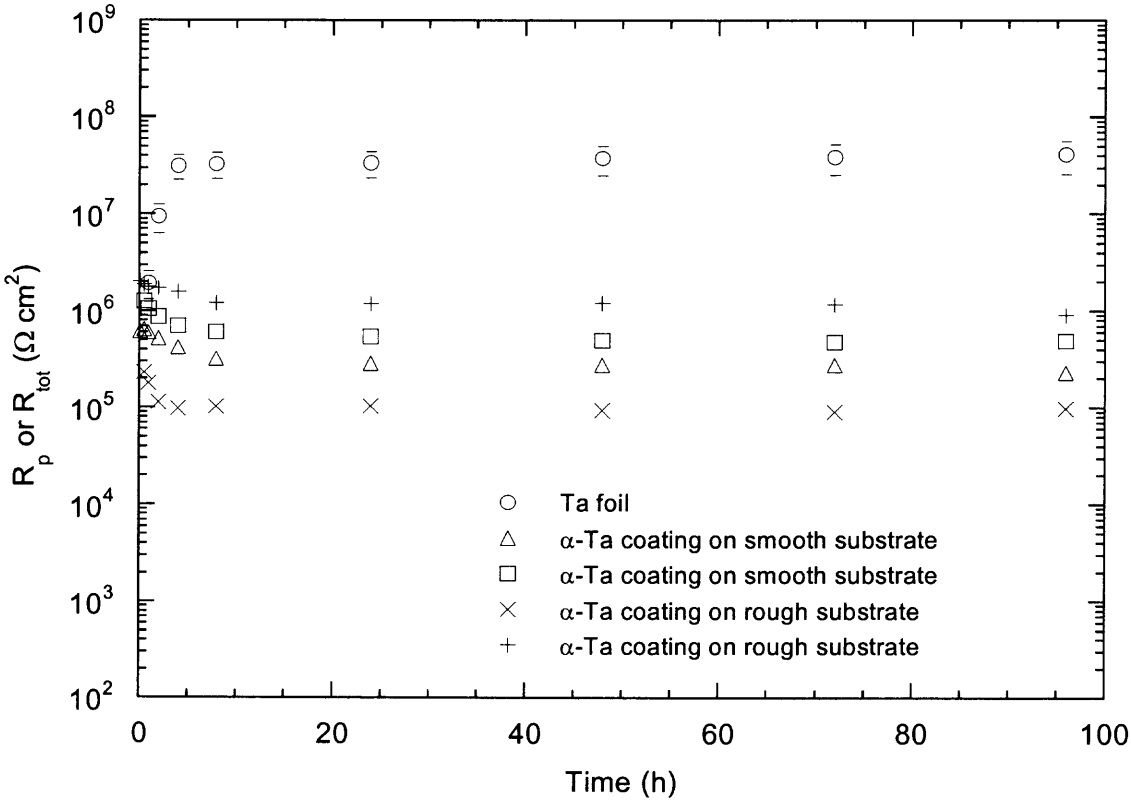

Figure 7.8 R_p and R_{tot} of Ta foil and α-Ta coatings on the smooth and rough steel substrates as a function of time. Error bars not visible are present within symbol.

Lui et al. [71] found a decrease in defects as surface roughness decreased with polishing, which changed from 220 grit SiC to a 6 μm diamond paste. Our results suggest the existence of a critical aspect ratio of the coating thickness to the substrate roughness, above which there is no effect of substrate roughness on the coating porosity.

7.4 Summary

The analysis of sputtered α-Ta coatings on steel, showed that while the long-range crystallographic orientation, seen in XRD patterns, is affected by the substrate surface roughness, the short-range structure is equivalent to the bulk α-Ta. The latter has been demonstrated by EXAFS measurements of the Ta-Ta coordination in the first shell (1.78 Å ≤ R ≤ 3.05 Å). Although the substrate surface roughness was two orders of magnitude greater for the coatings deposited on the rough substrate than the smooth one, the porosity was only 7.92×10^{-4} for the smooth substrate and 9.43×10^{-4} % for the rough one, representing a negligible difference. The coatings deposited on both substrates showed almost identical anodic polarization behavior; although the corrosion current density was slightly higher in the case of the coating on the rough substrate. The electrochemical impedance behavior of the coatings over long exposure times was similar to that of Ta foil, revealing a high corrosion resistance. Moreover, repeated deposition under the same sputtering conditions on substrates with different roughness produced samples that had the same corrosion resistance over all exposure times studied. This result implies that there is no significant effect of substrate roughness on corrosion performance, at least when the ratio of coating thickness to the surface roughness

(maximum surface height excursions) is greater than 10. In the next chapter, the comparison of corrosion behavior between Ta coatings and Cr coatings from full scale processes was studied.

CHAPTER 8

CORROSION BEHAVIOR OF ELECTRODEPOSITED AND SPUTTERED Cr COATINGS AND SPUTTERED Ta COATINGS WITH α- AND β-PHASE

8.1 Introduction

Electrochemically deposited chromium coatings have been used as protective coatings against erosion and corrosion of gun bores because of their high wear and corrosion resistance [6, 98]. However, hexavalent chromium is a known carcinogen and associated wastes are hazardous and difficult to dispose. Therefore, efforts to replace electrodeposited (ED) Cr include for example, physical vapor deposition (PVD) of Cr and a more environmentally friendly material and process such as magnetron sputtered tantalum [98, 117].

When deposited as a film on steel substrates, more than one phase of tantalum forms: α-phase (body centered cubic structure), which is stable and ductile, and β phase (tetragonal structure), which is meta-stable and brittle. Both α- and β-phases have been observed under varying sputtering conditions [98, 105]. Because of the brittle nature of the β-phase, α is preferred for the purpose of protecting the gun bore against erosion. A metal coating deposited without impurities or defects should exhibit corrosion behavior comparable to that of the bulk metal. However, in practice it is generally not feasible to achieve such coatings, especially for thin ones. Consequently, the potential presence of defects (i.e., pinhole, open pores) in coatings may result in severe localized corrosion [14]. Our previous study investigating the corrosion behavior of the α-Ta coating by planar magnetron sputtering showed that at 50 μm or greater, the coating behaves almost

equivalently to the foil [113]. Furthermore, for thin Ta coatings (< 10 μm), β-phase is more susceptible than α-phase to delamination due to localized corrosion at open pores.

The objective of this paper is to evaluate the corrosion behavior of sputtered Ta and Cr coatings produced in full-scale process and compare the performance to that of the electrodeposited Cr coating. Cylindrical magnetron sputtering was applied in producing α- and β-Ta coatings as well as Cr. Morphological evaluation of the surface before and after electrochemical analysis was performed using scanning electron microscopy with energy dispersive x-ray spectroscopy for elemental analysis.

8.2 Experimental Methods

The substrate for the Cr coatings is ASTM A723 (gun steel) steel cylinders. High contractile (HC) Cr with 100 μm thickness was electrochemically deposited; this is the conventional coating for gun bore [118]. The PVD Cr coating with 120 μm thickness was prepared by a cylindrical magnetron sputtering system. As for Ta coatings, the α-Ta with 38 μm and β-Ta with 50 μm were deposited on AISI 4340 steel also by a cylindrical magnetron sputtering.

In comparing coating performance, a number of analyses were conducted. To obtain local structural information of Cr and Ta coatings, extended x-ray absorption spectroscopy (EXAFS) experiments using total electron yield (TEY) mode were carried out at the Cr *K* edge (E_0 = 5989 eV) for Cr coatings and Ta L_{III} edge (E_0 = 9881 eV) for Ta coatings on beamline X11A at the National Synchrotron Light Source (NSLS), Brookhaven National Laboratory. The storage ring operated at the energy of 2.80 GeV

with an average current of 180 mA. A Si (111) double-crystal monochromator was used for the photon energy selection, and the second Si crystal was detuned to approximately 50% (Cr coatings) and 80% (Ta coatings) of maximum transmitted x-ray intensity to minimize the presence of higher harmonics. EXAFS data were collected over the energy range of 5.839 – 7.093 keV for Cr coatings and a reference Cr foil and 9.732 – 10.986 keV for Ta coatings; spectra were analyzed following standard procedures [96]. Additionally, the crystallographic phase identification was accomplished using conventional x-ray diffraction (XRD) with Cu Kα radiation and the x-ray tube operating at 45 kV and 40 mA. Before and after corrosion tests, surface and corrosion features of coated samples were examined using an electron microscope with a field emission electron source and by energy dispersive x-ray spectroscopy (EDX) for elemental analysis. The corrosion products could therefore be qualitatively assessed at the pinhole defects.

In electrochemical investigation, solutions of deaerated 0.5 M H_2SO_4 were prepared with 10 N H_2SO_4 (ACS reagent grade) and deionized (DI) water. The systems were purged with N_2 gas (99.999% purity) at a rate of 1.0 L/min for 1 h before an electrochemical test and then continuously purged with the N_2 gas at a rate of 0.5 L/min during the experiment. Electrochemical impedance spectroscopy (EIS) and potentiodynamic polarization measurements were carried out at room temperature (22 ± 3 ^{o}C) using a Gamry PC4/300 computerized system for collecting and analyzing electrochemical data. A flat cell (Princeton Applied Research) was used with a three-electrode configuration including a saturated calomel electrode (SCE) and platinum gird

as reference and auxiliary electrodes, respectively. All electrochemical tests were carried out with an exposure area of 1 cm^2.

EIS data were collected at open circuit potential (OCP) with a sinusoidal voltage perturbation of 10 mV (rms) over the frequency range of 10 mHz to 100 kHz with 7 to 10 points per decade; these spectra were obtained regularly over an exposure period of 5 days. The data were analyzed using complex nonlinear least squares fitting (CNLS) LEVM algorithm [68] in the Gamry Echem Analyst software. Potentiodynamic polarization was measured 1 h after immersion with a scan rate of 10 mV/min from –0.2 to +1.5 V versus OCP.

8.3 Results and Discussions

8.3.1 Phase Identification and Morphology

The electrodeposited (ED) and sputtered (PVD) Cr coatings reveal the same phase as the powder diffraction pattern of Cr (body centered cubic structure): the PVD Cr coating has (110) orientation and is similar to that of the Cr powder diffractogram while the ED Cr coating has (222) orientation with peak broadening, which may be attributed to microstrain and particle size (Figure 8.1). In addition to the long range structure, the short range structure of the Cr coatings was compared to that of the Cr foil by conducting EXAFS analysis. Data reduced to $\chi(k)k^3$ versus photoelectron wavevector, k, (Figure 8.2a) show identical envelopes, where the PVD coating appears to exhibit less disorder due to the greater amplitude of the spectra compared to that for the ED one. The Fourier transforms (FT) of the EXAFS ($\chi(k)k^3$) spectra (Figure 8.2b) over 1.56 to 3.15 Å correspond to the first coordination shell that represents two subshells in the vicinity of

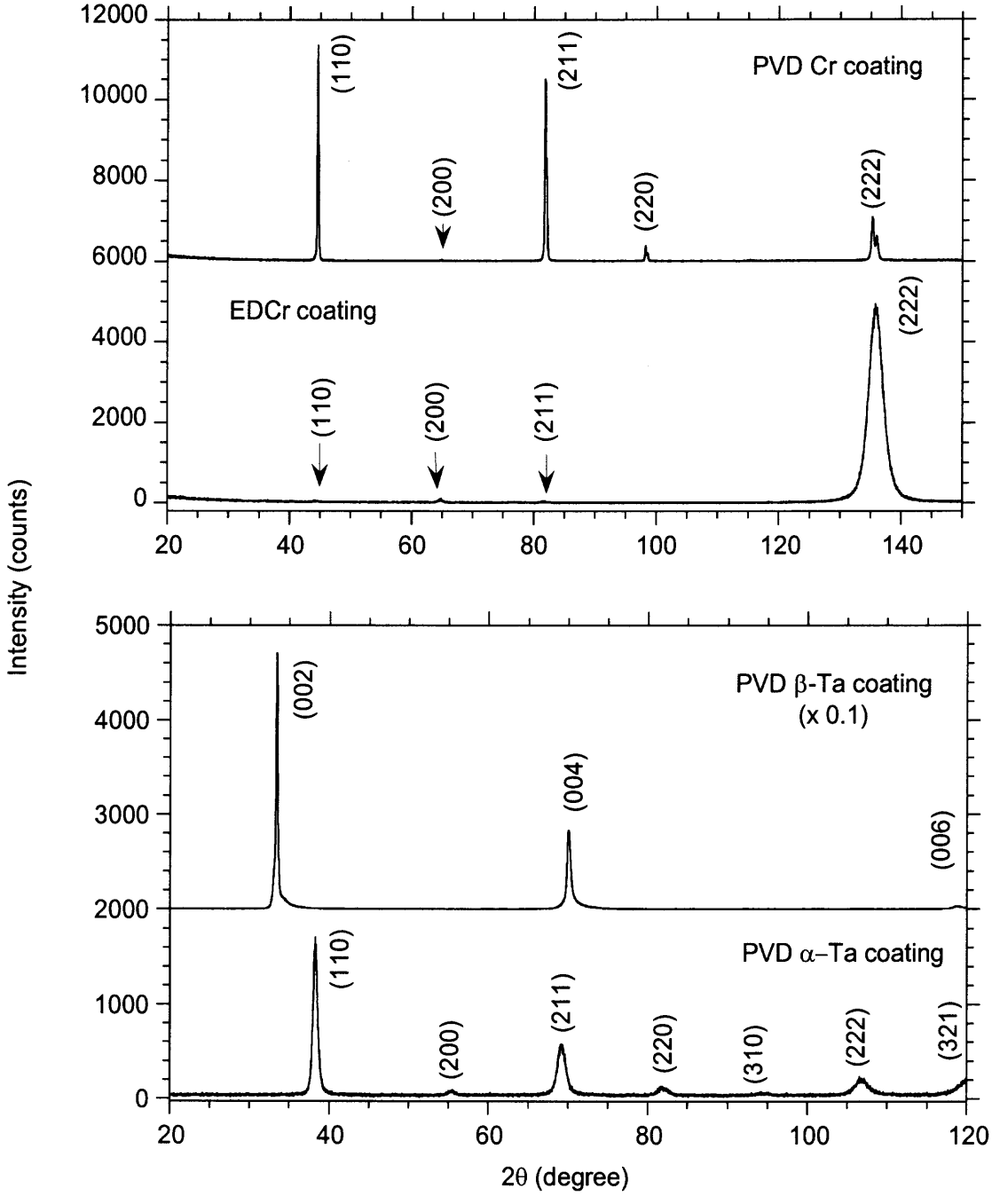

Figure 8.1 X-ray diffraction patterns of electrodeposited Cr and sputtered Cr coatings and sputtered α- and β-Ta coatings.

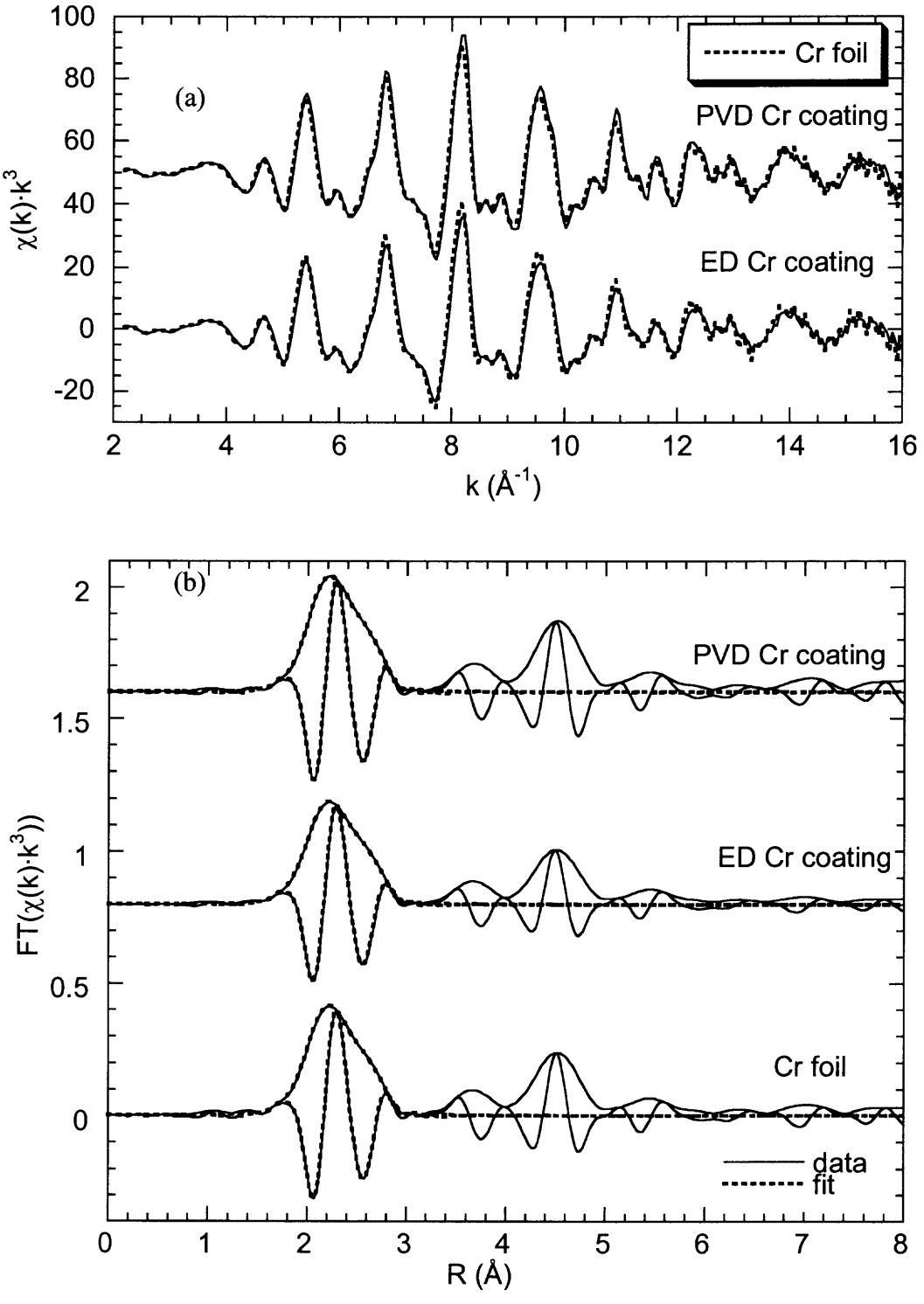

Figure 8.2 (a) Cr *K*-edge $\chi(k)k^3$ spectra of PVD and ED Cr coatings and Cr foil. (b) Fits to Fourier transforms of $\chi(k)k^3$ spectra over the k range 2.4 – 15.7 Å^{-1}.

the absorbing atom. This atomic short-range structure for both coatings is consistent with Cr foil (body centered cubic structure) (Table 8.1) with 8 and 6 Cr atoms at 2.50 and 2.88 Å, respectively. It is interesting to note that the long-range order as well as the short range structure are affected by deposition methods.

The α-Ta coating exhibits a very similar pattern to Ta powder with (110) orientation; the β phase was not observed (Figure 8.1). For the β-Ta coating three peaks (Figure 8.1), referred to as (002), (004), and (006) are observed with no trace of the α phase. In general, β-Ta films exhibit (002) texture [106]. The short-range structure of both Ta coatings was also investigated by EXAFS analysis. The EXAFS [$\chi(k)k^3$] spectra of the coatings reveal unique structures (Figure 8.3a). For the α-Ta coating, the FT of the $\chi(k)k^3$ over 1.7 to 3.05 Å corresponds the first coordination shell (Ta) around the absorbing atom (Figure 8.3b); the atomic short-range structure is consistent with the theoretical EXAFS of α Ta with 8 – 9 Ta atoms at 2.83 Å (Table 8.2). As for β-Ta coating, the broad shell of Ta is positioned between 1.7 and 3.5 Å. Given the structure (tetragonal), space group of $P\bar{4}2_1m$ with 30 atoms per unit cell [119], multiple subshells are present and therefore fitting was not feasible due to the number of parameters required in fitting, exceeding the degrees of freedom. Jiang et al. [11] reported that as β-Ta has a highly disordered local structure, the EXAFS data can not be modeled by a simple cumulant expansion.

A morphological analysis of the ED Cr coating reveals a dense network of microcracks (Figure 8.4a), which may be produced by internal stresses generated during electrodeposition [120]. Cote et al. [118] reported that the surface cracks were generated during deposition and subsequent annealing at 200 °C to remove hydrogen. These cracks

Table 8.1 Results of EXAFS fits* on the first shell for PVD and ED Cr coatings and Cr foil Fourier transformed over 2.4 to 15.7 $Å^{-1}$ k-range and fitted over 1.56 to 3.15 Å r-range.

	PVD Cr coating	ED Cr coating	Cr foil	Cr XRD model
		First subshell (Cr-Cr)		
N**	8.0	8.0	8.0	8.0
R (Å)	2.50 ± 7.5E-4	2.50 ± 9.7E-4	2.50 ± 9.3E-4	2.49
σ^2 ($Å^2$)	0.003931 ± 2.9E-5	0.004796 ± 3.5E-5	0.004332 ± 4.4E-5	0
		Second subshell (Cr-Cr)		
N**	6.0	6.0	6.0	6.0
R (Å)	2.88 ± 9.8E-4	2.88 ± 1.6E-3	2.88 ± 1.5E-3	2.88
σ^2 ($Å^2$)	0.003628 ± 5.3E-5	0.004482 ± 6.3E-5	0.004076 ± 1.12E-4	0

* S_0^2 was set as 0.74 based on fit on Cr foil.

** N was fixed in all fits.

N, R, and σ^2 are coordination number, interatomic distance, and Debye-Waller factor, respectively.

N and R have errors of ± 20% and ± 0.02 Å, respectively.

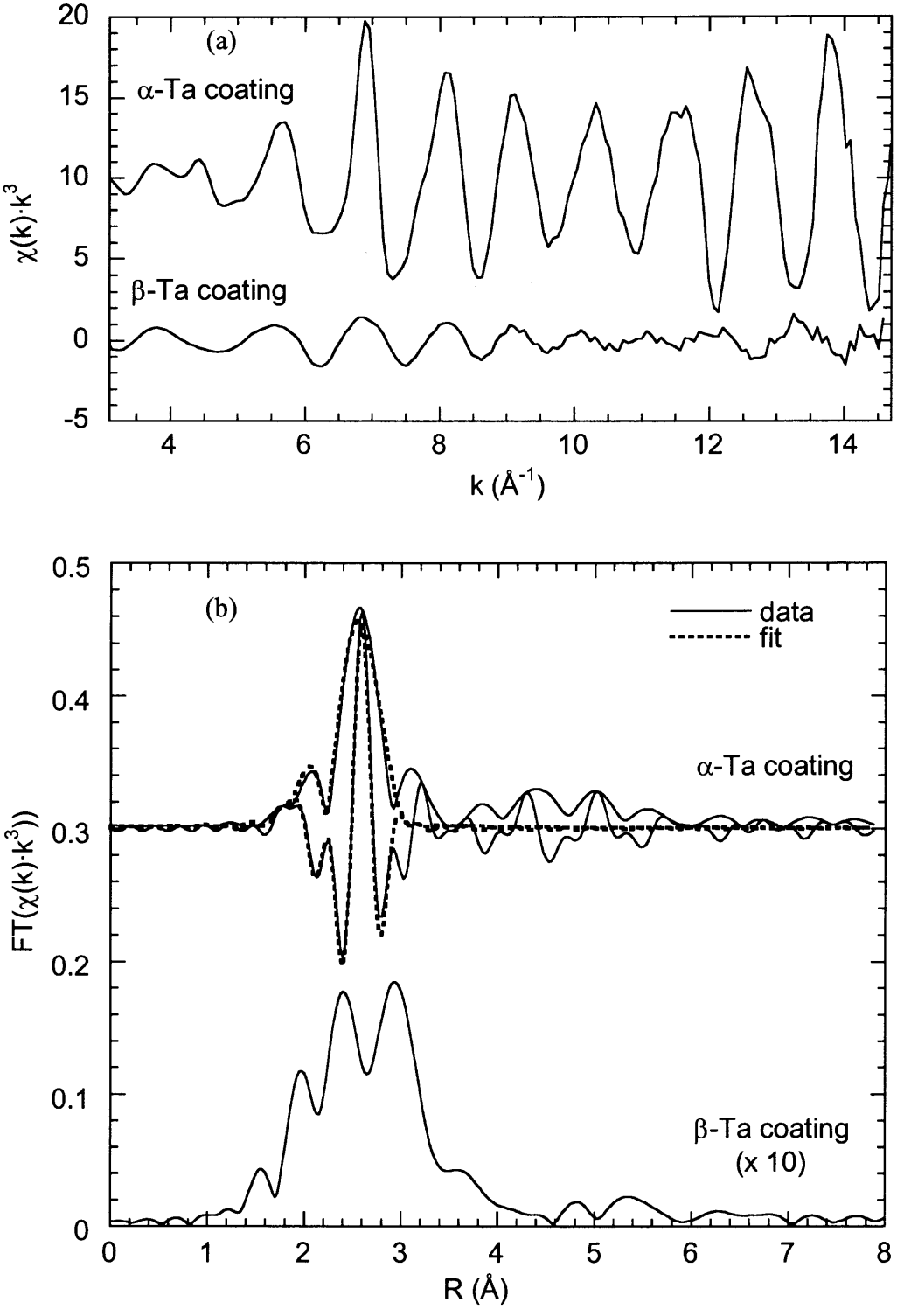

Figure 8.3 Ta L_{III}-edge $\chi(k)k^3$ spectra of PVD α- and β-Ta coatings. (b) Fourier transforms over the k range 3.1 – 15.4 Å^{-1} for α-Ta coating and 3.5 – 14.1 Å^{-1} for β-Ta coating.

Table 8.2 Results of EXAFS fit* on the first shell for α-Ta coating on the steel substrate Fourier transformed over 2.85 to 15.8 $Å^{-1}$ k-range and fitted over 1.70 to 3.05 Å r-range.

	α-Ta coating	α-Ta XRD model
N	8.97	8.00
R (Å)	2.83	2.86
σ^2 ($Å^2$)	0.006731 ± 0.000090	0

N, R, and σ^2 are coordination number, interatomic distance, and Debye-Waller factor, respectively.

* S_0^2 was set as 1.0. N and R have errors of ± 20% and ± 0.02 Å, respectively.

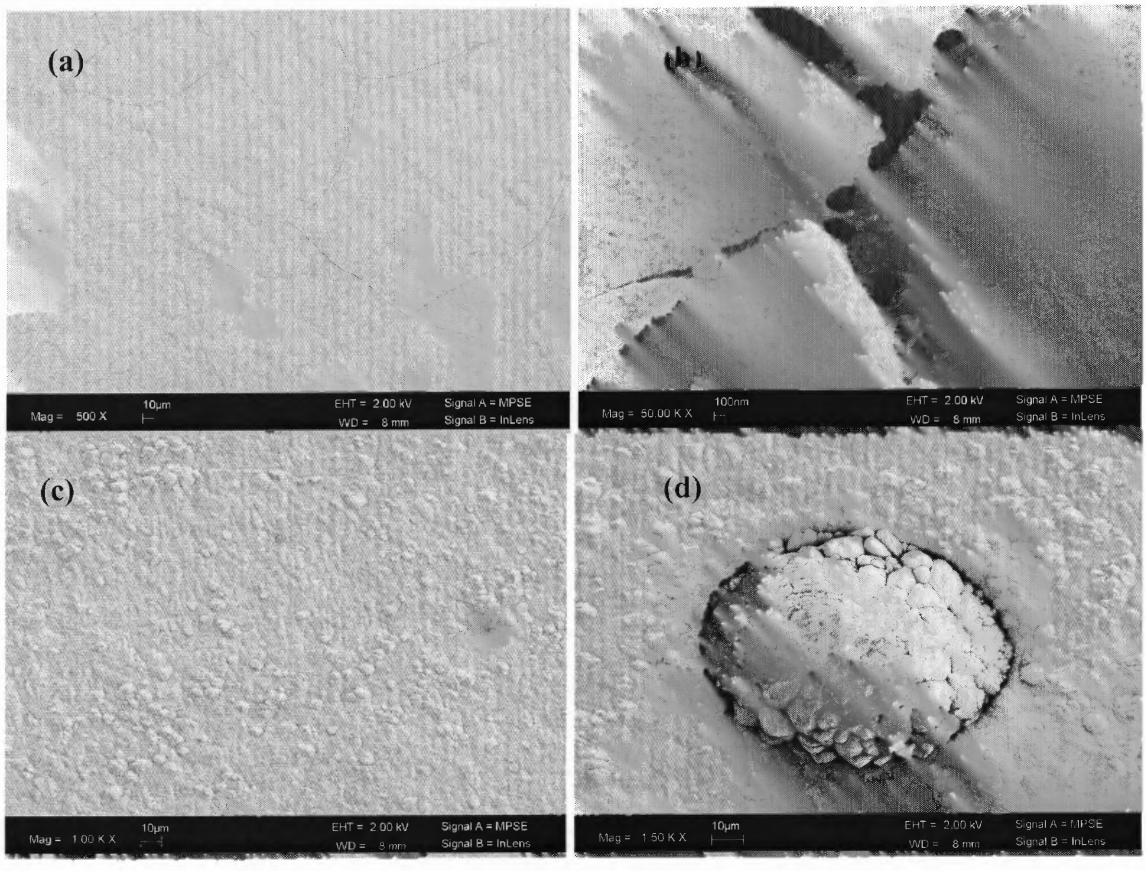

Figure 8.4 SEM images of electrodeposited Cr (a, b) and sputtered Cr (c, d) coatings.

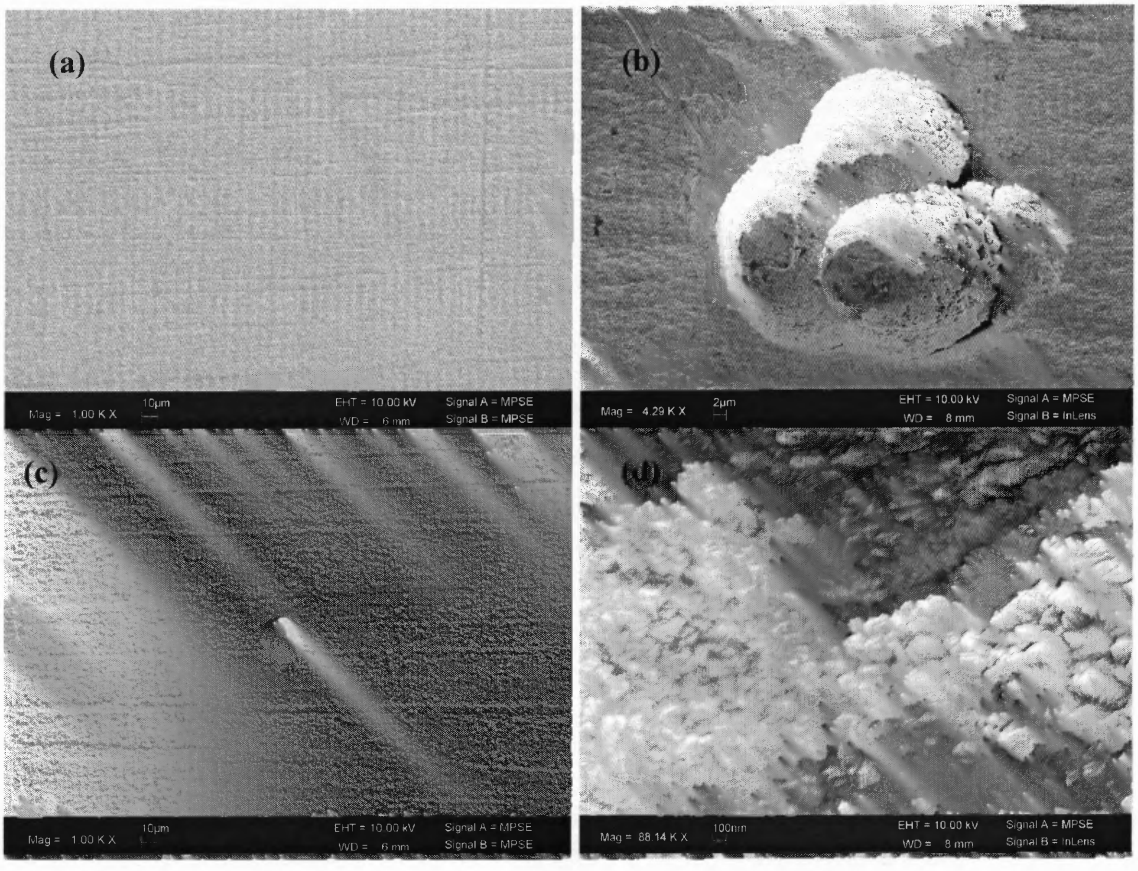

Figure 8.5 SEM images of sputtered α-Ta (a, b) and β-Ta (c, d) coatings.

are thin (< 0.4 μm) as compared to the coating thickness (Figure 8.4b); in addition, they are and observed throughout the deposit. The PVD Cr coating does not exhibit microcracks, however, droplet-like defects (Figure 8.4c) that are commonly found in PVD processes are seen throughout the surface; this feature has been reported by others as well [113, 104-108]. SEM imaging of the α-and β-Ta coatings showed uniform coverage of the steel substrate without cracks (Figure 8.5a and c). Nevertheless, defects such as droplet-like clusters and pinholes (Figure 8.5b and d) were observed, but not to the same degree as that found with the PVD Cr coating (Figure 8.4c). Defects in the form of open pores or voids extending from the coating surface to the substrate are of the

greatest concern as they provide channels for electrolyte penetration to the steel substrate, initiating localized corrosion that significantly influences the corrosion resistance of coatings.

8.3.2 Corrosion Behavior of as Function of Immersion Time Evaluated by EIS

The impedance spectra of the α- and β-Ta coatings collected over 5 days at OCP are shown in Figure 8.6. The development of two time constants in the phase angle was observed for both coatings after 24 hours of exposure. This effect was accompanied by a continuous and slight decrease in the absolute values of impedance. In general, tantalum exhibits consistent and stable impedance behavior with one time constant over long exposure times due to the very stable and dense tantalum oxide passive film [23]. Therefore, the presence of two time constants is attributed to the dissolution of steel substrate at open pores. The short relaxation time constant, associated with a high-frequency process is related to the coating/solution interface and the dielectric characteristic of the native oxide film, whereas the low-frequency process is associated with the substrate/solution interface through open pores.

For the Ta coatings, the equivalent circuit model (Figure 8.7) representing localized corrosion of the steel substrate exposed to the electrolyte through permeable defects in the coating was applied to fit the EIS data for the Ta coatings. The parallel connection of R_{ps} and C_s is representative of the electrical charge transfer process at the steel substrate/coating interface through open pores and represents the polarization resistance of the steel substrate and the capacitance of the electrical double layer at the electrolyte-steel substrate interface, respectively. R_{po} in series with R_{ps} and C_s is the pore

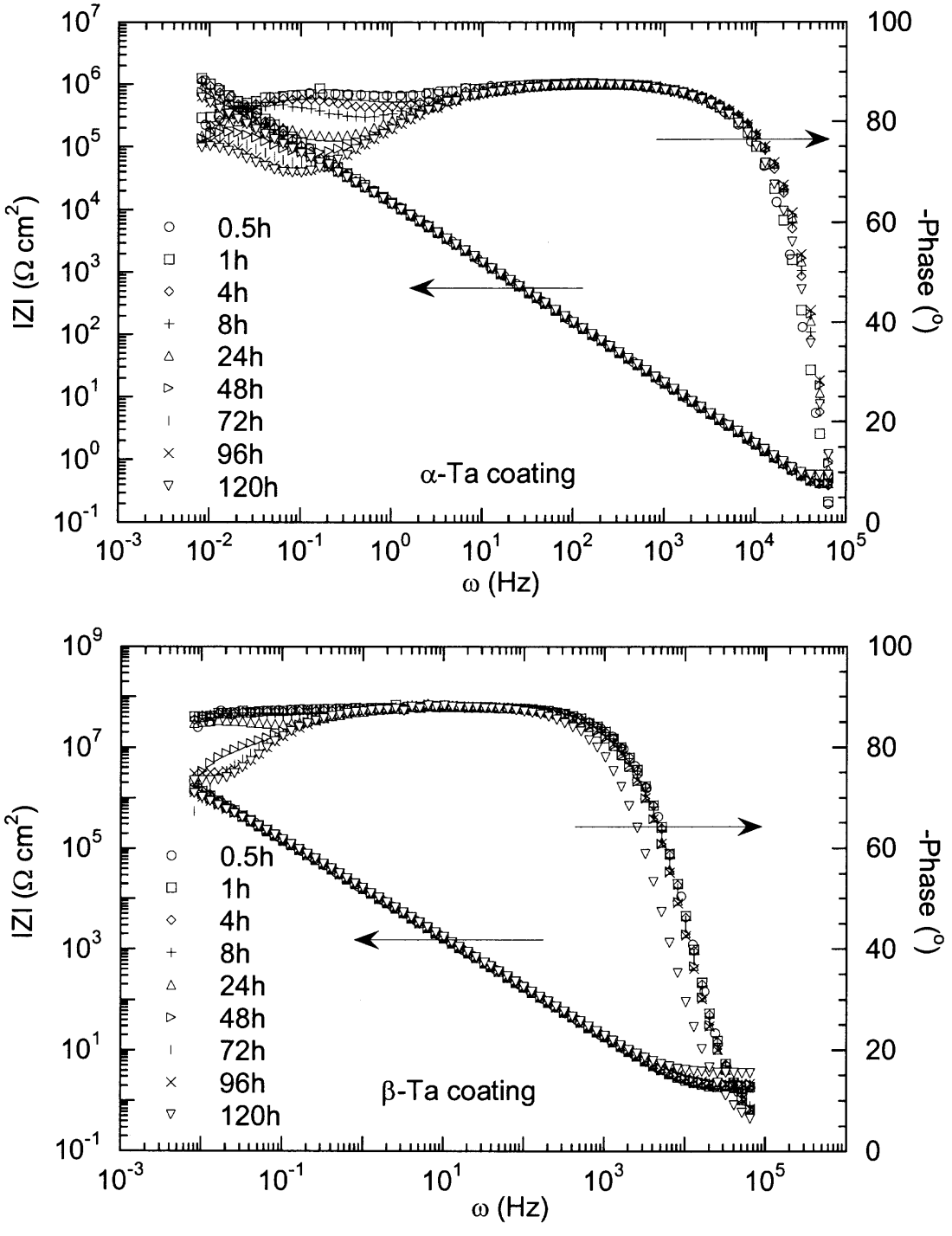

Figure 8.6 Impedance spectra of sputtered α-Ta and β-Ta coatings for different immersion time in deaerated 0.5 M H_2SO_4 with N_2 at room temperature.

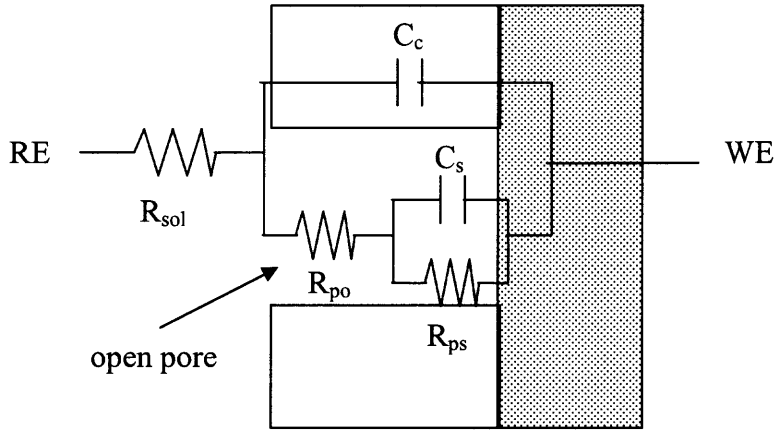

Figure 8.7 Equivalent circuit model for fitting experimental EIS data of α-Ta and β-Ta coatings. (RE and WE are reference and working electrodes, respectively. R_{sol}: solution resistance, R_{po}: pore resistance, R_{ps}: polarization resistance of steel substrate, C_s: electrical double layer capacitance at steel/electrolyte interface, C_c: coating capacitance).

resistance to the ionic current and provides information on degradation of the coating [58]:

$$R_{po} = \frac{\rho L}{PA} \tag{8.1}$$

where ρ is the resistivity of electrolyte in pores, L is average pore length and equivalent to the coating thickness, and A is the surface area exposed to electrolyte, and P is the porosity of the coating, that is the pore area per total exposed area. The circuit parameters obtained from EIS fitting are plotted as a function of time in Figure 8.8. Both coatings show an increase in R_{po} at initial exposure; R_{po} of the α-Ta coating remains constant after 24 h, while for the β-Ta coating it shows a continuous increase. This increase in R_{po} appears to be due to blocking of pores, especially very fine ones from corrosion products

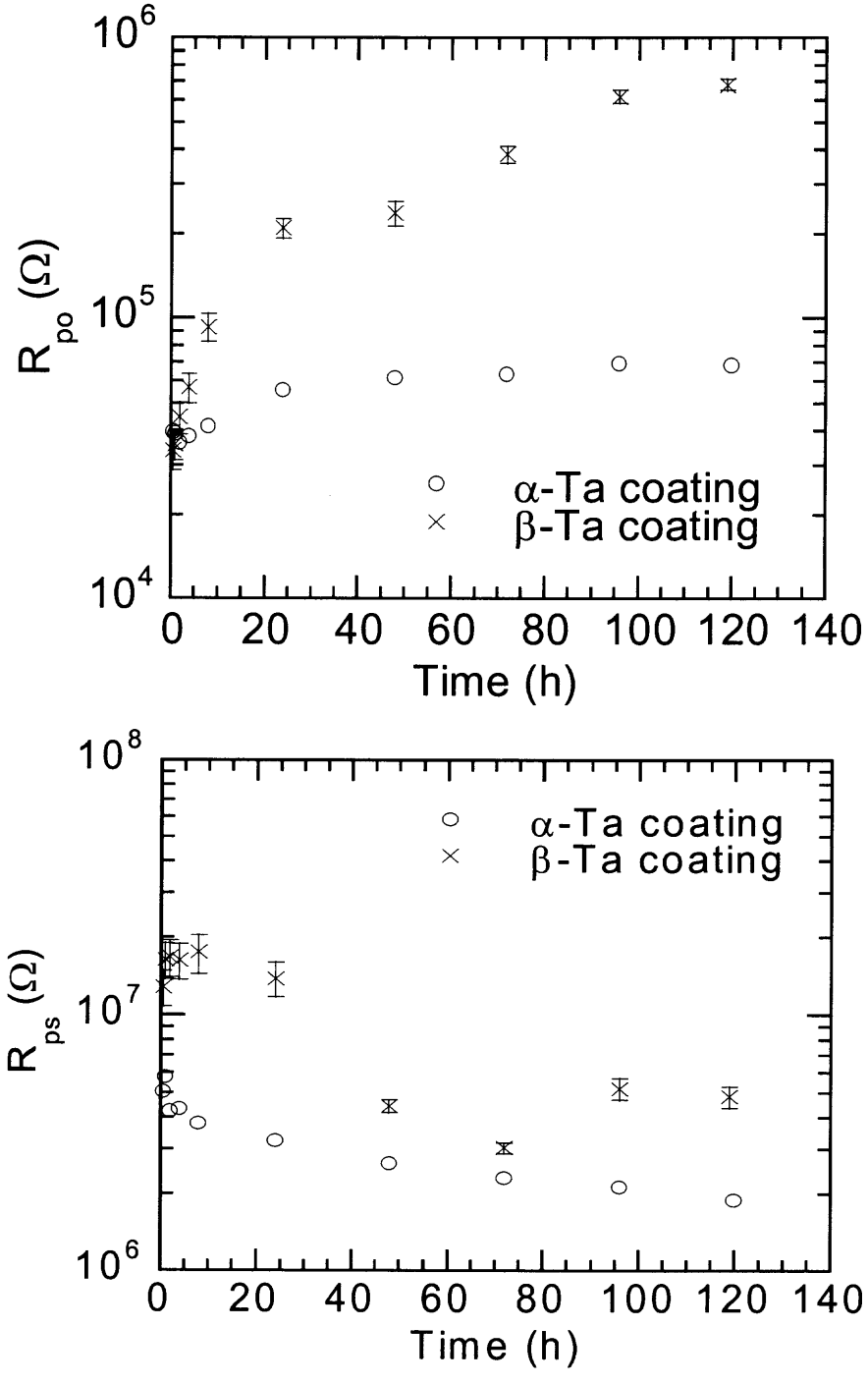

Figure 8.8 The evolution of fitted parameters of the equivalent circuit for α-Ta and β-Ta coatings. Error bars not visible are present within symbol.

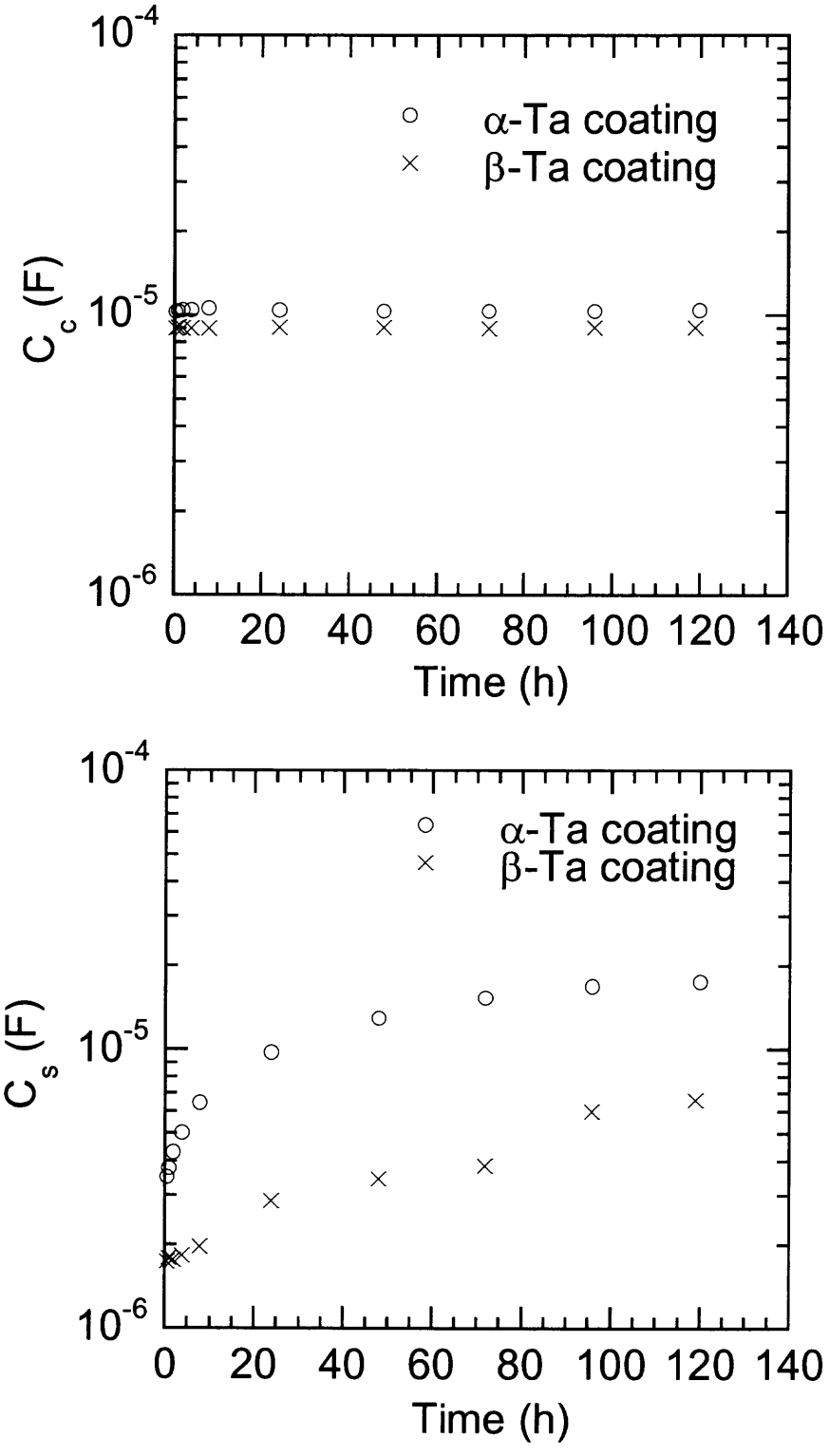

Figure 8.8 (Continued)

along pore surface, decreasing in porosity. Therefore, the β-Ta coating may have finer pores than the α-Ta coating. In contrast to R_{po}, both coatings exhibit a reduction in R_{ps}, suggesting continuous dissolution of the steel substrate through open pores, yet the dissolution rate overall is insignificant over the course of the experiment. The slight increase in Rps for the β-Ta coating after 72 h of exposure may be due to the passivation of the steel substrate through open pores. In association with the behavior of R_{ps}, the increase in C_s demonstrates an increase in the corroding area at the steel substrate/coating interface. Additionally, using SEM, the surface morphology of both coatings was not observed to change over long exposure time and hence the coating capacitance (C_c) was constant, indicating a lack of degradation of the coating. These results reveal that the corrosion process for Ta coatings is dominated by dissolution of the steel substrate through open pores. Therefore, the corrosion resistance of α- and β-Ta coated steels is highly dependent on the presence of open pores. In the previous study, we found that for α-Ta coatings greater than 50 μm, a viable coating was produced where through-pores were insignificant; the impedance behavior was consistent with Ta foil. While the α-Ta coating evaluated in this current work is less than 50 μm, the β-Ta coating is approximately 50 μm. Interestingly, this thicker coating exhibited finer pores, however, the structure and properties are significantly different from the α, potentially contributing to the coating behavior, localized corrosion.

The corrosion behavior of the electrodeposited (ED) and sputtered (PVD) Cr coatings was also studied using EIS (Figure 8.9). The impedance of the ED Cr coating decreases dramatically, reaching the lowest magnitude after 2 h exposure, whereas the

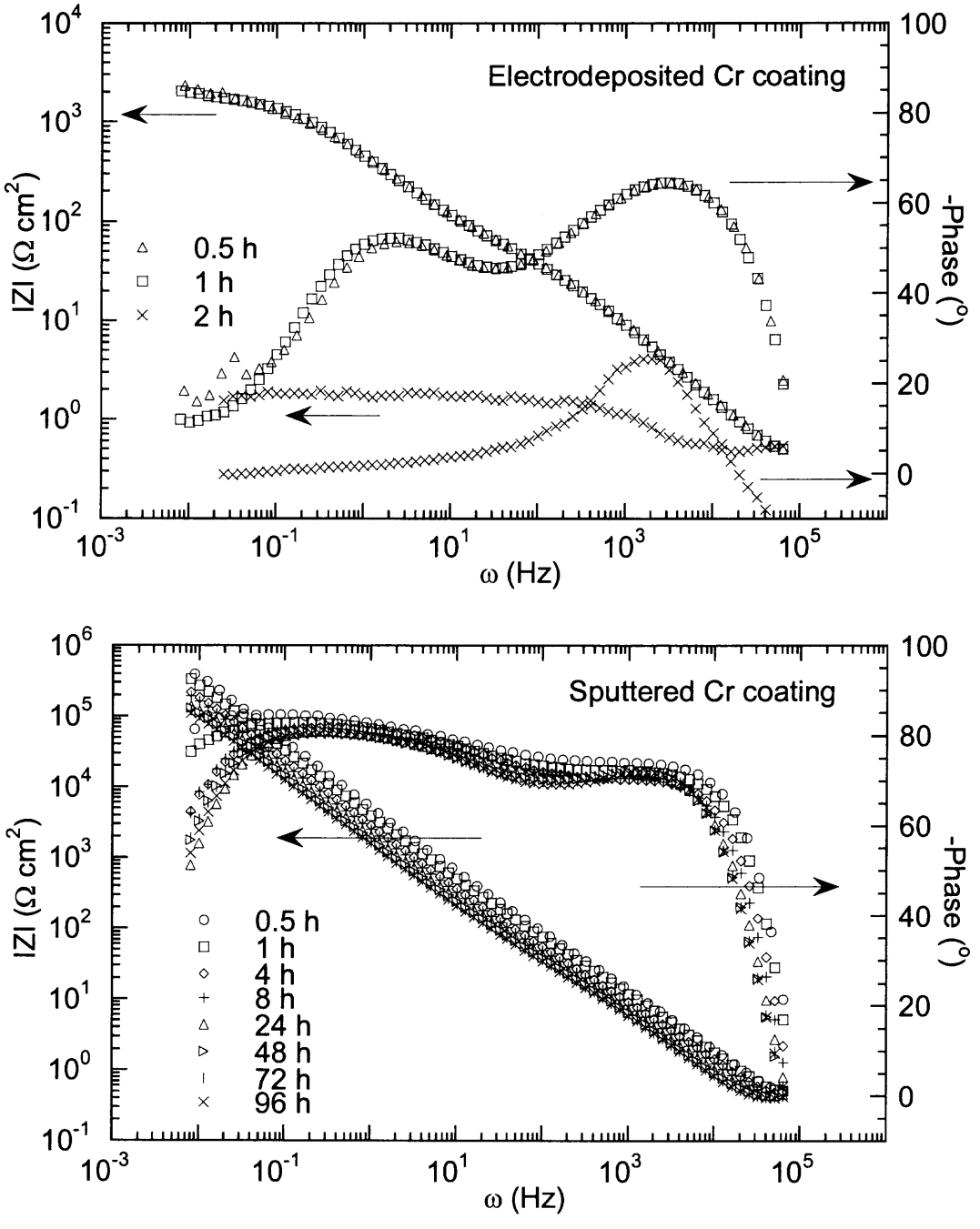

Figure 8.9 Impedance spectra of electrodeposited Cr and sputtered Cr coatings for different immersion time in deaerated 0.5 M H_2SO_4 with N_2 at room temperature.

PVD Cr coating shows a gradual decrease in the impedance, but maintains high impedance over long exposure. In the initial phase angle response, two time constants were observed in both coatings. However, the ED Cr coating showed the transition to one time constant at 2 h, while two time constants were still seen for the sputtered Cr up to 120 h of exposure. Cheng et al. [121] reported a transition in phase angle response from one time constant to two as potential increased from the active dissolution region to the passivation region for pure Cr. Therefore, the presence of two time constants in the Cr coatings may be attributed to the pre-existing Cr passive film and/or any potential open pores as shown in the Ta coatings.

The passive film formed on Cr, reported as Cr_2O_3 [122], is not stable at pH less than 1 over the potential range of -1.2 to 2.2 V and hence, undergoes dissolution [20, 122]. The OCP decayed with immersion time to more active values, resulting from dissolution. This decay was observed in both Cr coatings over the course of the experiment; for the ED Cr coating, from -438 to -732 mV (vs. SCE) at which the pure Cr foil corrosion potential was reported by Wilde and Hodge [123], and for the PVD Cr coating, from 75 to -290 mV (vs. SCE), where the pure Cr foil still undergoes passivation.

Subsequent evaluation of the surface morphology of the ED Cr coating revealed severe attack, where dissolution was initiated at the microcracks (Figure 8.10a and b). However, the PVD Cr coating does not reveal any effect of corrosion (Figure 8.10c). Elemental analysis using EDX only confirmed the presence of Cr; however, for coatings of such thickness, detecting the substrate even through μm size cracks would be very difficult (as EDX has a sampling depth of 1-2 μm). Therefore, potentiodynamic

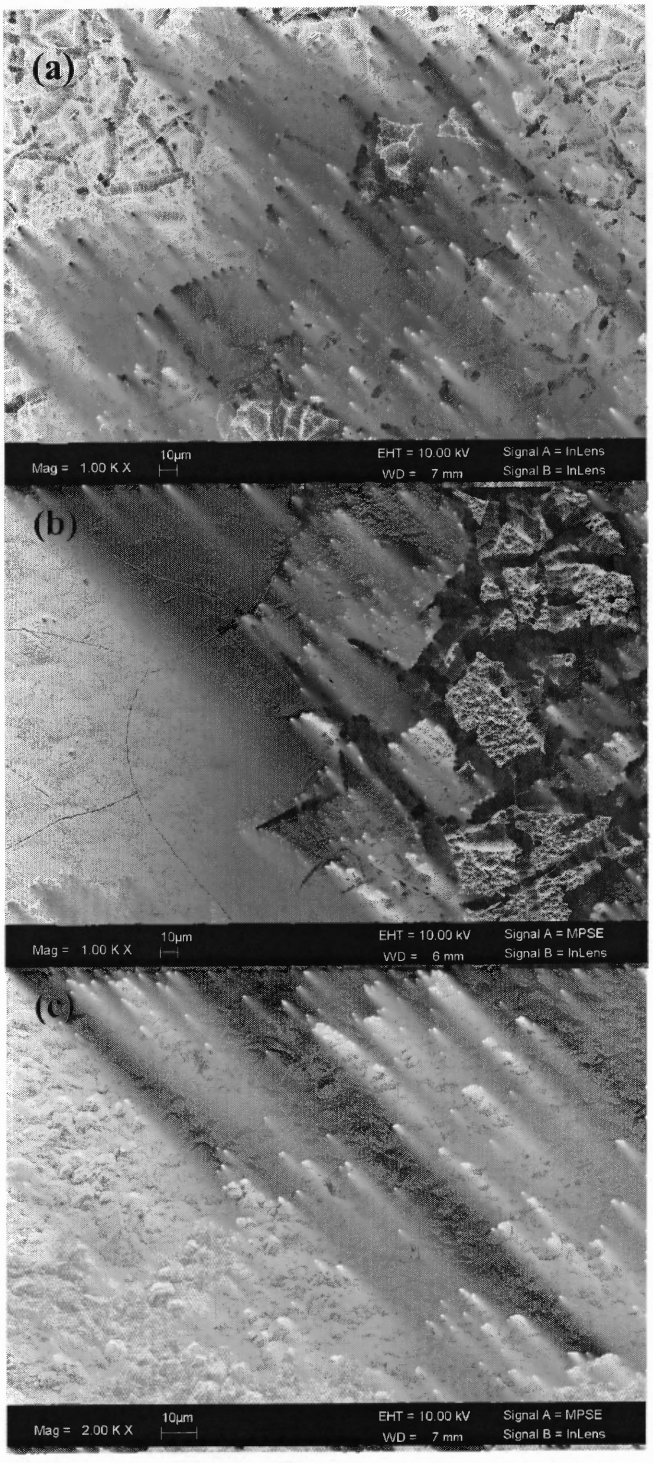

Figure 8.10 SEM images of electrodeposited Cr (a, b) and sputtered Cr (c) coatings after EIS measurement.

polarization was conducted to further assess the effect of open pores at 1 h after immersion by applying potential from -0.2 to 1.5 V (vs. SCE) from OCP.

8.3.3 Anodic Polarization Behavior of Cr Coatings

The polarization curves for the ED and PVD Cr coatings are shown along with the steel substrate in Figure 8.11. The behavior of the ED Cr coating is consistent with that of pure Cr foil in deaerated 0.5 M H_2SO_4 [122], showing two stable mixed potentials for the reduction of H^+ to H_2; its corrosion potential was measured at -660 mV (vs. SCE), which

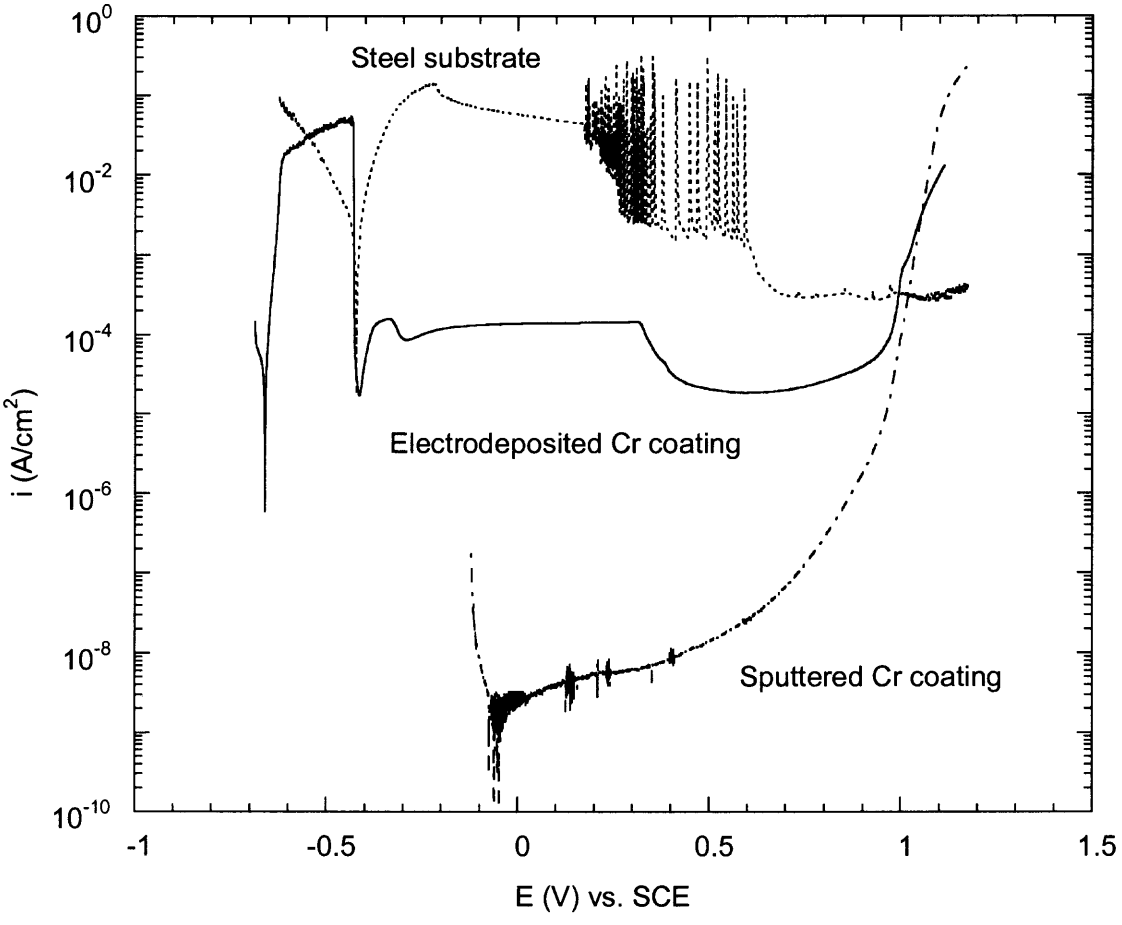

Figure 8.11 Anodic polarization curves of electrodeposited Cr and sputtered Cr coatings and the steel substrate (ASTM A723) after 1 h immersion in 0.5 M H_2SO_4 deaerated with N_2 at room temperature.

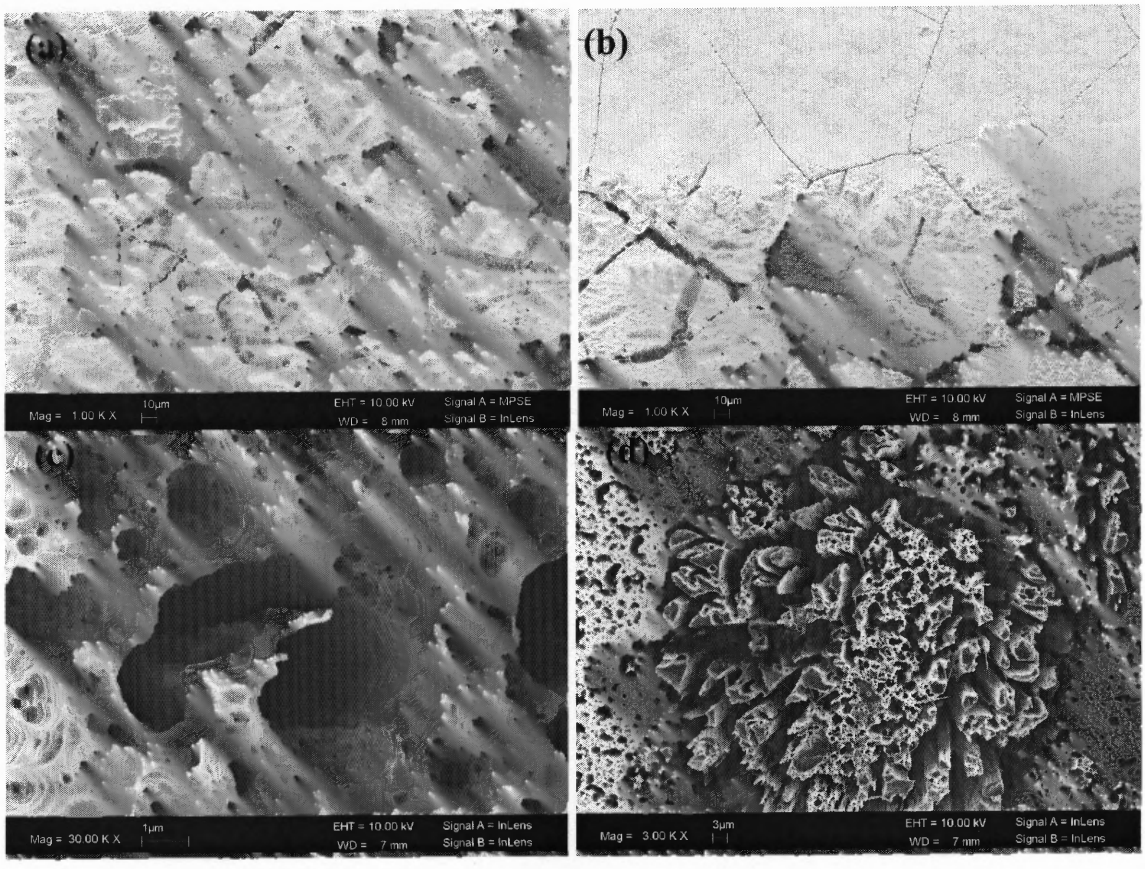

Figure 8.12 SEM images of electrodeposited Cr (a, b) and sputtered Cr (c, d) coatings after potentiodynamic polarization measurement.

is slightly greater than that of pure Cr (-703 mV), indicating that the coating underwent active dissolution at open circuit potential. However, the PVD Cr coating, of which the corrosion potential was approximately -75 mV (vs. SCE), exhibits a more noble behavior than the ED Cr coating. Additionally, the corrosion current density of the former is four orders of magnitude lower than the latter. This result demonstrates that the PVD Cr

coating is more corrosion resistant than the ED coating, potentially due to the passive oxide film.

Both Cr coatings show a similar transpassivation behavior to pure Cr, representing oxidation of the passive film and high dissolution of Cr species [124]. As the applied potential draws near the transpassivation region (> approx. 0.9 mV vs. SCE), the current density of the PVD Cr coating gradually increases, approaching that of the ED Cr coating. Interestingly, the current density of the PVD Cr coating becomes greater than that of the ED one beyond 1.05 V (vs. SCE). This result appears to be caused by the widespread droplet-like defects in the PVD Cr coatings, of which boundaries potentially provide more surface activity than that for the ED one. The surface morphology of the corroded ED Cr coating (Figure 8.12a and b) is consistent with that observed at the free corrosion potential (Figure 8.10a and b), showing microcracks are more severely attacked than other regions. In contrast, the PVD Cr coating exhibited a significant change in surface morphology; the surface became porous after dissolution of Cr coating (Figure 8.12c) and the droplet-like defects appear to be highly attacked (Figure 8.12d). It is worth noting that at the transpassivation region of Cr coatings, the steel substrate is under passivation and hence corrosion products from substrate dissolution/oxidation at open pores should be observable by EDX for thinner Cr coating (< ~3 μm). However, substrate dissolution even on the severely attacked regions was not confirmed. In association with EIS, these results potentially suggest a lack of presence of open pores in the Cr coatings with thicknesses greater than 100 μm, indicating that the corrosion process may be dominated by the depassivation of the oxide film and dissolution of Cr species.

8.4 Summary

The corrosion behavior of the PVD and ED coatings was studied at open circuit potential using EIS. For Ta coatings, the corrosion process was dominated by dissolution of the steel substrate through open pores, however, at the end of 5 d, coating degradation was not observed. In contrast, open pores were not observed with the ED and PVD Cr coatings. Yet a continuous decrease in the corrosion resistance was observed for the Cr coatings under acidic conditions, as a result of the protective oxide dissolution. In addition, the PVD Cr coating exhibited improved corrosion resistance over the ED one, which may be due to surface structure of the oxide film. Similarly, the polarization behavior of the ED Cr coating was consistent with pure Cr, while the PVD one again showed improved corrosion performance. Both Cr coatings exhibited similar transpassive behavior to that of pure Cr; the current density of the PVD Cr coating was observed to be greater than that of the ED one in the transpassive region, and again this may be attributed to the surface microstructure of the extensive droplet-like defects. Overall, the α-Ta coatings with thickness greater than 50 μm is superior to the Cr coatings with respect to corrosion performance because of the stable Ta oxide as a passive film. In the next chapter, the passive Ta oxide films were investigated comparing thermal and anodic Ta oxide films

CHAPTER 9

AN INVESTIGATION ON STRUCTURES OF THERMAL AND ANODIC TANTALUM OXIDE FILMS

9.1 Introduction

High temperature and anodic tantalum oxide films have been studied extensively in the field of corrosion [33, 125]. Ta possesses a high melting point (2996 °C), is highly ductile, and is corrosion resistant in aggressive environments [126]. The low thermal expansion and the predictability of tantalum oxidation are additional characteristics that make tantalum attractive for high temperature applications. In addition, with a dielectric constant greater than 20, tantalum pentoxide (Ta_2O_5) has received significant attention in the semiconductor industry [25]. Although Ta itself is highly reactive, the stable, dense nanometer oxide film formed provides an effective barrier to corrosive environments.

Thermodynamically, tantalum pentoxide (Ta_2O_5) is the only stable high temperature oxidation product [125]. However, thin films of Ta_2O_5 have several different structures depending on the system temperature [32, 127, 128, 130, 131]. The principal structures of crystalline Ta_2O_5 are orthorhombic (α and β phases) [99-101] and hexagonal (δ phase) [32, 131]. Fukumoto and Miwa [131] reported that the hexagonal structure of Ta_2O_5 has the space group of *P6/mmm* with lattice constants of a = 7.191 Å and c = 3.831 Å and eight oxygen atoms in the first shell. The orthorhombic structure occurs in two forms with a reversible transition reported at approximately 1360 °C [127-129]: the high temperature α-phase (H-Ta_2O_5) and the low temperature β-phase (L-Ta_2O_5). A recent study [129] on the low temperature oxide showed that β-Ta_2O_5 has unit-

cell parameters of a = 6.217 Å, b = 3.677 Å, and c = 7.794 Å with the space group of *Pccm*. Voltovich et al. [132] reported that over the temperature range of 600 to 1000 °C β-Ta_2O_5 was produced. However, the formation of metastable tantalum oxide phases occurs between 300 and 800 °C [133]. Steeb and Renner [134] found that at approximately 400 °C, platelets of metastable metallic oxide phases are nucleated and grown. These suboxides include TaO_x, TaO_y, and TaO_z comprising Ta_6O, Ta_4O, and Ta_2O, respectively. Between 600 and 800 °C, TaO_z is the dominant intermediate oxide, while above 800 °C, the thermodynamically stable β-Ta_2O_5 is formed directly from Ta-O solid solution [125, 132]. In contrast to the high temperature tantalum oxide, the anodic oxide has been observed to be amorphous. Kerrec et al. [23] reported that when anodically grown in 0.5 M H_2SO_4 at 25 °C, the oxide is comprised for the most of Ta_2O_5 and TaO_x sub-oxide, the latter of which is present initially before oxidation. They found that as the thickness of anodic oxide increases, Ta_2O_5 increases and is dominant.

To better understand the nature and growth of protective Ta oxide films, extended x-ray absorption fine structure (EXAFS) spectroscopy was applied to investigate the short-range structure of both the thermal and anodic oxide films. In addition to EXAFS, x-ray diffraction, scanning electron microscopy, and atomic force microscopy were utilized for identifying crystallographic phases and morphological and topographical features.

9.2 Experimental Methods

Polycrystalline Ta_2O_5 powder (99.85%, Alfa Aesar) was used as a reference specimen.

Ta disks (99.9%) with a diameter of 15 mm were mechanically polished using an alumina suspension (with particle size down to 0.05 μm). The Ta specimens were thermally oxidized in 1 atm O_2 at 800 °C for 1 hr, 400 °C for 30 min, and 400 °C for 3 hrs. These temperatures fall into the range where metastable oxides are formed; additionally, they represent temperatures employed in the semicondotor industry [25, 135] and therefore understanding the nanometer oxide films formed are critical to predicting performance. To obtain the anodic oxide films used as dielectrics [23, 25], a constant current density, i=0.7 mA/cm^2 was applied in deaerated 0.5 M H_2SO_4 at room temperature using galvanostatic control mode in EG&G (Princeton Applied Research) model 273A. The exposure area was 1 cm^2; the immersion times were 100, 200, 500 and 600 seconds; and the corresponding total charge, which passed during anodic oxidation, was 73, 144, 367 and 422 mC.

Crystallographic phase identification was accomplished using conventional x-ray diffraction (XRD) with Cu Kα radiation and the x-ray tube operating at 45 kV and 40 mA. Morphological and topographical features of thermal and anodic oxide films were examined using field emission scanning electron microscopy (FE-SEM) and atomic force microscopy (AFM) in contact mode.

To obtain the local structural information, EXAFS experiments were carried out at the Ta L_{III} edge (E_0 9881 eV) on beamline X11A at the National Synchrotron Light Source (NSLS), Brookhaven National Laboratory. The storage ring energy operated at 2.80 GeV with an average current of 180 mA. A Si (111) double-crystal monochromator was used for energy selection, and the second Si crystal was detuned to approximately 80% of maximum transmitted x-ray intensity to minimize the presence of higher

harmonics in the beam. Data were collected over the energy range of 9.732 – 10.986 keV after calibration using a tantalum foil. To investigate thermal effects, spectra of the β-Ta_2O_5 reference powder were measured at 77 K and 298 K. For the thermal oxide film produced at 800 °C, fluorescence data were collected with a Lytle detector filled with Ar gas. Ta oxide films formed at 400 °C (30 min and 3 hr) and anodically were investigated with total electron yield (TEY) because of its surface sensitivity [136]; helium gas was utilized in acquisition of spectra to minimize the absorption of x-rays within the TEY detector. Data analysis and fitting were accomplished using standard procedures [96] with WinXAS software [137]. Structural information obtained includes the coordination number (N), the bond length (R), and the mean square variation in distances (σ^2). The model, β-Ta_2O_5 [128], for fitting was generated using FEFF7 [138, 139].

9.3 Results and Discussion

XRD patterns (Figure 9.1) of the Ta oxide film produced at 800 °C and the Ta_2O_5 reference powder are consistent with β-Ta_2O_5 [129], which is an orthorhombic structure with the designation of "*L*-Ta_2O_5" (low-temperature polymorph of Ta_2O_5) [140]. An analysis of peaks with relative intensities greater than or equal to 50% indicates that the structure of Ta oxide at 800 °C is less crystalline than the Ta_2O_5 powder. At 800 °C, a thick white oxide layer is formed; in contrast, oxide formation through thermal oxidation at 400 °C and anodic oxidation is apparently unique. Ta oxide films formed at a lower temperature (400 °C) show that TaO_x (Figure 9.1) is a dominant species among TaO_x, TaO_y and $TaO_{z,}$, which are metastable Ta oxides formed above about 300 to 400 °C

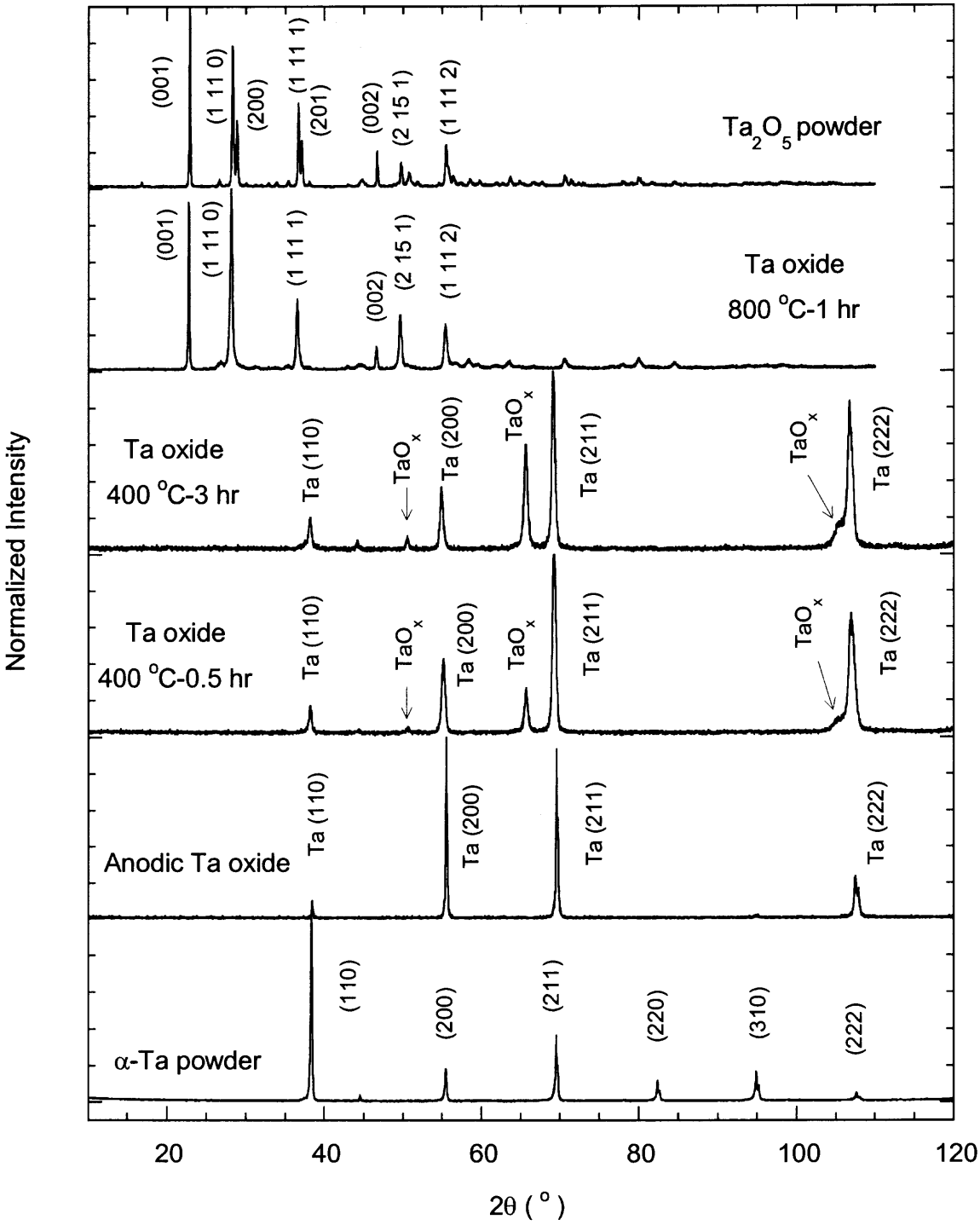

Figure 9.1 X-ray diffraction patterns of Ta_2O_5 powder; thermal Ta oxide at 800 °C for 1 hr, 400 °C for 3 hr and 0.5 hr; anodic Ta oxide; and α-Ta powder.

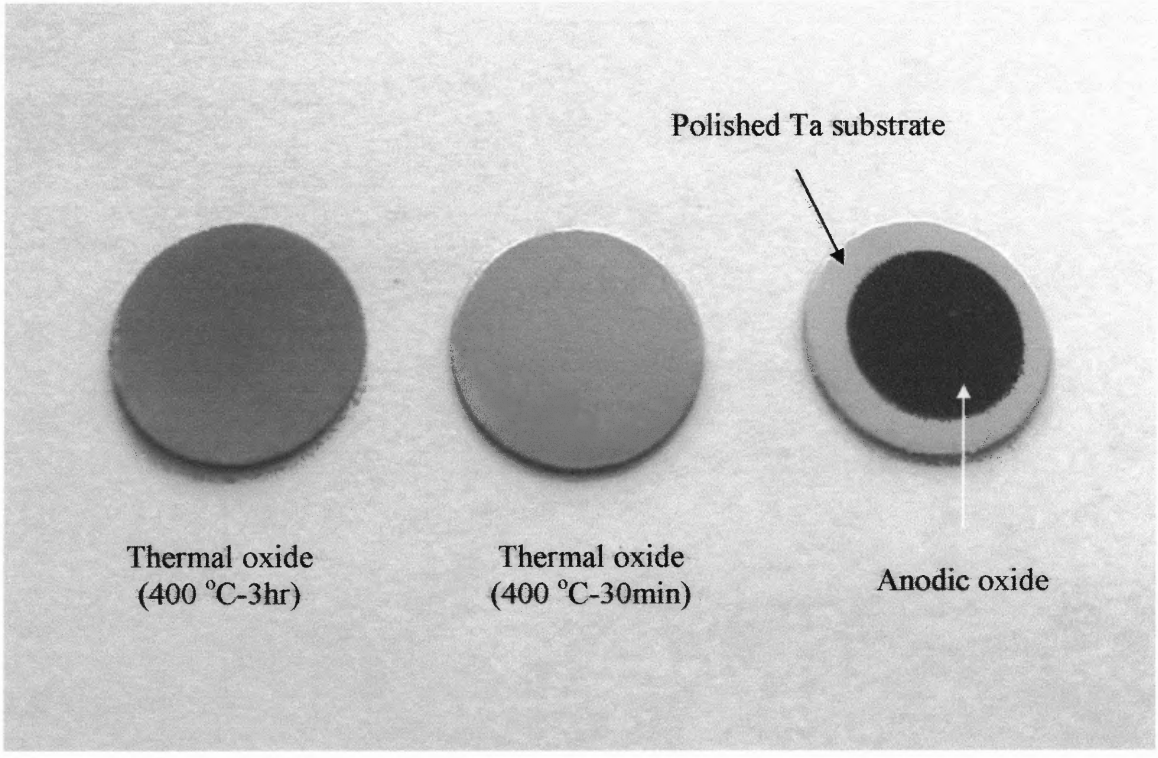

Figure 9.2 Optical image of thermally and anodically oxidized Ta foil.

[134]. Other peaks reveal Ta (110), (200), (211), and (222) planes from the bcc substrate. In addition, consistency of XRD patterns between 30 min and 3 hr is observed, suggesting no time dependence on thermal oxidation at 400 °C. This oxide as well as anodic oxide films changes from brown to blue with increasing exposure time (Figure 9.2). The interference color is characteristic of Ta oxide films and changes with its thickness [33, 141, 142]. Unlike thermal oxides, the XRD pattern of the anodic oxide film shows no indication of long-range or crystalline structure. In general, these anodic oxide films are known to be compact and amorphous [33]. SEM measurements were collected to better understand surface characteristics of the oxides.

The difference in the morphology of oxide layers formed can be seen with the FE-SEM (Figure 9.3). In contrast to the powder-like morphology of the thermal oxide layer

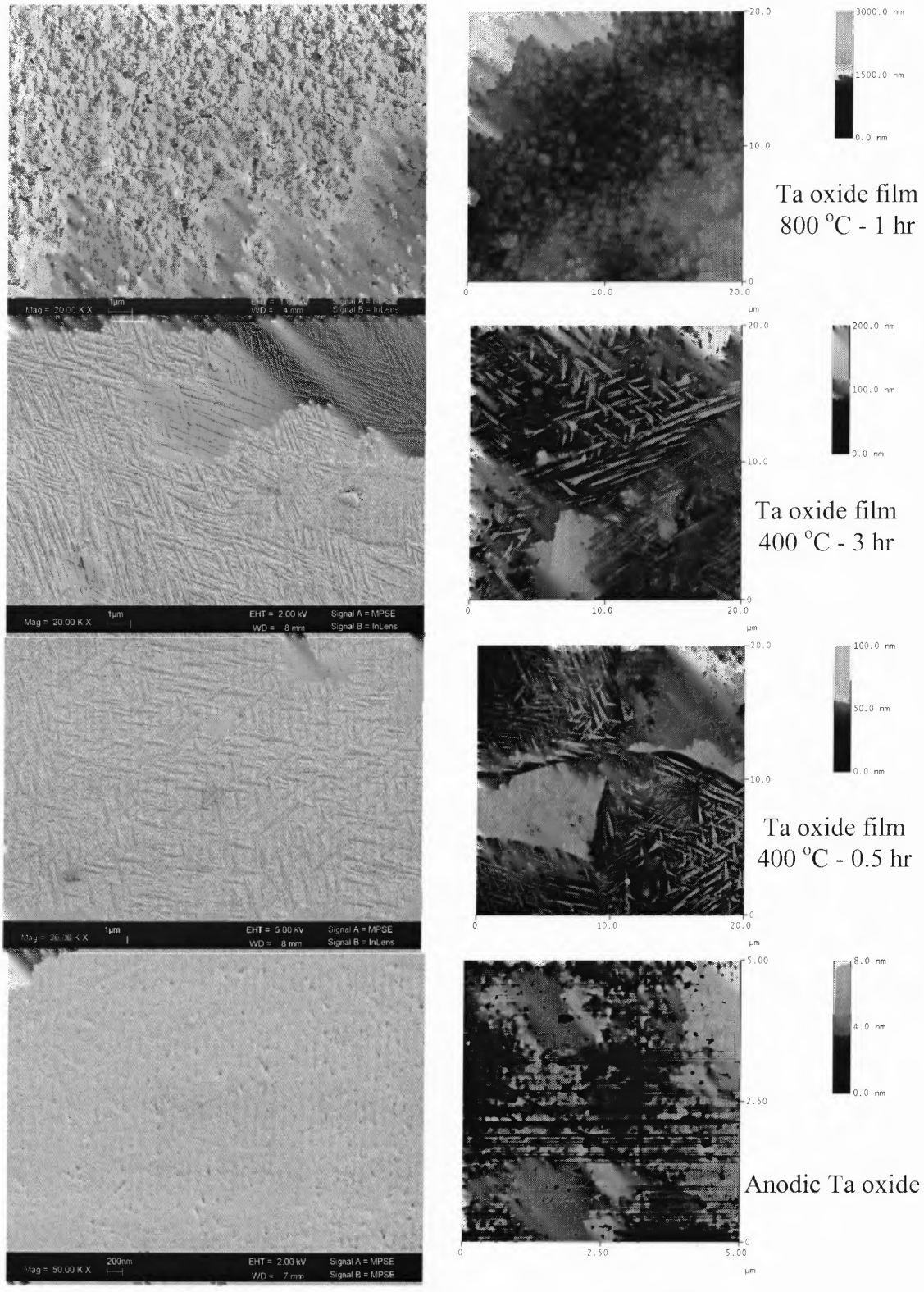

Figure 9.3 SEM (left side) and AFM (right side) images of thermal Ta oxides at 800 °C for 1 hr and 400 °C for 3 and 0.5 hr and anodic Ta oxide.

formed at 800 °C, the oxide films formed at 400 °C reveal platelets of the metastable metallic oxide phase [133]. While no particular morphological change after anodic oxidation was observed compared to the polished Ta disk, variation was observed in roughness (Figure 9.3). The polished Ta disk exhibited an initial roughness of about 5 nm (RMS), at 400 °C roughness varied from about 11 nm (RMS) to 20 nm (RMS) increasing with exposure time. However, the surface morphology of the samples was invariant. The roughness (7 nm, RMS) observed on the anodically oxidized sample was not significantly different from that of the polished Ta disk. Because of its thickness and structure, the morphology and roughness of the 800 °C oxide is not unlike that of the β-Ta_2O_5 reference powder. Further assessment of the exact phases present was performed with x-ray absorption measurements.

Not surprisingly, the 800 °C oxide shows strong oscillations at low k owing to the backscattering of an oxygen shell and is consistent with that of the β-Ta_2O_5 powder (Figure 9.4). For crystalline Ta_2O_5, enhancement of the EXAFS signal was observed at 77 K, which is due to the decrease in thermal vibration of neighboring atoms around the central atom. The amplitude change between room temperature and 77 K is relatively more significant in the higher k-range than lower, indicative of a larger contribution of the thermal component in the Debye-Waller factor, σ^2, for the higher Ta shells. Overall, the fluorescence data of the 800 °C oxide (Figure 9.4) are consistent with β-Ta_2O_5 spectra. In contrast, thermal (400 °C) and anodic Ta oxides (Figure 9.4) show weaker oscillations from an oxygen shell at the low k region (around 4 $Å^{-1}$) than the 800 °C oxide and are dissimilar to that of Ta_2O_5 powder. Dissimilarity with the oxide originates from the contribution of the Ta substrate and is clearly seen in comparing the spectra to Ta foil

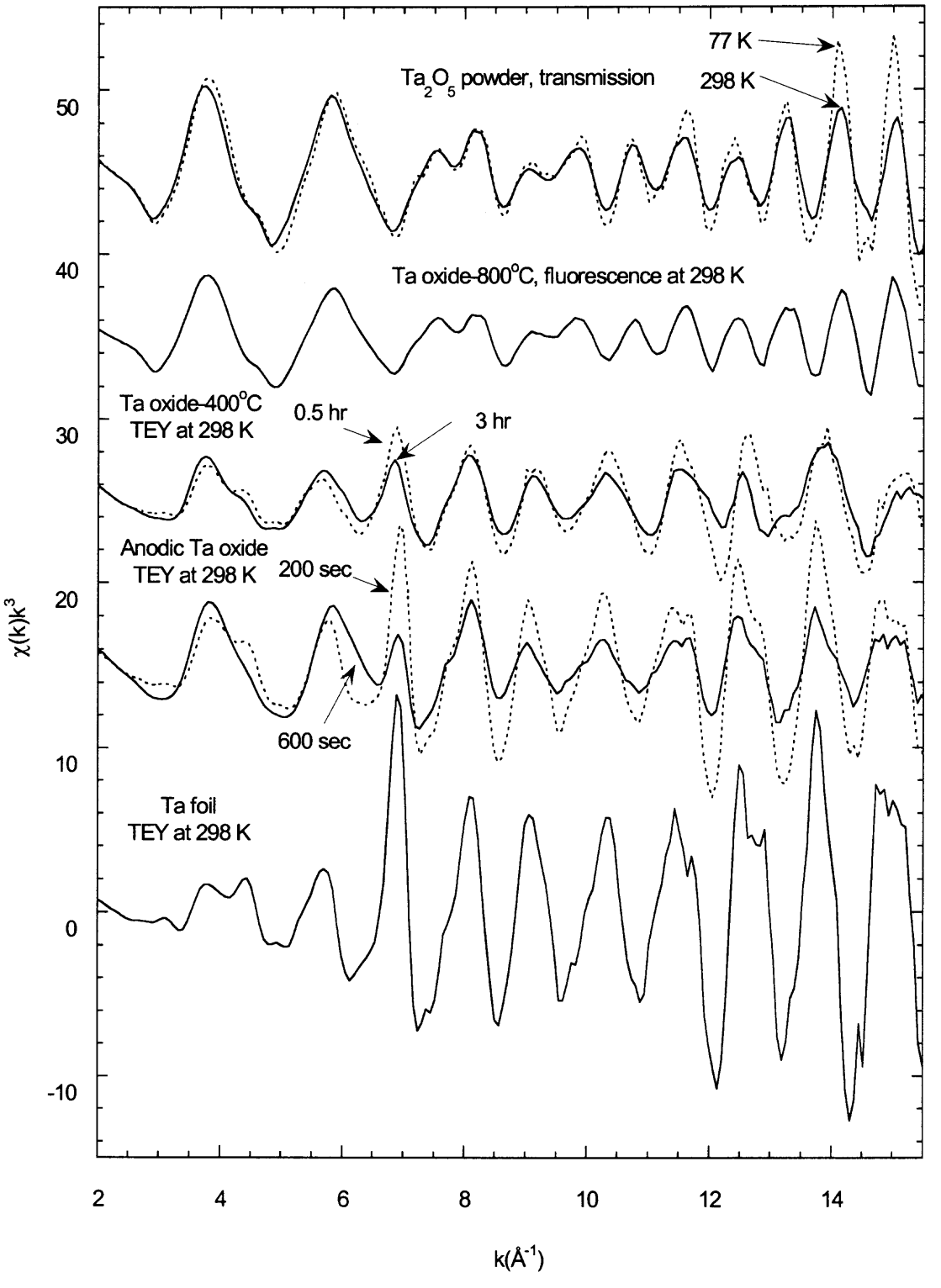

Figure 9.4 Ta L_{III}–edge $\chi(k)k^3$ spectra of Ta_2O_5 powder, 800 °C-thermal Ta oxide, 400 °C-thermal Ta oxide films, anodic Ta oxide films, and Ta foil.

where oscillations around 7 $Å^{-1}$ are observed. However, as exposure times in thermal (at 400 °C) and anodic oxidation increase, the contribution of the Ta substrate decreases due to the increase in oxide film thickness.

Typical radial structural functions around Ta atoms of β-Ta_2O_5 and α-Ta are observed (Figure 9.5); in the β-Ta_2O_5 spectra, the shells are indicative of oxygen and tantalum. The radial distances in the Fourier transforms are not corrected for the atomic and backscattering atom phase shift. Judging from the shape of radial distribution function, tantalum oxide formed at 800 °C appears to exhibit similar short-range atomic structure to the highly crystalline Ta_2O_5 powder except for the amplitude reduction over the entire radial range due to self-absorption in fluorescence. The temperature effect on the local structure of Ta_2O_5 powder shows that no significant change in the amplitude of the nearest neighbor (O shell, below 2 Å) is observed; again suggesting that static disorder is more significant than the thermal contribution. However, in the higher shells this effect becomes more important.

The data corresponding to the first shell (0.92 Å ≤ R ≤ 2.04 Å) were fitted with Ta-O coordination (Figure 9.6). Based on XRD, β-Ta_2O_5 exhibits a first shell comprised of three subshells with Ta-O radial distances of 1.839, 1.949 and 1.983 Å; each subshell has two oxygen atoms. In our fitting, the radial distances of the second and third subshells were combined with an average of four oxygen atoms. Two Gaussian subshells satisfied the distribution of oxygen in the first shell (Table 9.1). As a result, tantalum oxide formed at 800 °C reveals a slightly longer Ta-O interatomic distance with an increasing degree of disorder (σ^2) compared to highly crystalline β-Ta_2O_5 powder. Stringer [143] reported that high temperature oxidation from 600 - 800 °C results in the

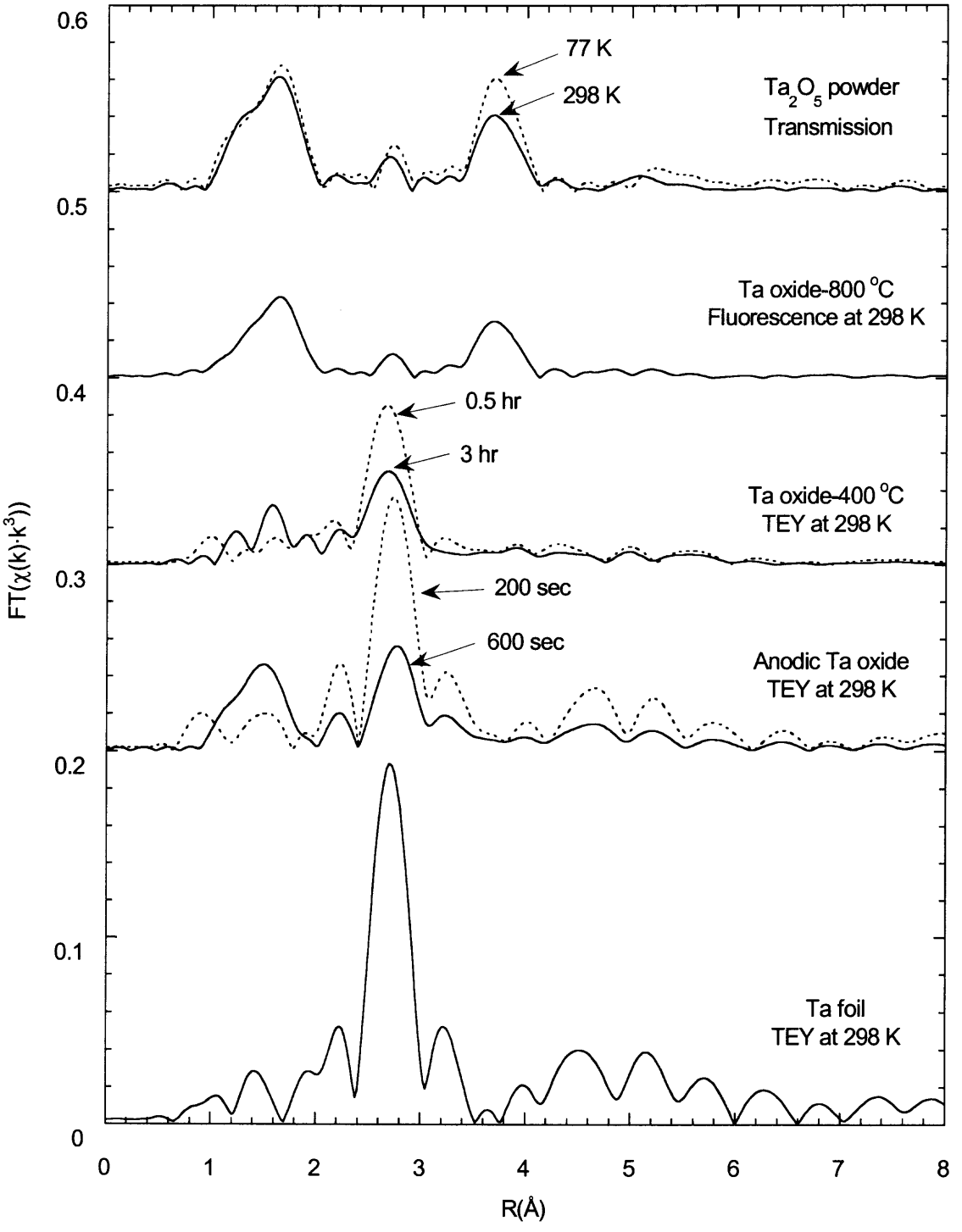

Figure 9.5 Fourier transforms of Ta L_{III}–edge $\chi(k)k^3$ spectra over the k range 2.2–15.2 Å.

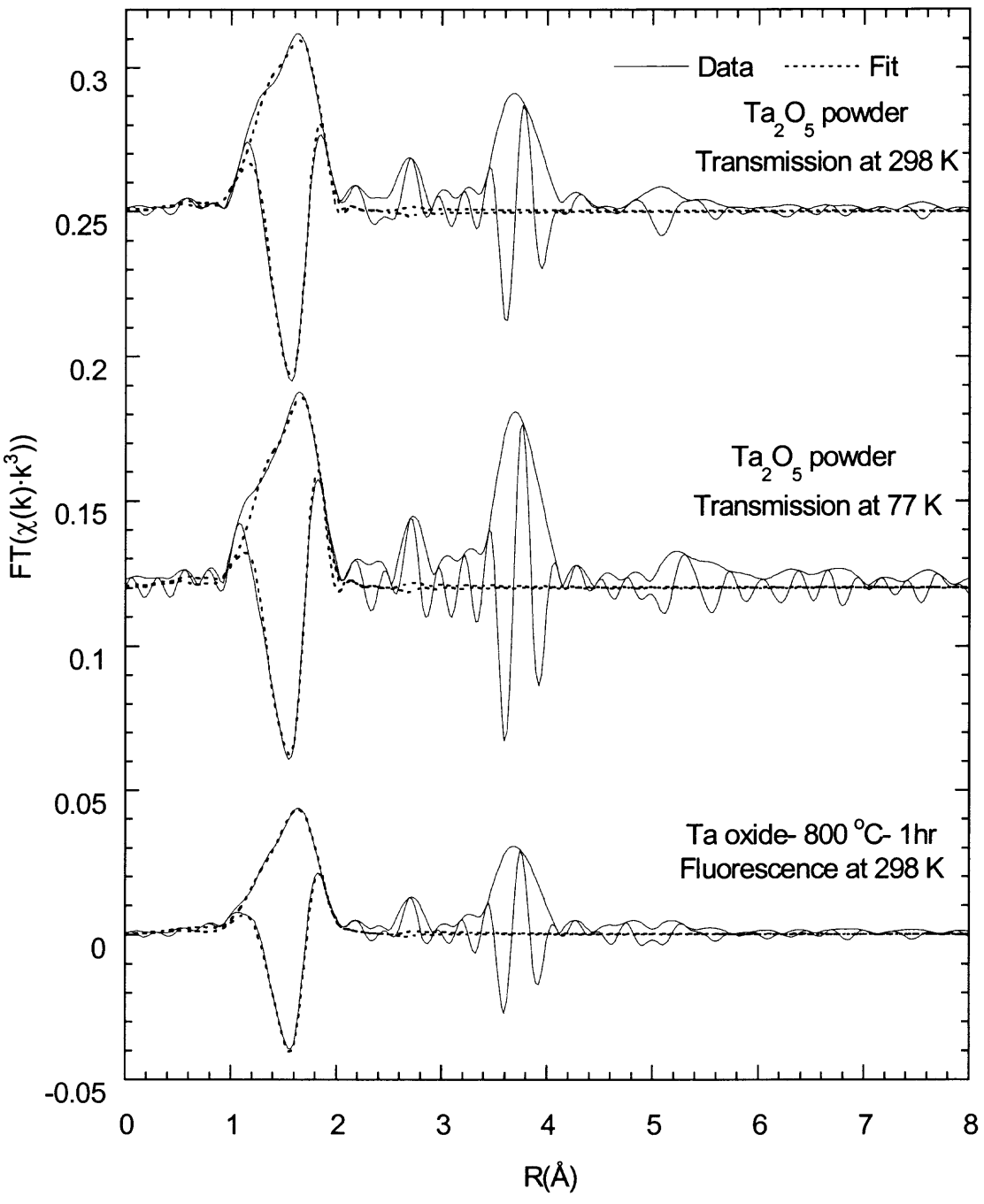

Figure 9.6 Fits to Fourier transform ($\chi(k)k^3$) vs. radial coordinate over the R range 0.92 – 2.04 Å of Ta_2O_5 powder transmission spectra at 298 and 77 K and the thermal Ta oxide (800 °C for 1hr) fluorescence spectra at 298 K.

Table 9.1 Results of EXAFS fitting for β-Ta_2O_5 powder and 800 °C thermal oxide film over 2.2 to 15.2 $Å^{-1}$ k-range and 0.92 to 2.04 Å r-range.

	β-Ta_2O_5 powder Transmission at 298 K**	β-Ta_2O_5 powder Transmission at 77 K**	HTO 800 °C Fluorescence at 298 K***	β-Ta_2O_5 XRD model
		1st subshell (O)		
N*	2	2	2	2
R (Å)	1.857 ± 0.019	1.854 ± 0.006	1.878 ± 0.011	1.839
σ^2 ($Å^2$)	0.00534 ± 0.00087	0.00560 ± 0.00092	0.00859 ± 0.00126	0
		2nd subshell (O)		
N*	4	4	4	4
R (Å)	2.007 ± 0.012	2.006 ± 0.004	2.018 ± 0.0054	1.966
σ^2 ($Å^2$)	0.00543 ± 0.00074	0.00505 ± 0.00042	0.00705 ± 0.00070	0

* Coordination number for fitting was fixed.

** S_0^2 was set as 1.0.

*** S_0^2 is 0.71 and was determined by comparing the amplitude ratio of fluorescence to transmission spectra for β-Ta_2O_5 powder at 298 K.

formation of porous β-Ta_2O_5 films due to the presence of TaO_z as an intermediate oxide. In the fitting of β-Ta_2O_5 between 298 K and 77 K, we observe no significant difference in Debye-Waller factor (σ^2) in the nearest shell of Ta-O. This result indicates that the static contribution is larger than that for the thermal even at room temperature. Because higher shells representing Ta involve multiple subshells, the number of fitting parameters exceeds the degrees of freedom and therefore it was not possible to carry out further shell-based EXAFS fitting.

In the TEY spectra (Figure 9.4) of tantalum oxide films produced at 400 °C and from anodic oxidation, the oxygen shell is not as distinguishable as that observed for the higher temperature samples. As mentioned earlier, these films are very thin where only the most significant contribution is from that of the Ta substrate, which is clearly seen by the presence of the Ta shell at approximately 2.6 Å and is consistent with the Ta foil (Figure 9.5). Interestingly, for these thin films, this Ta shell becomes less significant as the oxide thickness increases in thermal oxidation at 400 °C and anodic oxidation. A quantitative evaluation of the relative contributions of the two surfaces, Ta substrate and Ta oxide, to the spectra was accomplished by linear combination [136] of the $\chi(k)k^3$ data from α-Ta foil (TEY) and β-Ta_2O_5 reference (transmission) (Figures 9.7 and 9.8). XRD showed that the oxide films formed at 400 °C consist primarily of metastable metallic Ta oxide, TaO_x. However, Ta_2O_5 powder was employed as the model in this study because bulk, metastable Ta oxides were not commercially available. Backscattering over the k-range of 6.6 – 7.3 $Å^{-1}$ represents the Ta substrate contribution; therefore, reasonable fitting was accomplished by minimizing the residual in the fitting over that range. For the 400 °C samples (Figure 9.7), the Ta contribution decreases with increasing exposure time

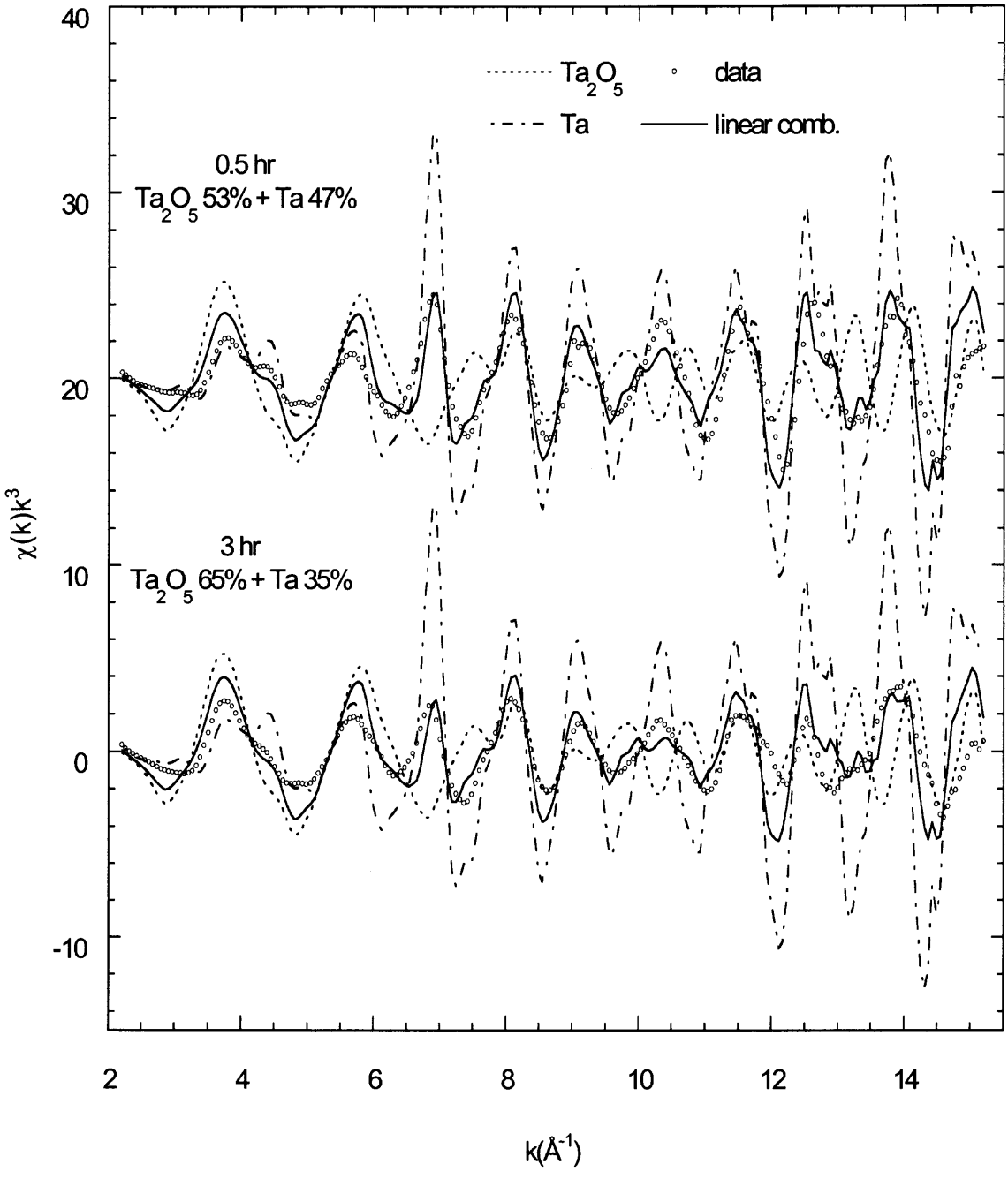

Figure 9.7 Ta L_{III}–edge $\chi(k)k^3$ spectra fitting with linear combination of the Ta_2O_5 and Ta spectra to the Ta oxide films (400 °C for 3 and 0.5 hr) over k range of 2.2 – 15.5 $Å^{-1}$.

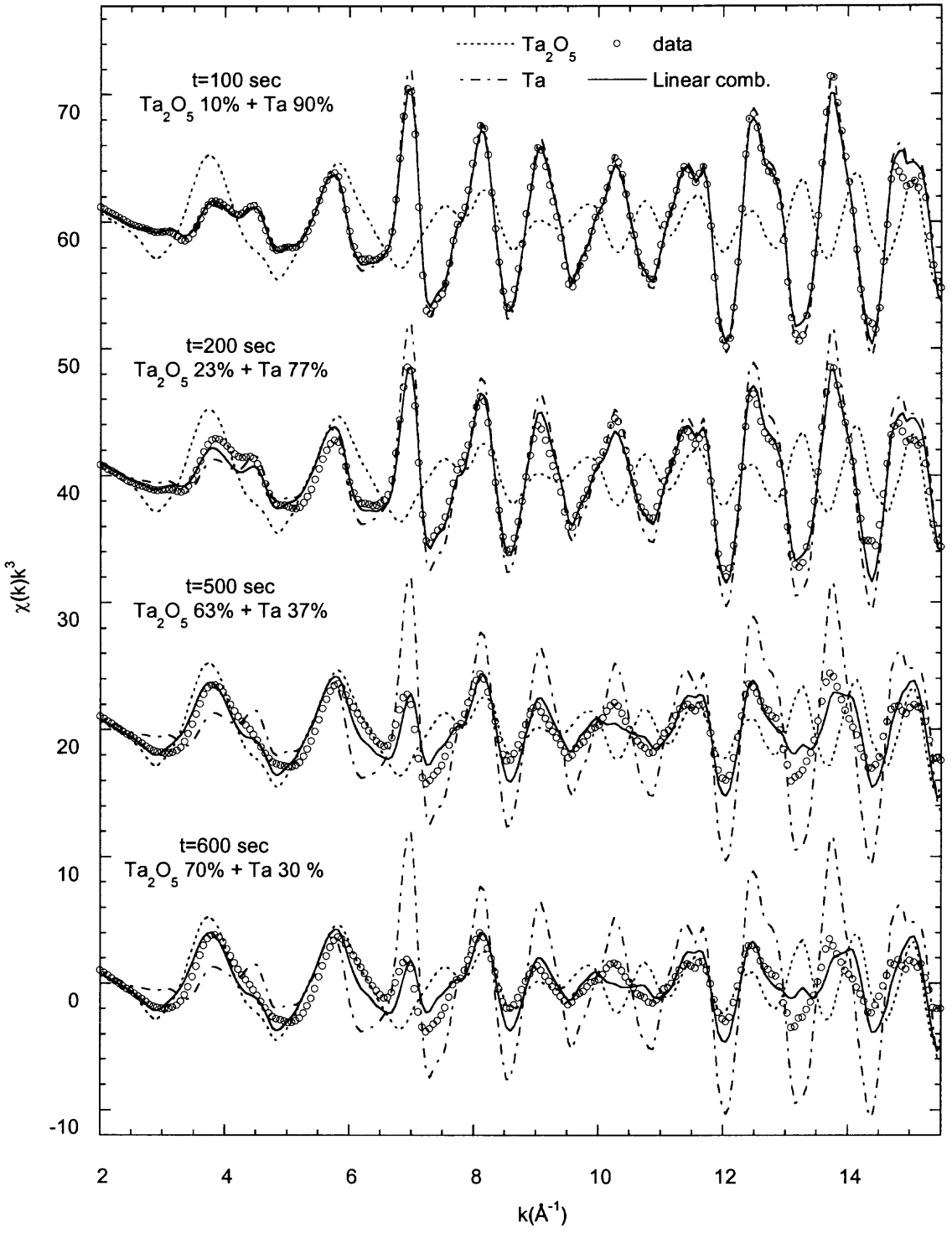

Figure 9.8 Ta L_{III}–edge $\chi(k)k^3$ spectra fitting using linear combination of the Ta_2O_5 and Ta spectra to the anodic Ta oxide films over k range of 2.0 – 15.5 $Å^{-1}$.

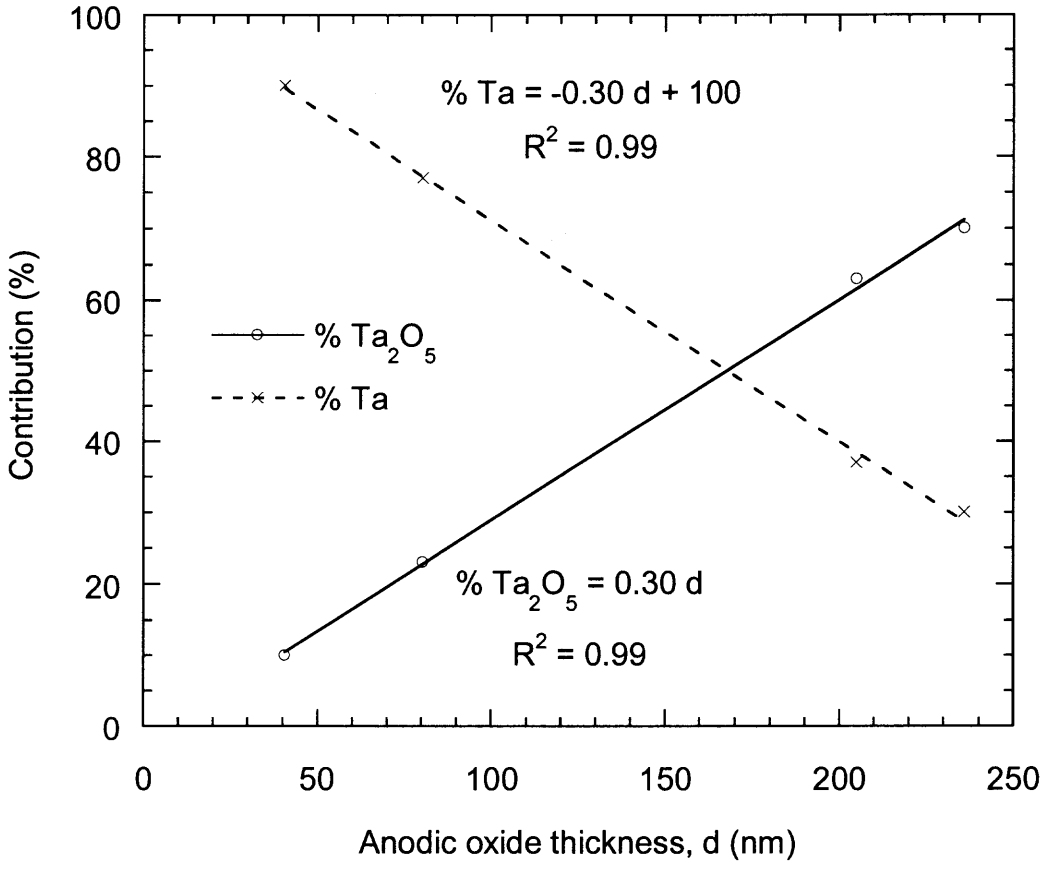

Figure 9.9 Contribution of the two model spectra, β-Ta_2O_5 and Ta, in fitting the Ta L_{III}-edge $\chi(k)k^3$ spectra of anodic oxide films with various oxide thickness. The linear relationship is depicted by the solid line.

due to the increase in oxide thickness; weak oscillations below 6 $Å^{-1}$ can be attributed to the oxygen shell as well as the overall disorder of the structure. A better fit, however, was obtained for the anodic oxide films (Figure 9.8) over the low k-range with the use of Ta_2O_5 powder spectra, indicating that the anodic oxide film has a relatively well ordered-local structure compared to its long-range one. Moreover, Ta_2O_5 contribution appears to be linearly related (Figure 9.9) to the oxide film thickness which is based on the total charge passed during anodic oxidation; this effect is consistent with Kerrec et al. [23].

9.4 Summary

Tantalum oxide films from thermal and anodic oxidation were investigated by XRD, SEM, and EXAFS. Thermal Ta oxide produced at 800 °C shows orthorhombic structure (β-Ta_2O_5) with a slightly greater degree of disorder in the short-range structure than the β-Ta_2O_5 powder reference. Temperature effects on local structure of β-Ta_2O_5 showed that the static contribution is larger than the thermal one for the first shell, and shows the reverse trend for higher shells. Films produced at 400 °C (0.5 and 3 hr) are comprised of metastable TaO_x demonstrating the relative stability of this oxide. Morphological evaluation on these thin Ta oxide films (400 °C) confirmed the formation of metastable platelets. The TaO_x suboxide exhibits a first shell not unlike that of β-Ta_2O_5, but with greater disorder. In contrast, the anodic Ta oxide film that is amorphous appears to have a relatively well ordered local structure. Fitting of the nanometer anodic oxide films with the linear combination approach revealed that Ta_2O_5 contribution is linearly related to the oxide thickness. Overall, this research demonstrates that that the nanometer oxide films formed on tantalum exhibit a first shell like that of the β-Ta_2O_5 reflecting the very compact nature that enhances its corrosion resistance. In the next chapter, the overall conclusions of this study are summarized.

CHAPTER 10

CONCLUSIONS

The overall objective of this research was to evaluate the corrosion performance of Ta coating on steel substrate as part of investigating replacement of electrodeposited hard Cr coatings. In order to meet the objective, the approach in this research was divided in to four parts. In the first part, the corrosion behavior of α- and β-Ta coatings was studied as a function of coating thickness to obtain a viable coating thickness (Chapter 6). In the next part, the effect of steel substrate roughness on the corrosion behavior of the viable coating was investigated (Chapter 7). The third part was to compare corrosion performance of Ta coating with Cr coatings, which were produced in full-scale processes (Chapter 8), and in the last part, an evaluation of the passive Ta oxide was conducted as the oxide is a barrier between Ta metal and corrosive environments enhancing the corrosion resistance (Chapter 9).

In Chapter 6, the galvanic behavior of Ta coatings on steel (AISI 4340) substrates with various cathodic to anodic area ratios revealed localized corrosion of the steel substrate at open pores due to galvanic action. However, the coating porosity was observed to decrease with increasing coating thickness and hence, the thicker coating showed greater corrosion resistance. For coatings less than 10 μm (α– or β–Ta), porosity was significant and open pores resulted in severe localized corrosion of the steel substrate, coating delamination, and overall coating failure. In addition, the β-Ta coatings were more susceptible than the α-phase to delamination. In contrast to thin coatings, the electrochemical impedance behavior of α-Ta coatings with thicknesses of 50 μm and 100

μm was comparable to that of Ta foil. Consequently α-Ta coatings greater than 50 μm demonstrated viability and corrosion resistance. However, the surface modification (fine-polishing) used for the steel substrate in this study is not feasible in full-scale process. Therefore, to assess the effect of steel substrate roughness on the coating quality of the viable coating was conducted.

In Chapter 7, α-Ta coatings on rough steel substrates (AISI 4340) were studied in an effort to assess the resulting porosity and corrosion behavior. While the long-range crystallographic orientation of the coatings was found to be affected by the surface roughness, the short-range structure was invariant. Peak broadening in X-ray diffraction patterns attributed to microstrain and particle size was observed for coatings on both types of substrates as compared to Ta powder. Although the roughness was two orders of magnitude greater for the coatings deposited on the rough substrates than the smooth ones, the porosity was not significantly different. Furthermore, electrochemical impedance behavior over long exposure times of coatings deposited on smooth and rough steel substrates was similar to that of Ta foil. These results demonstrate that substrate roughness appears to have little to no effect on the coating quality with respect to corrosion performance for 50 μm coatings.

In Chapter 8, the corrosion behavior of α- and β-Ta coatings was compared to that of Cr coatings produced by cylindrical magnetron sputtering as well as electrodeposition in full scale processes. For Ta coatings, the corrosion process was dominated by dissolution of the steel substrate through open pores, however, at the end of 5 days, coating degradation was not observed. In contrast, while open pores were not observed with the Cr coatings, the corrosion resistance decreased as a function of time

under acidic conditions, as a result of the protective oxide dissolution. Initially, however, the sputtered Cr coating exhibited improved corrosion resistance over the electrodeposited one, potentially due to the surface structure of the oxide film. Both Cr coatings showed similar transpassive behavior to that of pure Cr; the current density of the sputtered Cr coating was observed to be greater than that of the electrodeposited one in the transpassive region due to the extensive droplet-like defects.

In Chapter 9, the passive oxide film responsible for the highly resistant behavior was investigated. Tantalum oxide films produced from anodic oxidation and thermal oxidation at 400 and 800 °C were studied with respect to long- and short-range structure by x-ray diffraction and x-ray absorption spectroscopy, respectively. Films formed at 800 °C show orthorhombic structure (β-Ta_2O_5) with greater disorder compared to the β-Ta_2O_5 powder reference, where six O atoms were observed at an average radial distances of 1.957 ± 0.014 (Ta_2O_5 powder) and 1.971 ± 0.007 Å (800 °C Ta oxide film). Lower temperature films consist primarily of metastable TaO_x (Ta_2O) and appear to be relatively stable for extended times of treatment with a first shell not unlike that of β-Ta_2O_5, based on a linear combination analysis. Furthermore, using a linear combination of β-Ta_2O_5 and α-Ta metal, the amorphous anodic oxide films studied as a function of thickness were observed to exhibit a relatively ordered local structure consistent with the high temperature (i.e., 800 °C) phase. This work demonstrates that the nanoscale oxide films formed on tantalum exhibit an ordered local structure reflecting the very compact nature that enhances its corrosion resistance.

CHAPTER 11

FUTURE RESEARCH

In this study, we investigated the corrosion behavior of Ta coatings under the simple condition of deaerated 0.5 M H_2SO_4 solution, providing easy assessment of presence of open pores for the coatings. From the results, the α-Ta coating with thickness greater than 50 μm exhibited equivalent corrosion behavior to that of bulk Ta, demonstrating a viable coating. For further assessment on the stability of the viable coating, it is necessary to investigate its corrosion behavior over several months of exposure and include test environments simulating for example marine environment and harsh conditions than gun-bore may undergo such as fuming nitric, sulfuric, and hydrochloric acids.

This study revealed that as coating thickness increases, the porosity significantly decreases and hence, the corrosion resistance increases. This observation provides the insight that if less porosity of the coating can be achieved in the sputtering process, the viable coating thickness can be reduced with respect to corrosion performance. Therefore, further optimizing the sputtering process may be worth while.

As mentioned earlier, the electrochemical techniques used in this study with deaerated 0.5 M H_2SO_4 solution are very useful to quantitatively evaluate the porosity of Ta coating. However, the porosity measurement by these techniques needs to be further developed for quality control purposes of the Ta coating. On example is to include calibration.

In addition to corrosion, one of the major contributors to erosion damage that gun-bore experiences is the thermal effect. Currently, Benet Laboratories investigates the

application of laser pulse heating to simulate thermal shock on gun-bore. Porosity assessed electrochemically can then be applied to evaluate the damage of coating induced by thermal shock. Therefore, the degree of damage by thermal shock will be correlated to the increase in porosity of the coating.

APPENDIX A

ELECTROCHEMICAL IMPEDANCE SPECTROSCOPY OF AISI 4340 STEEL

EIS of AISI 4340 steel as a function of immersion time in deaerated 0.5 M H_2SO_4 solution purged with N_2 gas are plotted in Nyquist and Bode plot.

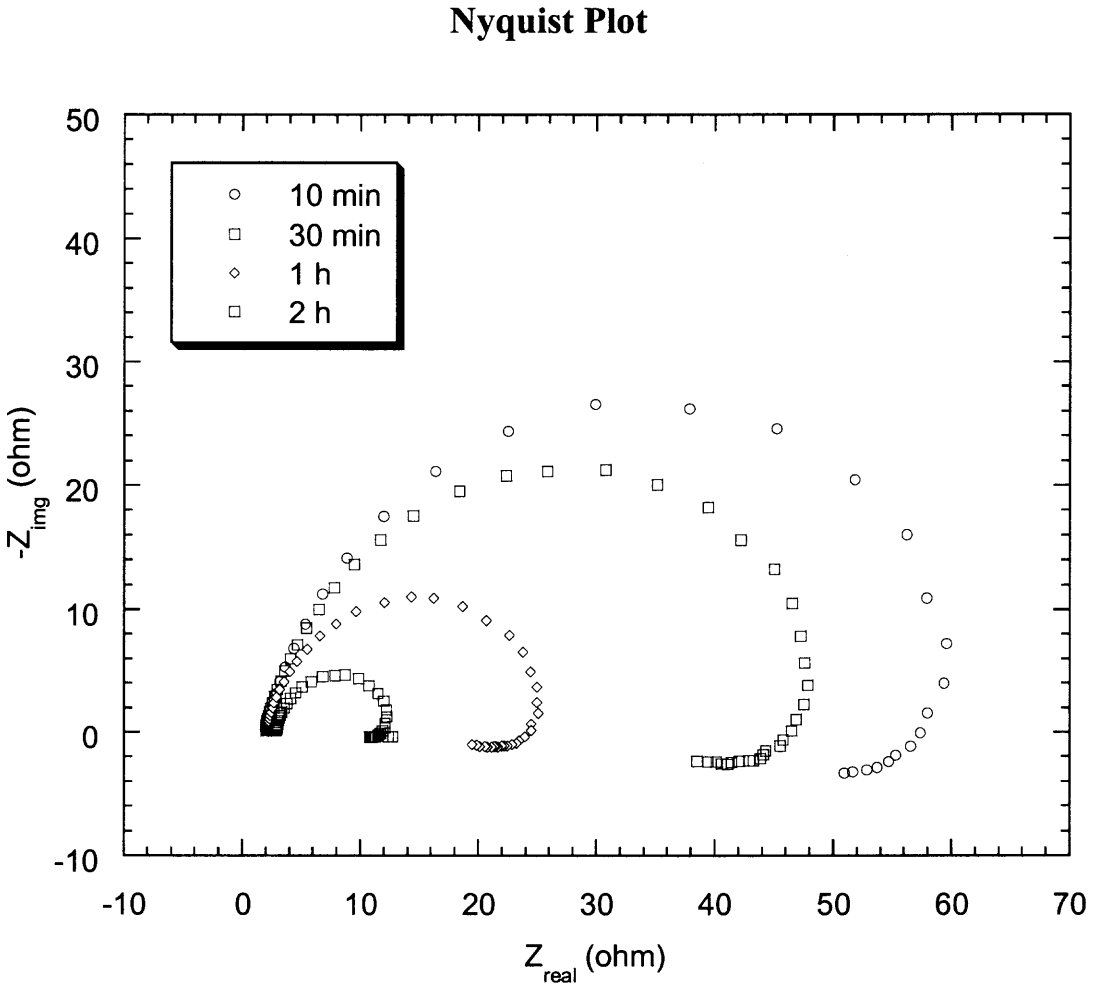

Bode Plot

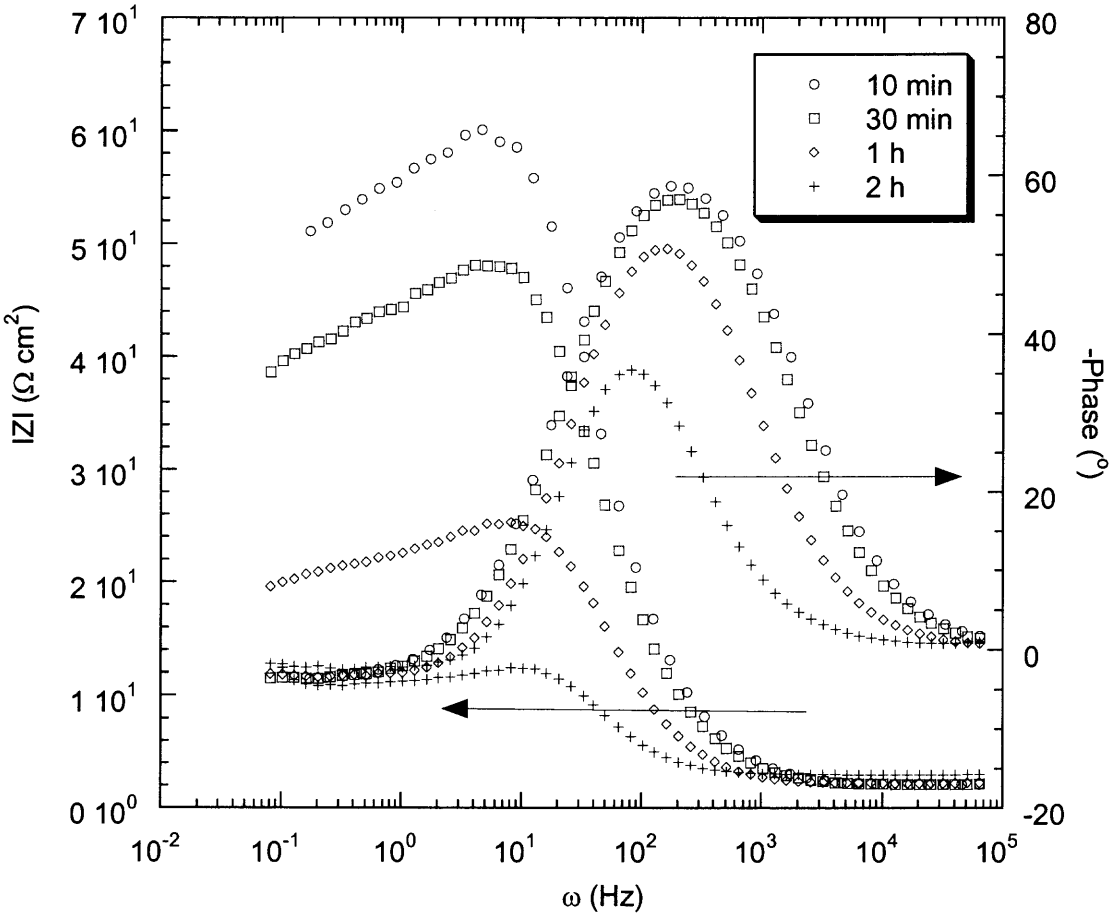
7 10^1
6 10^1
5 10^1
4 10^1
3 10^1
2 10^1
1 10^1
0 10^0
|Z| (Ω cm^2)
80
60
40
20
0
-20
-Phase (°)
10^-2
10^-1
10^0
10^1
10^2
10^3
10^4
10^5
ω (Hz)
10 min
30 min
1 h
2 h

APPENDIX B

DEKTAK SURFACE PROFILES OF ROUGH STEEL AND 50 μM THICK TA COATINGS ON ROUGH STEEL SUBSTRATE

(1) Dektak profile of rough steel #1

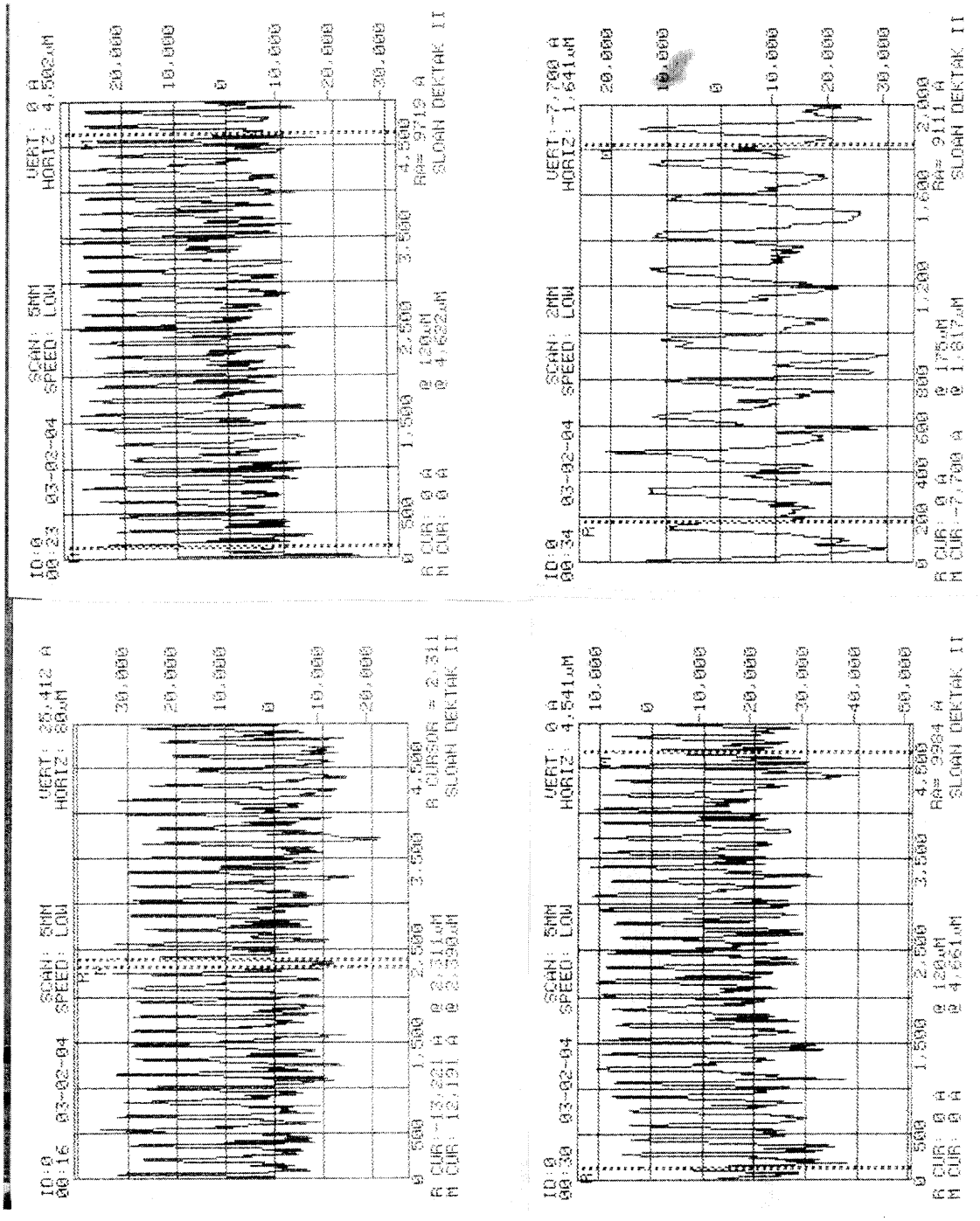

(2) Dektak profile of Rough steel #2

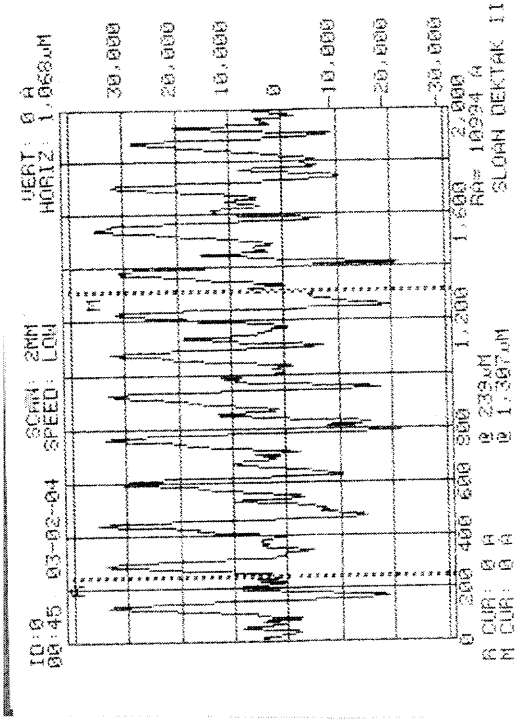

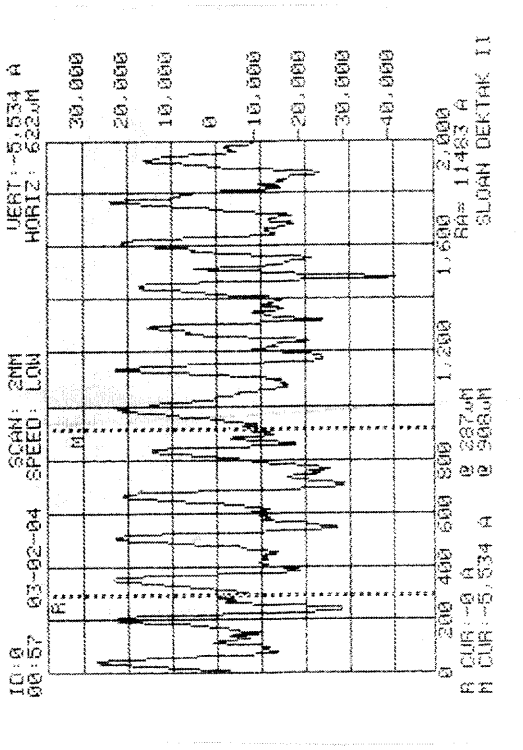

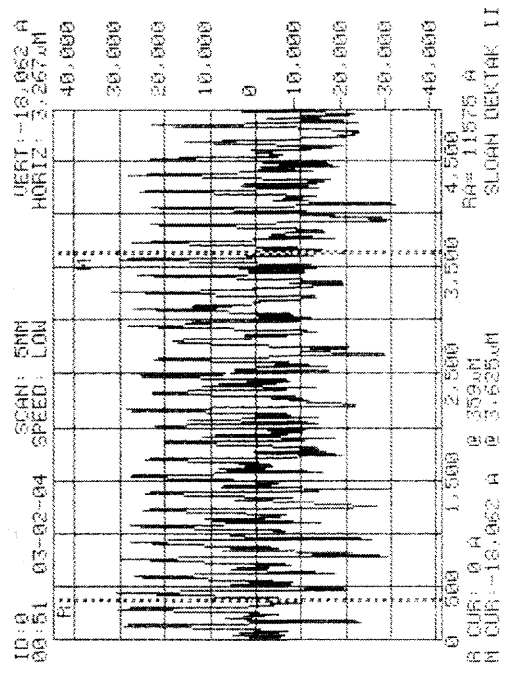

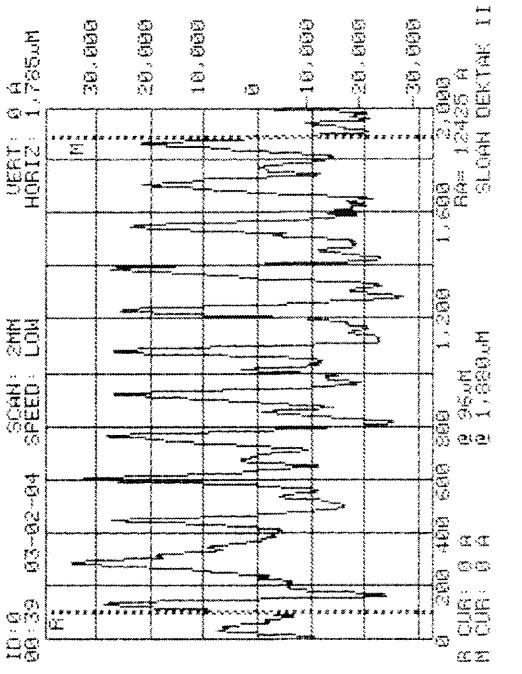

(3) Dektak profile of Rough steel #3

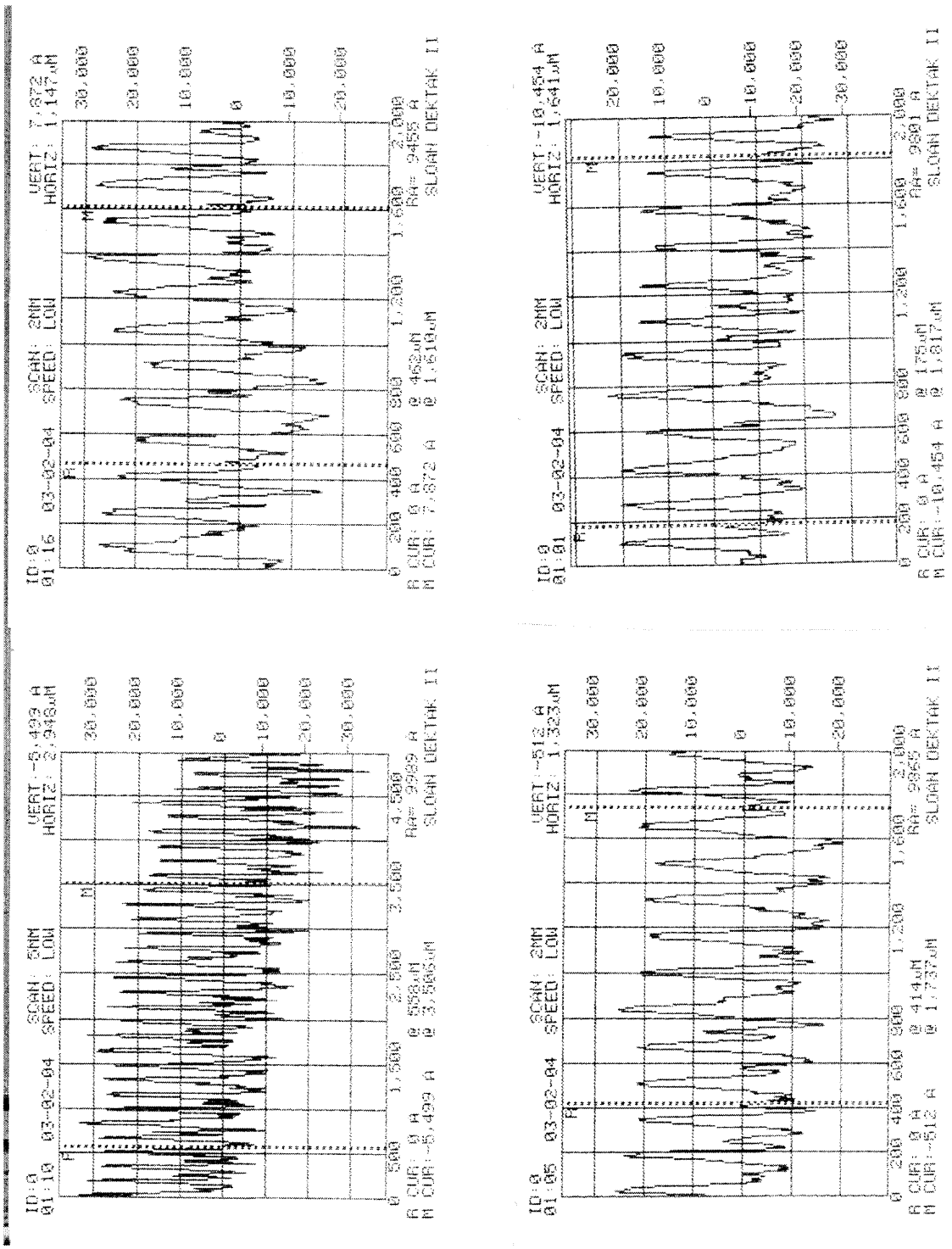

(4) Dektak profile of 50 μm α-Ta coating (PT04a1) on rough steel substrate

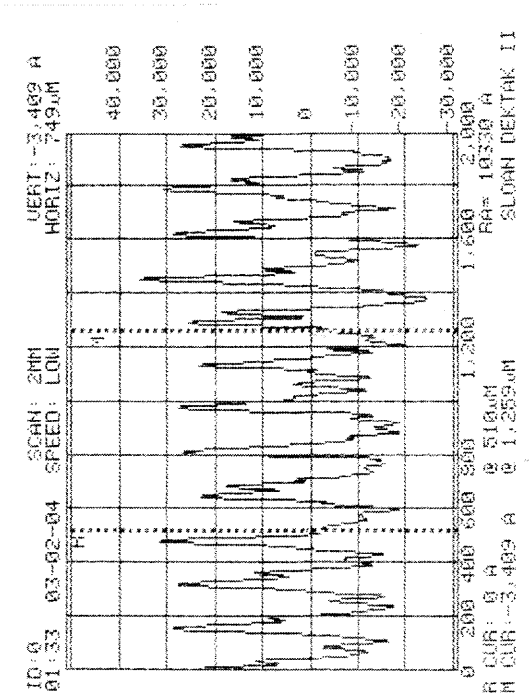

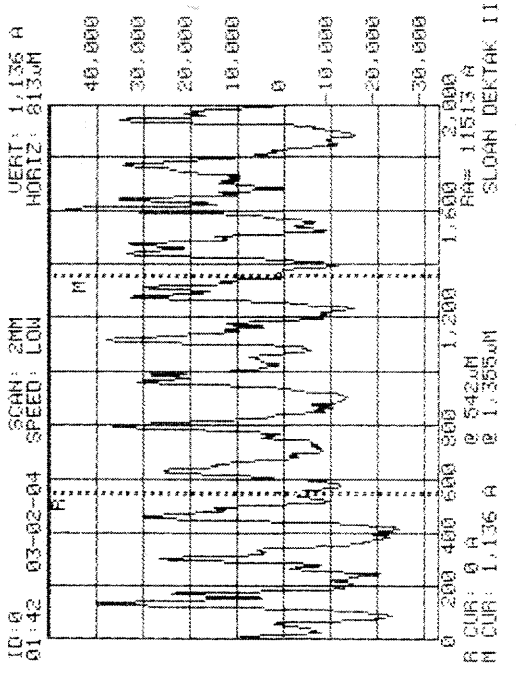

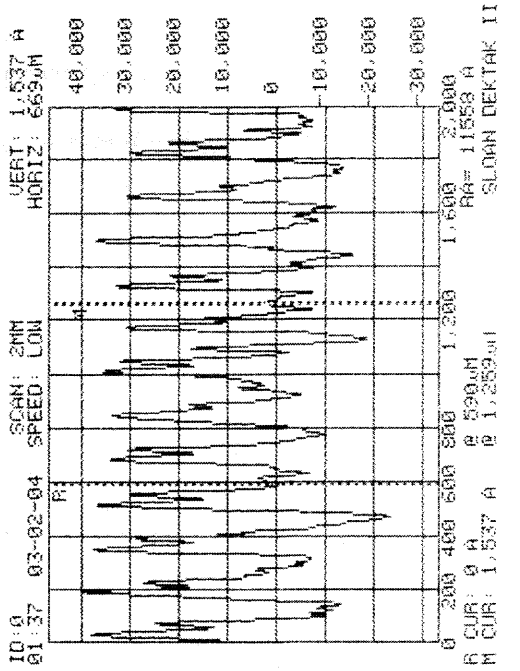

(5) Dektak profile of 50 μm α-Ta coating (PT04a3) on rough steel substrate

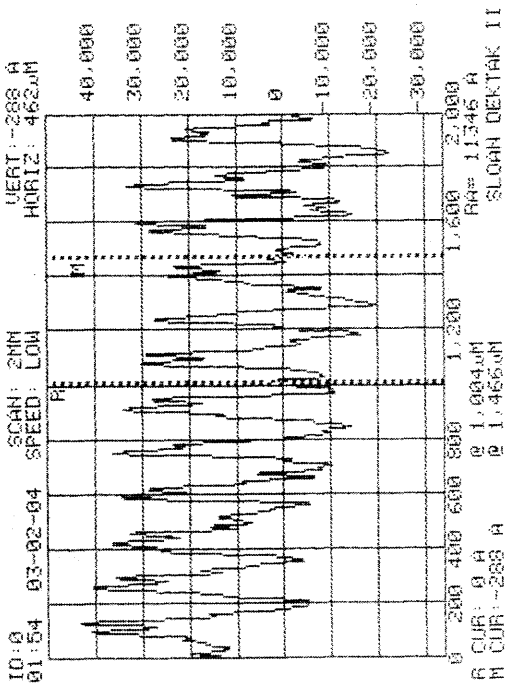

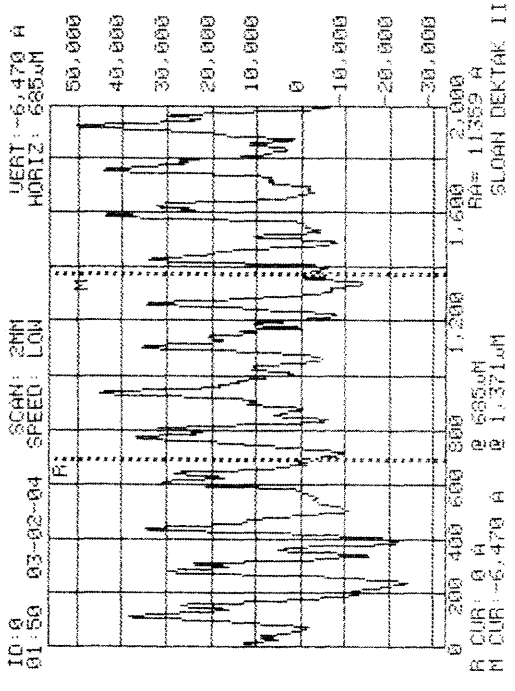

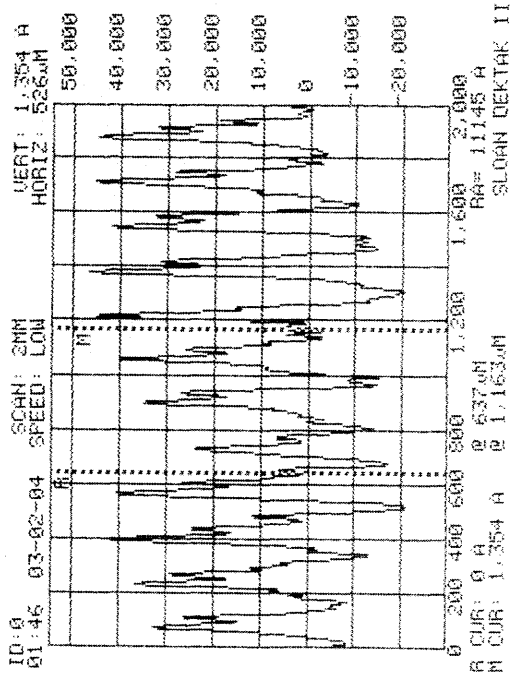

(6) Dektak profile of 50 μm α-Ta coating (PT04a5) on rough steel substrate

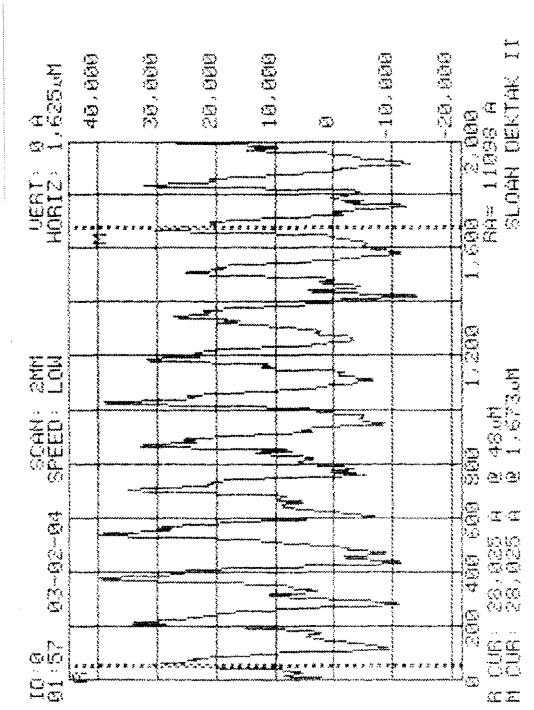

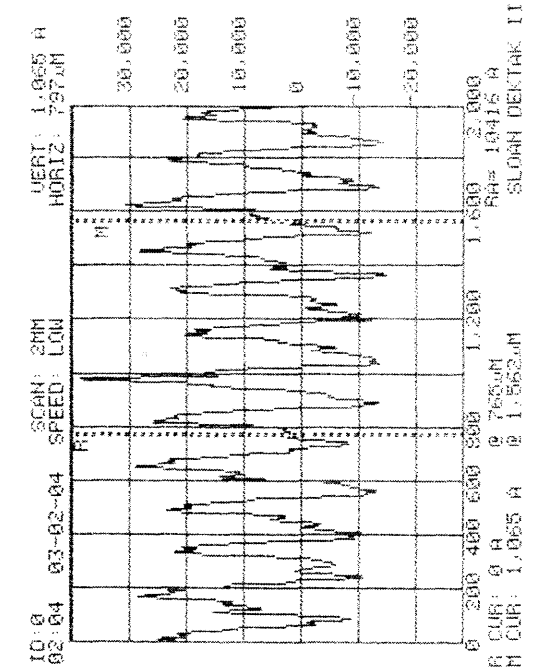

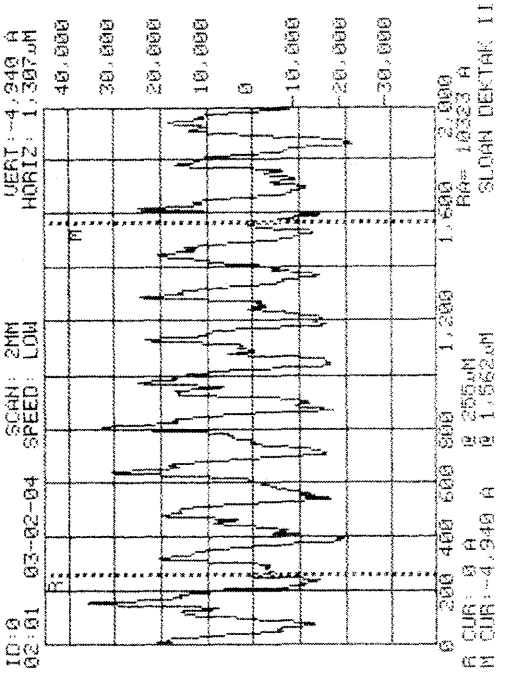

REFERENCES

1. J. R. Davis, *Metals Handbook*, 9th Ed., Vol. 14: Corrosion, ASM International, Metals Park, OH (1978).

2. I. Ahmad, P. Greco, G. D'Andrea, J. Barranco, *MCIC Rep.* (MCIC-79-40, Proc. 1978 Tri-Serv. Conf. Corros.), pp. 203-16 (1979).

3. U. S. DoD, EXECUTIVE ORDER 13148 INTERAGENCY WORKGROUP REQUEST FOR FEDERAL AGENCY, FIELD-LEVEL COMMENT: Executive Order 13148, Section 203, [http://epic.er.doe.gov/epic/pdfs/callforcomment/PDF] (2000).

4. D. W. Matson, M. D. Merz, E. D. McClanahan, *J. Vac. Sci. Technol.* A 10 (1992) 1791.

5. S. L. Lee, D. Windover, *Surf. Coat. Technol.* 108/109 (1998) 64.

6. S. L. Lee, M. Cipollo, D. Windover, C. Rickard, *Surf. Coat. Technol.* 120/121 (1999) 44.

7. G. Das, *Thin Solid Films* 12 (1972) 305.

8. R. D. Burbank, *Acta Cryst.* 6 (1973) 217.

9. P. T. Moseley, C. J. Seabook, *Acta Cryst.* B29 (1973) 1170.

10. N. O. Nnolim, T. A. Tyson, L. Axe, *J. Applied Physics* 93 (2003) 1.

11. A. Jiang, A. Yohannan, N. O. Nnolim, T. A. Tyson, L. Axe, S. Lee, P. Cote, *Thin Solid Films* 437 (2003) 116.

12. W. D. Westwood, N. Waterhouse, P. S. Wilcox, *Tantalum Thin Films*, Academic Press, London, 1975.

13. M. H. Read, C. Altman, *Applied Physics Letters* 7 (1965) 51.

14. I. M. Notter, D. R. Gabe, *Corrosion Reviews* 10 (1992) 217.

15. J. Creus, H. Mazille, H. Idrissi, *Surface and Coatings Technology* 130 (2000) 224.

16. I. M. Notter, D. R. Gabe, *Corrosion Science* 34 (1993) 851.

17. L. L. Shreir, R. A. Jarman, G. T. Burstein, *Corrosion*, Vol. 1, 3rd Ed., Butterworth-Heinemannl, Oxford (1994).

18. E.A. Brandes, *Smithells Metals Reference Book*, 6th ed., Butterworths, London (1983)

19. H. S. Betrabet, W. B. Johnson, D. D. Macdonald, W. A. T. Clark, *Proc. Electrochem. Soc.*, 84 (1984) 83.

20. M. Pourbaix, *Atlas of Electrochemical Equilibria in Aqueous Solutions*, Pergamon Press, New York (1966).

21. J. Chelius, "Use of Refractorty Metals in Corrosive Environment Service," Mater. Eng. Quart., pp. 57-59, Aug. 1957.

22. R. B. Flanders, "Try Tantalum for Corrosion Resistance," Chem. Eng. Vol. 17 (1979).

23. O. Kerrec, D. Devillier, H. Groult, M. Chemla, *Electrochimica Acta* 40 (1995) 719.

24. D. R. Lide (Editor-in Chief), CRC Handbook of Chemistry and Physics, 83th edition, CRC Press, Inc., Boca Raton, FL (2002).

25. C. Chaneliere, J. L. Autran, R. A. B. Devine and B. Balland, *Materials Science & Engineering Reports: A Review Journal* R22 (1998) 269.

26. V. I. Khitrova, V. V. Klechkovskaya, Z. G. Pinsker, *Kristallografiya* 21 (1976) 937.

27. V. I. Khitrova, V. V. Klechkovskaya, Z. G. Pinsker, *Kristallografiya* 12 (1967) 1044.

28. V. I. Khitrova, V. V. Klechkovskaya, Z. G. Pinsker, *Kristallografiya* 24 (1979) 1254.

29. V. V. Klechkovskaya, V. I. Khitrova, *Kristallografiya* 13 (1968) 523.

30. K. Lehovec, *Less-Common Metals* 7 (1964) 397.

31. U. Balachandran, N. G. Eror, *Material Science Letters* 1 (1992) 219.

32. V. I. Khitrova, V. V. Klechkovskaya, *Kristallografiya* 25 (1980) 1169.

33. L. Young, *Anodic Oxide Film*, Academic Press Inc., New York (1961).

34. J. Hirvonen, A. G. Revesz, T. D. Kirkendall, *Thin Solid Films* 33 (1976) 315.

35. D. J. Smith, L. Young, *IEEE Trans. Electron Devices* ED-28(1981) 22.

36. J. P. S. Pringle, *J. Electrochem. Soc.* 120 (1973) 482.

37. K. W. Kwon, C. S. Kang, T. S. Park, Y. B. Sun, N. Sandler, D. Tribula, *Mater. Soc. Symp. Proc.* 284 (1993) 505.

38. C. H. An, K. Sugimoto, *J. Electrochem. Soc.* 139 (1992) 1956.

39. M. G. Fontana, *Ind. Eng. Chem.*, 44 (1952) 71A.

40. G. A. Hampel, *Rare Metals Handbook*, Reinhold, London (1961) 469.

41. L. L. Shreir, R. A. Jarman, G. T. Burstein, *Corrosion*, Vol. 2, 3rd Ed., Butterworth-Heinemann, Oxford (1994).

42. M. Haissinsky, *Metaux et Corrosion*, 23 (1948) 15.

43. K. Lehovec, J. D'Amico, *J. Electrochem. Soc.: Solid State Science* 114 (1967) 363.

44. K. Lehovec, J. D'Amico, *J. Electrochem. Soc.: Solid State Science* 114 (1967) 495.

45. F. J. Hunkeler, Properties of Tantalum for Applications in the Chemical Process Industry, NRC Inc. (1983).

46. W. Wilhelmsen, *Electrochimica Acta*, 33 (1) (1988) 63.

47. D. A. Vermilyea, *J. Electrochem. Soc.*, 103 (1956) 690.

48. E. E. Stansburry, R. A. Buchanan, Fundamentals of electrochemical corrosion, ASM International, Material Park, OH (2000).

49. J. O. M. Bockris and A. K. N. Reddy, Modern Electrochemistry, Vol. 2, pp. 1432, Plenum Press, New York (1970).

50. J. O. Bockris and A. K. N. Reddy, Modern Electrochemistry, Vol. 2, p. 632, Plenum Press, New York (1973).

51. K. J. Vetter, *Electrochemical Kinetics*, Academic Press, p. 104-395 (1967).

52. L. Bai, B. E. Conway, *J. Electrochem. Soc.*, 137 (12) (1990) 3737.

53. L. Bai, B. E. Conway, *Electrochim Acta*, 38 (14) (1993) 1803.

54. M. Keddam, O. R. Mattos, H. Takenouti, *J. Electrochem. Soc.; Electrochemical Science and Technology*, 128 (2) (1981) 257.

55. R. Cottis, S. Turgoose, *Corrosion Testing Made Easy: Electrochemical Impedance and Noise*, NACE International, Houston, TX (1999).

56. C. Gabrielli, *Electrochemical Impedance Spectroscopy: Principles, Instrumentation, and Applications*, Editor: I. Rubinstein, Physical Electrochemistry, Marcel Dekker Inc., New York, NY (1995).

57. M. Stern, A. L. Geary, *J. Electrochem. Soc.* 104 (1957) 56.

58. M. Kendig, F. Mansfeld, S. Tsahi, *Corrosion Science* 23 (1983) 317.

59. M. W. Kendig, E. M. Meyer, G. Lindberg, F. Mansfeld, *Corrosion Science* 23 (1983) 1007.

60. ASTM G106-89, *Standard Practice for Verification of Algorithm and Equipment for Electrochemical Impedance Measurements*, ASTM International, West Conshohocken, PA (1999).

61. M. Urquid-Macdonald, S. Real, D. D. Macdonald, *J. Electrochem. Soc.* 133 (1986) 2018.

62. H. Shih, F. Mansfeld, *Corrosion Science* 28(1988) 933.

63. Z. Aoltowski, *J. Electroanal. Chem.* 240 (1988) 53.

64. R. L. Zellar III, R. F. Savinell, *Corrosion Science* 26 (1986) 591.

65. B. A. Boukamp, *Solid State Ionics*, 18-19, Part I (1986) 136.

66. D. C. Silverman, *Practical Corrosion Prediction using Electrochemical Techniques, Uhlig's Corrosion Handbook*, 2nd Ed., Edited by R. Winston Revie, John Wiley & Sons, Inc., pp. 1179-1225 (2000).

67. F. M. Al-Kharafi, W. A. Badawy, *Electrochimica Acta* 40 (1995) 2623.

68. J. R. Macdonald, *Impedance Spectroscopy*, p. 173, John Wiley & Sons, Inc., New York (1987).

69. B. D. Cahan, C. T. Chen, *J. Electrochem. Soc.* 129 (1982) 700.

70. F. Mansfeld, M. Kendig, S Tsai, *Corrosion*, 38 (1982) 478.

71. C. Liu, A. Leyland, S. Lyon, A. Matthews, *Surface and Coatings Technology* 76-77 (1995) 615.

72. G. M. Treacy, G. D. Wilcox, M. O. W. Richardson, *Surface and Coatings Technology* 114 (1999) 260.

73. X. G. Zhang, Galvanic Corrosion, Uhlig's Corrosion Handbook, 2nd Ed., Edited by R. Winston Revie, John Wiley & Sons Inc., New York (2000).

74. D. A. Jones, Principles and Prevention of Corrosion, 2nd Ed., Prentice-Hall Inc., Upper Saddle River, NJ (1996).

75. R. Morris, W. Smyrl, *J. Electrochem. Soc.* 136 (1989) 3237.

76. F. Mansfeld, D. H. Hengstenberg, J. V. Kenkel, *Corrosion* 30 (1974) 343.

77. A. K. Babko, V. V. Lukaehina, B. I. Nabinanets, Russ, *J. Inorg. Chem.* 8 (1963) 957.

78. S. R. Morrison, *Electrochemistry at Semiconductor and Oxidized Metal Electrodes*, Plenum, New York (1980).

79. J. W. Schultze, V. A. Macagno, *Electrochimica Acta* 13 (1986) 355.

80. S. M. Wilhelm, "*Galvanic Corrosion caused by Corrosion Product*," *Galvanic Corrosion*, ASTM STP978, edited by H. P. Hack, American Society for Testing and Materials, Philadelphia, PA, pp. 23-24 (1988).

81. P. T. Gilbert, "*An Investigation into the Corrosion in Zinc and Zinc-Coated Steel in Hot Waters*," Sheet Metal Industries, October-December (1948).

82. D. R. Gabe, A. M. El Hassan, *British Corrosion Journal* 21 (1986) 185.

83. ASTM G31-72, *Standard Practice for Laboratory Immersion Corrosion Testing of Metals*, ASTM International, West Conshohocken, PA (1999).

84. H. I. McHenry, D. T. Read, T. R. Shives, *Mater. Perform.* 26 (1987) 18.

85. H. K. Birnaum, "*Environment-Sensitive Fracture of Engineering Materials*," edited by Z. A. Foroulis, American Institute of Mining, Metallurgical, and Petroleum Engineers, Warrendale, PA (1979) pp. 326-357.

86. T. P. Groeneveld, E. E. Fletcher, A. R. Elsea, "*A Study of Hydrogen Embrittlement of Various Alloy*," Battle Columbus Laboratories, Columbus, OH, 23 June 1966.

87. F. E. Bacon, P. M. Moanfeldt, Reaction with the Common Gases, in *Columbium and Tantalum*, edited by F. T. Sisco and E. Epermian, John Wiley & Sons (1963).

88. W. Ensinger, *Surface and Coatings Technology* 84 (1996) 434.

89. R. J. Morrisey, *J. Electrochem. Soc.* 117 (1970) 742.

90. I. M. Notter, D. R. Gabe, *Corrosion Science* 34 (1993) 851.

91. N. G. Thompson, J. H. Payer, *Corrosion Testing Made Easy: DC Electrochemical Test Methods*, Vol. 6, NACE, Houston (1998).

92. Maeng, S., Axe, L., and Tyson, T. A., *Corrosion* 58 (2002) 370.

93. NIST (National Institute of Standards and Technology), Certificate of Analysis: Standard Reference Material 661 (AISI 4340 Steel), 2001.

94. Mauvais, C.J., Latanision, R. M., and Ruff, Jr., A. W., *J. Electrochem. Soc.* 117 (1970) 902.

95. ASTM G5-94, *Standard Reference Test Method for Making Potentiostatic and Potentiodynamic Anodic Polarization Measurements*, ASTM International, West Conshohocken, PA (1999).

96. B. K. Teo, *Extended X-ray Absorption Spectroscopy: Basic Principles and Data Analysis*, p. 114, Springer-Verlag, New York (1986).

97. G. Long, J. Kruger, Chapter 4: Surface X-Ray Absorption Spectroscopy, EXAFS and NEXAFS, for the in situ and ex situ Study of Electrodes, in *Techniques for Characterization of Electrodes and Electrochemical Processes*, Edited by R. Varma and J. R. Selman, John Wiley & Sons, Inc. (1991).

98. S. L. Lee, D. Windover, M. Audino, D. W. Matson, E. D. McClanahan, *Surface and Coating Technology* 149 (2002) 62.

99. L. A. Clevenger, A. Mutscheller, J. M. E. Harper, C. Cabral Jr. K. Barmak, *J. Appl. Phys.* 72 (1992) 4918.

100. N. Schwartz, E. D. Feit, *J. Electrochem. Soc. Solid State Sci. Technol.* 124 (1977) 125.

101. B. Elsener, A. Rota and H. Böhni, *Material Science Forum* 44/45 (1989) 29.

102. W. Tato and D. Landolt, *J. Electrochem. Soc.* 145 (1998) 4173.

103. H. A. Jehn, *Surface and Coatings Technology* 125 (2000) 212.

104. C. Liu, Q. Bi, A. Leyland, A. Matthews, *Corrosion Science* 45 (2003) 1257.

105. L. Gladczuk, A. Patel, C. Singh Puar, M. Sosnowski, *Thin Solid Films* 467 (2004) 150.

106. M. H. Read, D. H. Hensler, *Thin Solid Films* 10 (1972) 123.

107. S. Lee, W. Ho, F. D. Lai, *Materials Chemistry and Physics* 43 (1996) 266.

108. S. H. Ahn, J. H. Lee, J. G. Kim, J. G. Han, *Surface & Coatings Technology* 177/178 (2004) 638.

109. F. Mansfeld, *Corrosion* 27 (1971) 436.

110. D. K. Merl, P. Panjan, M. Cekada, M. Macek, *Electrochimica Acta* 49 (2004) 1527.

111. F. Mansfeld, *Electrochimica Acta* 38 (1993) 1891.

112. Q. Lu, S. Mato, P. Skeldon, G. E. Thompson, D. Masheder, *Thin Solid Films* 429 (2003) 238.

113. S. Maeng, L. Axe, T. Tyson, L. Gladczuk, M. Sosnowski, *J. Electrochem. Soc.* (2004) in press.

114. R. Brown, M. N. Alias, R. Fontana, *Surf. Coat. Technol.* 62 (1993) 467.

115. J. L. He, C. H. Chu, H. L. Wang and M. H. Hon, *Surf. Coat. Technol.* 63 (1994) 15.

116. J. Munermasa, T. Kumakiri, *Surf. Coat. Technol.* 49 (1991) 496.

117. D. W. Matson, E. D. McClanahan, S. L. Lee, D. Windover, *Surf. Coat. Technol.* 146-147 (2001) 344.

118. P. J. Cote, G. Kendall, M. E. Todaro, *Surf. Coat. Technol.* 146-147 (2001) 65.

119. A. Arakcheeva, G. Chapuis, V. Grinevitch, *Acta Cryst.* B58 (2002) 1-7.

120. L. Fedrizzi, S. Rossi, F. Bellei, F. Deflorian, *Wear* 253 (2002) 1173.

121. X. Cheng, H. Ma, S. Chen, L. Niu, S. Lei, R. Yu, Z. Yao, *Corro. Sci.* 41 (1999) 773.

122. M. Bojinov, G. Fabricius, T. Laitinen, T. Saario, G. Sundholm, *Electrochim Acta* 44 (1998) 247.

123. B. E. Wilde, F. G. Hodge, *Electrochim. Acta* 14 (1969) 619.

124. S. Tanaka, N. Hara, K. Sugimoto, *Mater. Sci. Eng.* A198 (1995) 63.

125. P. Kofstad, *High Temperature Corrosion*, p. 309, Elsevier Applied Science Publishing CO., Inc., New York (1988).

126. R. H. Burns, J. C. Fang, P. Kumar, in *Tantalum*, E. Chen, A. Crowson, E. Lavernia, W. Ebihara, P. Kumar, Editors, p. 273, TMS Publications, Warrendale, PA (1996).

127. N. C. Stephenson and R. S. Roth, *Acta. Cryst.* B27 (1971) 1037.

128. N. C. Stephenson and R. S. Roth, *J. of Solid State Chemistry* 3 (1971) 145.

129. L. A. Aleshina, S. V. Loginova, *Crystallography Reports* 47 (2002) 415.

130. P.C. Joshi, M. W. Cole, *J. Appl. Phys.* 86 (1999) 871.

131. A. Fukumoto, K. Miwa, *Phys. Rev.* B 55 (1997) 11155.

132. V. B. Voltovich, V. A. Lavrenko, V. M. Adejev, and E. I. T. Golovko, *Oxidation of Metals* 43 (1995) 509.

133. P. Kofstad, *J. Inst. Metals* 90 (1962) 253.

134. S. Steeb and J. Renner, *J. Less-Common Metals* 9 (1965) 181.

135. G. S. Oehrlein, F. M. d'Heurle, A. Reisman, *J. Appl. Phys.* 55 (1984) 3715.

136. S. L. M. Schroeder, G. D. Moggridge, R. M. Ormerod, T. Rayment, *Surface Science* 324 (1995) L371.

137. T. Ressler, WinXAS 2.1, 2001 (Fritz-Haber-Institut der MPG, Department of Inorganic Chemistry, Faradayweg 4-6D-14195 Berlin, Germany).

138. J. J. Rehr, J. Mustre de Leon, S. I. Zabinsky, R. C. Albers, *J. Am. Chem. Soc.* 113 (1991) 5135.

139. J. J. Rehr, S. I. Zabinsky, R. C. Albers, *Phys. Rev. Lett.* 69 (1992) 3397.

140. R. S. Roth, J. L. Waring, H. S. Parker, *J. of Solid State Chemistry* 2 (1970) 445.

141. S. Sato, T. Inoue, H. Sasaki, *Thin Solid Films* 86 (1981) 21.

142. K. Volz, A. Hasse, W. Ensinger, *Surface and Coating Technology* 136 (2001) 80.

143. J. Stringer, *J. Less-Common Metals* 11 (1966) 111.